

Novel Aspects in Terahertz: Channel Measurements, Modeling and Material Characterization

**Von der Fakultät für Ingenieurwissenschaften,
Abteilung Elektrotechnik und Informationstechnik
der Universität Duisburg-Essen**

zur Erlangung des akademischen Grades

Doktor der Ingenieurwissenschaften (Dr.-Ing.)

genehmigte Dissertation

von

M.Sc. Fawad Sheikh

aus

Sheikhupura, Pakistan

Gutachter:

Prof. Dr.-Ing. Thomas Kaiser

Prof. Dipl.-Ing. Dr. techn. Andreas F. Molisch

Tag der mündlichen Prüfung: 05.12.2019

DuEPublico

Duisburg-Essen Publications online

UNIVERSITÄT
DUISBURG
ESSEN

Offen im Denken

ub | universitäts
bibliothek

Diese Dissertation wird über DuEPublico, dem Dokumenten- und Publikationsserver der Universität Duisburg-Essen, zur Verfügung gestellt und liegt auch als Print-Version vor.

DOI: 10.17185/duepublico/73130

URN: urn:nbn:de:hbz:464-20201109-152906-1

Alle Rechte vorbehalten.

Acknowledgments

Prophet Mohammad, peace and blessings be upon him, said, “*He who does not thank people, does not thank Allah*” (Abu Dawud, Ahmad, Al-Tirmidhi).

First and foremost, I express my utmost gratitude to my hardworking advisor Prof. Thomas Kaiser, heading the Institute of Digital Signal Processing (DSV) at the University of Duisburg-Essen (UDE). Following the hidden message in the proverb “What cannot be completely attained, should not be completely left”, I managed to acquire knowledgeable experience. I once again extend my sincere thanks to Prof. Thomas Kaiser for recognizing my skills and granting me the opportunity to fulfill my dream Ph.D. studies at his institute. I feel quite lucky to avail this one time Ph.D. chance in life and that too with a kind and helpful mentor.

I am also thankful to Prof. Andreas F. Molisch from the University of Southern California (USC) in Los Angeles, USA for hosting me as an exchange student during my short term scientific mission at his WiDeS group in 2017 and serving as a co-supervisor.

I thank Prof. Klaus Solbach, Prof. Andreas Czylik and Prof. Andreas Stöhr for their intensive collaboration within the *Tera50 Project*. The most memorable moment; the world-record high spectral efficient wireless data transmission using a fiber-wireless system approach at 60 GHz and 325 GHz has been demonstrated using *Tera50* system.

A special thanks for Dr. Qammer H. Abbasi, lecturer at University of Glasgow, for hosting me during my second short term scientific mission. Working in James Watt Nanofabrication Centre was a wonderful experience.

My sincere thanks also goes out to Michael Wiemeler, my group leader at DSV.

Thanks also to Marc Hoffmann as an ever ready help throughout my stay at DSV.

I like to thank all former (Mohamed El-Hadidy, Yuan Gao, Trung Thanh Nguyen, Sundar Daniel Peethala, Dien Lessy, Abdulkader Ghwaji) and current members (Mohammed El-Absi, Jahangir Alam, Ali Abbas, Mai Alissa, Nidal Zarifeh, Yamen Zanteh, Feng Zheng, Theo Kreul) at the DSV who contribute to the good friendly atmosphere here. In particular, I acknowledge our secretaries Sabine Jankowski as well as Petra Stawicki for their strong organizational help and prompt responses. Further on, Heinz Schreiber for his help in establishing the measurement set-ups. It's nearly impossible to name all of you here, but you all deserve a proud appreciation for building up a unique atmosphere in the institute.

I am also super thankful to the German Research Foundation (Deutsche Forschungsgemeinschaft, DFG) for funding my research to pursue my Ph.D. degree.

Last but not least, special thanks to my wife for her patience. She does not like the cold weather here but coped with the weather for me.

Duisburg, August 2019

F. Sheikh

Abstract

The new “Tera-Era” visions extreme high speed wireless data transfer of 100 Gb/s and beyond, machines computing at rates of teraflops, and electronic devices performing operations on the femtosecond time scale. The key to break this 100 Gb/s barrier by wireless means incites numerous applications in wireless communications, material characterization, spectroscopy, imaging, sensing, and screening. In fact, to achieve 100 Gb/s wireless links anywhere and anytime, a bandwidth of several gigahertz (GHz) is enforced, best sheltered in the targeted terahertz (THz) frequency range ($f \sim 0.25 - 4$ THz; $\lambda \sim 1.2 - 0.075$ mm) chosen for the research projects. For instance, to transmit at 300 GHz, this carrier frequency is the choice of fortune for four reasons: (i) it is five times higher than the highest frequency of 60 GHz used in wireless communications today; (ii) the atmospheric attenuation is of less extreme amounts to no more than 2.8 dB/km while falling within the spectral windows; (iii) it procures a 47 GHz of continuous bandwidth which is larger than the unified spectral resources globally available for all kinds of wireless systems; and (iv) this former barely accessible spectral window due to technological limitations allows a 100 Gb/s high throughput even with a simple modulation scheme for short-range wireless communications. The wireless data transmission of 100 Gb/s and beyond in the THz range is referred to as *THz Communications*. Helping this technological development is the rapid improvement in silicon germanium (SiGe), gallium nitride (GaN), and graphene technology, so that THz science and technology becomes a highly investigated research topic.

Yet despite the various advantages offered, the venture of employing the targeted frequency range in real world applications still sounds quite elusive. In order to realize the design of an efficient and reliable THz indoor communication system in the presence of rough surfaces and also taking into account the substantial research gaps, this dissertation aims to fill in these gaps

by exploring and unfolding each of the four emphases described in the following:

Emphasis 1 ... to thoroughly study, analyze and model the THz wave characteristics

The THz frequencies pose unique challenges for channel modeling due to sparse and extreme frequency selective behaviour of the propagation mechanism. In particular, the most critical feature proven to provide important contributions in determining spatial and temporal dispersion in the targeted frequency range is the diffuse scattering mechanism from rough surfaces, a necessary design consideration constituting a high proportion of all the propagation rays and hence, must be accounted for propagation modeling to accurately predict channel characteristics.

Emphasis 2 ... to classify rough surfaces and propose the advances in THz scattering models

A major challenge is the fact that at THz frequencies, dimensions of indoor building materials (e.g., granular wallpaper, plaster walls) are comparable to or even larger than the wavelength at hand and therefore these indoor materials which are normally now neglected and assumed smooth become rough evidently and are to be taken into account. The four scattering models, namely, Rayleigh-Rice (R-R), Effective Roughness (ER), classical Beckmann-Kirchhoff (cB-K), and modified Beckmann-Kirchhoff (mB-K) are chosen to provide solutions for the scattering problems and besides, they are widely accepted and developed in recent times. Likewise, we also endeavor to demonstrate a comparison between these approximate models along with their specific advantages and limitations.

Emphasis 3 ... to develop novel THz ray-tracing algorithms with distinct THz wave characteristics to support the proposed THz scattering models

Conventional GHz ray-tracer has some limitations because the distinct THz propagation mechanisms do not obey geometrical optics rules. Besides, the existing models and tools in the lower frequency bands (i.e., 2.4 GHz, 5 GHz, Ultra-Wideband, 60 GHz) do not consider the roughness of a material so profoundly smooth materials for GHz frequencies become rough now at THz frequencies. In consequence, it demands ray-tracing algorithms or simulation tools that can be employed for channel modeling at THz frequencies. In order to combat this challenge, we developed our own THz ray-tracing algorithms integrating the aforementioned THz scattering models of rough surfaces which can work on completely standalone basis.

Emphasis 4 ... to characterize indoor materials at THz frequencies using state-of-the-art instrumentation and techniques

This dissertation reports the first ever transmission measurements for a wide choice of indoor material groups such as *wood, plastic, paper, brick, glass* and *leather* at frequencies from 750 GHz to 1.1 THz using up-conversion (frequency-domain) method employing *Swissto12* system. Both the reflection coefficients (S_{11} , S_{22}), and transmission coefficients (S_{12} , S_{21}) are measured using this new and non-invasive electromagnetic technique. We reviewed various techniques for converting S-parameters to complex dielectric properties i.e., frequency dependent refractive index, absorption coefficient, relative permittivity, and relative permeability. Until previously, only THz time-domain spectroscopy (THz-TDS) system based on down-conversion (time-domain) method has been employed. The details about the techniques employed to convert S-parameters to frequency dependent refractive index $n(f)$ and absorption coefficient $\alpha(f)$ are elaborated in Chapter 5.

Zusammenfassung

Die neue “Tera-Ära” steht für extreme Hochgeschwindigkeitsdatenübertragungen von 100 Gb/s und mehr, die drahtlos ermöglicht werden sollen, für Rechenleistungen von TeraFLOPS pro Prozessor und für elektronische Schaltungen mit Schaltgeschwindigkeiten im Bereich von Femtosekunden. Das Durchbrechen der 100 Gb/s Grenze im drahtlosen Bereich wird vielfältige Anwendungen in den Bereichen drahtlose Kommunikation, Materialcharakterisierung, Spektroskopie, Bildverarbeitung, Sensorik und Screening ermöglichen. Tatsächlich wird zwingenderweise eine Bandbreite von mehreren Gigahertz (GHz) benötigt, bestens abgeschirmt im angestrebten Terahertz (THz) Frequenzbereich ($f \sim 0.25 - 4$ THz; $\lambda \sim 1.2 - 0.075$ mm), um überall und zu jeder Zeit drahtlose Verbindungen mit 100 Gb/s zu erreichen. Beispielsweise ist aus den folgenden vier Gründen das Senden bei 300 GHz eine gängige Wahl: (i) es ist fünfmal höher als die höchste derzeit verwendete Frequenz bei 60 GHz; (ii) die Dämpfung durch die Atmosphäre ist mit 2,8 dB/km weniger stark als in benachbarten Frequenzbereichen; (iii) es stellt ein zusammenhängendes Spektrum von 47 GHz bereit, mehr Bandbreite als alle derzeit betriebenen Funkssysteme zusammen erfordern; (iv) dieser früher aufgrund von eingeschränkten technologischen Möglichkeiten nur schwer zugängliche Frequenzbereich erlaubt Datenraten von 100 Gb/s selbst mit einfachen Modulationsverfahren für die drahtlose Nahbereichskommunikation. Die drahtlose Datenübertragung mit Raten von 100 Gb/s und mehr im THz Bereich wird als *THz Kommunikation* bezeichnet. Große Fortschritte in der Silizium-Germanium (SiGe), Gallium Nitrit (GaN) und der Graphen-Technologie unterstützen diese Entwicklung, so dass die THz Wissenschaft und Technologie ein schnell wachsender Forschungsbereich geworden ist.

Trotz der vielen Vorteile erscheint das Vorhaben, die Anwendungen im angestrebten Frequenzbereich unter realen Bedingungen umzusetzen, doch noch sehr utopisch. Um ein effizientes und zuverlässiges THz Kommunikationssystem, das die in Innenräumen vorhande-

nen rauen Oberflächen mit berücksichtigt, zu designen, ist es das Ziel dieser Dissertation, Forschungslücken durch das *Entfalten* der folgenden vier *Schwerpunkte* zu schließen:

Schwerpunkt 1 ... **sorgfältige Studie, Analyse und Modellierung der THz Wellencharakteristik**

THz Frequenzen stellen einzigartige Herausforderungen an die Kanalmodellierung durch ihr “sparse” und extrem frequenzabhängiges Verhalten der Übertragungsmechanismen. Insbesondere der diffuse Streumechanismus an rauen Oberflächen, die kritischste Eigenschaft, die einen großen Einfluss auf die räumliche und zeitliche Strahlausbreitung im angestrebten Frequenzbereich hat, sowie die notwendigen Design Abwägungen mit ebenfalls einem großen Einfluss auf die Strahlausbreitung, müssen beim Ausbreitungsmodell berücksichtigt werden, um das Kanalverhalten akkurat vorhersagen zu können.

Schwerpunkt 2 ... **Klassifizierung von rauen Oberflächen und Vorschlag eines fortschrittlichen THz Streumodells**

Eine wesentliche Herausforderung bei THz Frequenzen stellen die Dimensionen der im Innenraum verwendeten Materialien (z.B. Tapeten, Wandputz) dar, die vergleichbar oder sogar größer als die genutzte Wellenlänge sind. Diese Materialien können deswegen nicht länger als glatt angesehen und vernachlässigt werden, sondern müssen vielmehr als rau mitberücksichtigt werden. Die vier Streumodelle, namentlich, Rayleigh-Rice- (R-R), Effective Roughness- (ER), klassisches Beckmann-Kirchhoff- (cB-K) und modifiziertes Beckmann-Kirchhoff-Modell (mB-K) sind zur Lösung des Streuproblems ausgewählt worden, sie sind in letzter Zeit weitläufig akzeptiert und weiterentwickelt worden. Ich vergleiche diese Näherungsmodelle und demonstriere spezifische Stärken und Einschränkungen.

Schwerpunkt 3 ... **Entwicklung neuer Strahlverfolgung Algorithmen für den THz Bereich mit eindeutigen THz Wellencharakteristiken, die die vorgeschlagenen THz Streumodelle unterstützen**

Herkömmliche GHz Strahlverfolger kommen an ihre Grenzen, weil eindeutige THz Ausbreitungsmechanismen nicht den Regeln der Strahlenoptik (Geometrical Optics) folgen. Außerdem werden bei den für den GHz Bereich (z.B. 2,4 GHz, 5 GHz, UWB, 60 GHz) existierenden Modellen und Simulationswerkzeugen die Rauigkeit der Materialien nicht mitberücksichtigt, denn die im GHz Bereich hochgradig glatten Materialien werden bei THz Frequenzen rau. Konsequenterweise werden Strahlverfolgung Algorithmen oder Simulations SW benötigt, die eine Kanalmodellierung im THz Bereich ermöglichen. Als Antwort auf diese Herausforderungen

wurde ein eigener THz Strahlverfolger Algorithmus entwickelt, der die zuvor genannten THz Modelle der rauen Oberflächen einbezieht und völlig selbstständig arbeitet.

Schwerpunkt 4 ... **Charakterisierung von Innenraummaterialien mit Hilfe von dem Stand der Technik entsprechenden Messgeräten und –techniken**

In dieser Dissertation wird über die allerersten jemals gemachten Übertragungsmessungen an einer breiten Auswahl an Innenraummaterialien, wie z.B. Holz, Plastik, Papier, Stein, Glas und Leder bei Frequenzen von 750 GHz bis 1,1 THz berichtet. Dabei kam die Aufwärtswandelmethode (up-conversion method) (im Frequenzbereich) des *Swisstol2* Systems zum Einsatz. Sowohl die Reflexionskoeffizienten (S_{11} , S_{22}) als auch die Transmissionskoeffizienten (S_{12} , S_{21}) werden beide durch die neue und nichtinvasive elektromagnetische Technik gemessen. Es werden mehrere Techniken zur Umrechnung der S-Parameter in komplexe dielektrische Materialeigenschaft, wie frequenzabhängiger Brechungsindex, Absorptionskoeffizient, relative dielektrische Leitfähigkeit und relative Durchlässigkeit untersucht. Bis vor kurzem stand nur die THz Zeitbereichs Spektroskopie (time-domain spectroscopy, THz-TDS) basierend auf der Abwärtswandlung im Zeitbereich zur Verfügung. Die Details zur Umrechnung der S-Parameter in den frequenzabhängigen Brechungsindex $n(f)$ und den frequenzabhängigen Absorptionskoeffizienten $\alpha(f)$ werden in Kapitel 5 ausgeführt.

Contents

1	Introduction	1
1.1	Terabit Wirelss Communications at THz Frequencies	2
1.2	The Research Projects	4
1.3	Novelty of this Dissertation	5
1.4	Organization of this Dissertation	7
2	Terahertz Wave Characteristics	11
2.1	Advances in THz Multi-Ray Model	11
2.2	Free Space Propagation	12
2.3	Propagation Loss Factor of Atmospheric Attenuation	13
2.4	Novel Findings from Candle Flame Analysis	16
2.5	Reflection by a Smooth Surface	20
2.5.1	Dependence of the Reflection Coefficient on Polarization	21
2.5.2	Dependence on the Grazing Angle	22
2.5.3	Dependence on Frequency	22
2.6	Reflection by a Rough Surface	24
2.6.1	Basic Geometry of Scattering	25
2.6.2	Statistical Description of Rough Surface	26
2.6.3	The Rayleigh Method	28
2.6.4	Depolarization	33
2.7	Diffraction	33

2.8	Channel Performance at THz Frequencies	35
2.9	Development of THz Standards	38
2.10	Concluding Remarks	38
3	Advances in THz Scattering Models	41
3.1	Physics of Diffuse Scattering in THz	41
3.1.1	Surface and Volume Scattering	43
3.1.2	Coherent and Incoherent Scattering	44
3.2	Rough Surfaces at THz Frequencies	45
3.2.1	Gaussian Rough Surfaces	46
3.2.2	Non-Gaussian Rough Surfaces	47
3.3	Scenarios Environments	47
3.4	Frequency Dependence of Material Properties	51
3.5	Novel Solution of the Scattering Problem in THz	53
3.5.1	Rayleigh-Rice (R-R) Model	53
3.5.2	Effective Roughness (ER) Model	57
3.5.3	Classical Beckmann-Kirchhoff (cB-K) Model	61
3.5.4	Modified Beckmann-Kirchhoff (mB-K) Model	67
3.6	Concluding Remarks	68
4	Novel THz Ray-Tracing Algorithms	69
4.1	Ray-Tracing Algorithm (RTA) GUI	71
4.2	SISO Propagation and Channel Modeling	72
4.2.1	Received and Scattered Power	72
4.2.2	Angle of Arrival / Angle of Departure (AoA/AoD)	75
4.2.3	Time of Arrival (ToA)	77
4.2.4	Channel Impuse Response (CIR)	77
4.2.5	Channel Transfer Function (CTF)	78
4.3	MIMO Propagation and Channel Modeling	80
4.3.1	Single User-MIMO Channel Capacity	81

4.3.2	Multi User-MIMO Channel Capacity	84
4.4	Concluding Remarks	85
5	Novel THz Material Characterization Techniques	87
5.1	State-of-the-art Spectroscopic Technique in THz	88
5.2	Measurement Techniques	90
5.2.1	Free Space Technique	90
5.2.2	Waveguide Measurement Technique	93
5.3	Measurement Characterization Kit <i>Swissto12</i>	94
5.4	Description of Material Samples	95
5.5	Propagation of EM Waves in Dielectric Materials	104
5.6	Novel Analysis Techniques	106
5.6.1	Nicolson-Ross-Weir (NRW) based Methods	106
5.6.2	Kramers-Kronig (K-K) Relations based Method	116
5.7	Concluding Remarks	121
6	Conclusions and Future Challenges	123
6.1	Conclusions	123
6.2	Future Challenges	124
	List of Publications	127
	Bibliography	131

List of acronyms

AoA	Angle of Arrival
AoD	Angle of Departure
AWGN	Additive White Gaussian Noise
BER	Bit Error Rate
B-K	Beckmann-Kirchhoff
BPSK	Binary Phase-Shift Keying
cB-K	Classical Beckmann-Kirchhoff
CDF	Cumulative Distribution Function
CIR	Channel Impulse Response
CMOS	Complementary Metal Oxide Semiconductor
CSI	Channel State Information
CTF	Channel Transfer Function
cw	Continuous Wave
CxIR	Complex Impulse Response
3D	Three-Dimensional
dB	Decibels
DSV	Digital Signal Processing
EM	Electromagnetic
ER	Effective Roughness
FDTF	Finite-Difference Time-Domain
FMCW	Frequency Modulated Continuous Wave
FSPL	Free Space Path Loss
5G	Fifth Generation

GaAs	Gallium Arsnide
GaN	Gallium Nitride
GHz	Gigahertz
GO	Geometrical Optics
GUI	Graphical User Interface
HBT	Heterojunction Bipolar Transistor
HDF	High Density Fiberboard
HPBW	Half Power Beamwidth
IC	Integrated Circuit
IEEE	Institute of Electrical and Electronics Engineers
IFFT	Inverse Fast Fourier Transform
InP-HEMT	Indium Phosphide High Electron Mobility Transistor
IoT	Internet of Things
IR	Infrared
ITU	International Telecommunications Union
KA	Kirchhoff Approximation
KED	Knife Edge Diffraction
K-K	Kramers-Kronig
LoS	Line-of-Sight
LTE	Long Term Evolution
mB-K	Modified Beckmann-Kirchhoff
MCK	Material Characterization Kit
MIMO	Multiple-Input Multiple-Output
mm-Wave	Millimeter Wave
MMKK	Multiply Subtractive Kramers-Kronig
MoM	Method of Moments
MPC	Multipath Component
MU-MIMO	Multi-User Multiple-Input Multiple-Output
NF	Noise Figure
NLoS	Non-Line-of-Sight
NRW	Nicolson-Ross-Weir
OFDM	Orthogonal Frequency-Division Multiplexing
OOK	On-Off Keying

PC	Poly Carbonate
PDF	Probability Density Function
PDP	Power Delay Profile
PHY	Physical Layer
PL	Path Loss
PVC	Poly Vinyl Chloride
QAM	Quadrature Amplitude Modulation
QTDS	Quasi Time-Domain Spectroscopy
R&D	Research and Development
RF	Radio Frequency
R-R	Rayleigh-Rice
RT	Ray-Tracer
RTA	Ray-Tracing Algorithm
RX	Receiver
RX-LoS	Line-of-Sight Receiver
RX-NLoS	Non-Line-of-Sight Receiver
RXPs	Receiver Points
RMSE	Root Mean Square Error
SC	Single Carrier
SiGe	Silicon Germanium
SISO	Single-Input Single-Output
SOLT	Short Open Load Through
SSKK	Singly Subtractive Kramers-Kronig
SNR	Signal-to-Noise-Ratio
SU-MIMO	Single-User Multiple-Input Multiple-Output
TDS	Time-Domain Spectroscopy
TE	Transverse Electric
THz	Terahertz
TM	Transverse Magnetic
ToA	Time of Arrival
TOSM	Through-Open-Short-Match
T/R	Transmission/Reflection
T-WLAN	Terabit Wireless Local Area Network

T-WPAN	Terabit Wireless Personal Area Network
TX	Transmitter
UTD	Uniform Theory of Diffraction
UWB	Ultra Wideband
VLC	Visible Light Communication
VNA	Vector Network Analyzer
WiFi	Wireless Fidelity
WLAN	Wireless Local Area Network
WPAN	Wireless Personal Area Network
XPD	Cross-Polar Discrimination Ratio

Notation

ROMAN SYMBOLS

x	Scalar
\mathbf{x}	Vector
\mathbf{X}	Matrix
\mathbf{X}^*	Complex Conjugate of \mathbf{X}
A	Surface Area
B	Noise Bandwidth
c	Speed of Light
C	Shannon Data Capacity
$C(\tau)$	Autocorrelation Function of the Surface
d	Transmission Distance; Material Thickness
$d_{\text{TX/RX}}$	Distance from Trasnmitter-/ Receiver to Edge or Wedge
dS	Surface Element
$d\mathcal{S}$	Rough Surface Element
D	Diffraction Coefficient
E_{Diff}	Diffracted Electric Field
E_i	Path-Specific Incident Field
E_{LoS}	Line-of-Sight Electric field
E_{Ref}	Reflected Electric field
\mathbf{E}_r	Path-Specific Specularly Reflected Field
$\overline{E}_r, \overline{E}_s$	Norms of the Reflected and Scattered Fields on the Surface Element dS
E_{Scatt}	Scattered Electric Field
\mathbf{E}_s	Path-Specific Scattered Field
E_{s0}	Maximum Amplitude

$E_{\text{TX/RX}}$	Transmitted / Received Electric Field
$E_{\theta/\phi, k}$	Theta-/ Phi Component of the Electric Field of the k^{th} Path at the RX
FSPL	Free Space Path Loss
f	Frequency
f_{max}	Maximum Oscillation Frequency
f_i	Reference Frequency
F	Geometrical Factor
g	Roughness Coefficient
$G_{\text{TX/RX}}$	Transmit / Receive Antenna Gain
G_{θ}	Theta Component of the Receiving Antenna Gain
$h(\mathbf{r})$	First Moment of Random Variable of Surface Height at Position r
\bar{h}	Mean of Surface Height
h	Channel Impulse Response
H	Channel Matrix
k	Wave number
K	Renormalization Constant
ℓ_{cr}	Surface Correlation Length
L_{LoS}	Line-of-Sight Propagation Loss Factor
L_{Ref}	Length of the Reflected Path
L_{Scatt}	Length of the Scattered Path
m	Iteration Number
M	System Margin; Constant for Tile Size
n	Complex Refractive Index
n	Normal Vector of Scattering Surface
N	Number of Transmit-/ Receive Antennas; Number of Tiles
NF	Receiver Noise Figure
\mathbf{N}_p	Number of Paths
N_o	Noise Spectral Density
O	Far-field Receiving Point O
$p_h(h)$	Probability Distribution Function of the Surface Height
P_k	Time Averaged Power of the k^{th} Path
P	Far-field Receiving Point P; Cauchy Principal Value
P_i	Direct Path

PL	Path Loss
P_e	Bit Error Rate
P_i	Incident Power
$P_{V/H}$	Received Power of the Vertical-/Horizontal Component
P_p	Power which Penetrates the Wall
$P_{TX/RX}$	Transmitted-/ Received Power
$P_{tot}(RX)$	Total Received Power
P_T	Total Transmitted Power
Q	Geometry Factor
\mathbf{R}	Polarization-Dependent Channel Matrix
R	Reflection Loss Factor
$\mathbf{R}_{TX/RX}$	Geometrical Depolarization Vector from Transmitter-/ Receiver
S	Scattering Coefficient; Reflection Surface
S_{ij}	Scattering Parameters
S^2	Diffuse Scattered Power
SNR	Signal-to-Noise Ratio
T	Transmission Coefficient
$u(t)$	Input Signal
$u(w)$	Response Function
v_g	Velocity in the Material
$v_{x/y/z}$	Component of the Scattered Wave Vector
x, y, z	Cartesian Coordinates
X_m	Excess Loss
XPD	Cross Polarization Discrimination Ratio
Z	Wave Impedance of Reflecting Material
Z_0	Free Space Impedence
$\mathbb{1}_{LoS}$	Indicator Function

GREEK SYMBOLS

α	Absorption Coefficient
α_a	Atmospheric Attenuation

$\alpha_a(f_i)$	Atmospheric Attenuation Coefficient at Reference Frequency f_i
α_r	Parameter that Sets Width of the Scattering Lobe
$\Delta x, \Delta y$	Distance Adjacent Receiver Positions in x and y Direction
η	Real Part of Refractive Index; Spectral Efficiency
η_{kk}	Real Part of Refractive Index based on Kramer-Kronig
γ	Propagation Constant
Γ	Reflection Coefficient
Γ_{in}	Total Reflection Coefficient
κ	Imaginary Part of Refractive Index
λ	Wavelength
λ_n	Nth Singular Value of Channel Matrix
μ_0	Free Space Permeability
μ_r	Relative Complex Permeability
ω	Angular Frequency
ω_c	Angular Cutoff Frequency
ψ	Continuous Scalar Function
ψ_θ	Relative Phase of the θ Component of the Far-field Electric Field
ψ_R	Angle between the Direction of the Reflected Wave and the Scattering Direction (Θ_2 and Θ_3)
ρ	Scattering Coefficient
ρ_0	Specular Component
ρ_{spec}	Rayleigh Roughness Factor
σ	Conductivity
σ^2	Noise Variance
σ_h	Standard Deviation of Surface Height
τ	Distance Between Two Randomly Selected Surface Points
τ_{meas}	Measured Group Delay
τ_{calc}	Calculated Group Delay
θ_A and ϕ_A	Direction from which the Path Arrives at the RX
θ_D and ϕ_D	Direction in which the Path Leaves from the TX
$\Theta_{i/r/s}$	Angles in Illustration of the Scattering Geometry
$\Theta_{1/2/3}$	Angles in Illustration of the Scattering Geometry
$\tilde{\epsilon}_r, \tilde{\tilde{\epsilon}}_r$	Real and Imaginary Part of Relative Complex Permittivity

$\tilde{\mu}_r, \tilde{\mu}_r$	Real and Imaginary Part of Relative Complex Permeability
ϵ_0	Free Space Permittivity
ϵ_r	Relative Complex Permittivity
$\Gamma_{\text{TE/TM}}$	Conventional Fresnel Coefficient in TE-/TM Polarization
$\varphi_{\text{TX/RX}}$	Orientation of the Incident-/ Emergent Plane with Respect to the Surface
φ	Phase of the Transmission Coefficient
$\tilde{\Gamma}_{\text{TE/TM}}$	Modified Fresnel Coefficient in TE-/TM Polarization
$\zeta_{1,2}$	Cross Polarization Coefficients

Introduction

By 2025 wireless data rates up to 1 Tb/s will be on demand [1, 2], helping to get through the struggle in progress of multimedia technology, high-speed internet, data and voice communications. For example, a forthcoming next generation video format, namely super hi-vision has a resolution of 7680 x 4320, that is sixteen times larger than the current 1080p format, depending on its frame rate and color depth requires more than 24 Gb/s data rate [3]. In addition, some of the most promising 5G applications such as 8K 360 degree videos, vehicle-to-everything (V2X) bidirectional communications, and augmented/mixed reality will require in the near future wireless data transmission capacity exceeding several hundred Gb/s. In fact, public WiFi hotspots serving users with such high-speeds and bandwidth-intensive wireless applications also tend to deal with the rapid explosion of wireless data traffic in the coming years. More devices than ever are making matters worse. In addition, the present industrial automation is relying on cables due to the limited range and mobility of the current WiFi data transmission capacity. In other words, the current wireless networks are not yet on the foreseeable horizon of “wireless everything” or “everything wireless”. In this work, *wireless* refers to the point-to-point radio systems that propagate inside rooms as will be reasoned later. However, by exploiting the power and peril of terahertz (THz) frequencies, i.e. in the targeted frequency range of 250 GHz to 4 THz, numerous applications for high-speed data links such as 5G cellular network, terabit wireless local area networks (T-WLANs), terabit wireless personal area networks (T-WPANs), cloud servers and ultrafast kiosk downloads are practically realizable. Therefore, development efforts are being carried out on the THz technology components (sources, detectors, mixers, circuits, antenna technology etc.) at various research and development (R&D) centers across the globe in order to overcome the scarcity in terms of spectrum, channel congestion and capacity

limitations in the current wireless systems. Helping this development is the rapid improvement in silicon germanium (SiGe), gallium nitride (GaN), and graphene technology [4, 5], so that THz science and technology becomes a highly investigated research topic. Moreover, despite the many announcements for the end of Moore's Law, the data transmission rates in wireless networks such as cellular, local, and personal area networks, kept on increasing now and then at Moore's Law pace; by about a factor of ten every five years, as illustrated in Fig. 1.1.

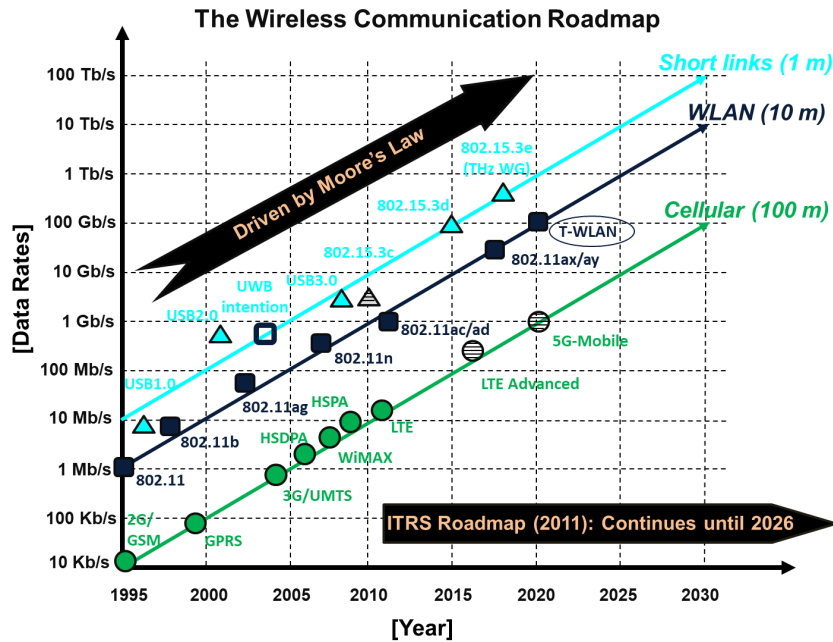


Figure 1.1: Wireless data rates' growth approximately keeping up with the pace of Moore's Law increasing by a factor of 10 every five years. Figure adapted from Fig. 1 in [2].

1.1 Terabit Wirelss Communications at THz Frequencies

The 100 Gb/s barrier crossover by wireless means incites numerous applications not only in wireless communications, but also in material characterization, spectroscopy, imaging, sensing, and screening. It seems clear that to achieve 100 Gb/s wireless links, one requires either larger swaths of spectrum, or very high spectral efficiencies. In the microwave regime, wireless data capacity has been exploited by increasing spectral efficiency with advanced modulation schemes and robust signal-processing techniques [6]–[9]. However, realization of such high data rates becomes quite challenging because of natural fundamental limitation of current technologies; limited bandwidth [3]. Likewise, the data rate provided by the *biologically friendly* technologies with frequencies above 10 THz, such as infrared (IR) and visible light communi-

cations (VLC), are restricted due to several technical and safety limitations [10].

A promising approach to this bottleneck is to transmit in higher frequency bands instead, where large swaths of spectrum are available. An incarnation of this approach is transmission at millimeter-wave (mm-wave) frequencies (20–100 GHz), which has gained much attention in the context of WiFi (802.11ad) [11] and 5G [12]. However, even the large bandwidths available there (up to several GHz) may not be sufficient for many aforementioned future applications, so a move to even higher frequencies becomes desirable, where extreme wide bandwidths (i.e., 20 GHz and beyond) are available as listed in Table 1.1. Fortunately, the two atmospheric spectral windows centered at 300 and 350 GHz band offer 47 GHz of continuous bandwidth [13, 14] with relatively low atmospheric attenuation. The wireless data transmission of 100 Gb/s and beyond in the THz range is referred to as *THz Communications*.

Table 1.1: Comparison: Conventional vs. THz channel.

About THz: What is it and why does the world need it?				
Band	2.4 GHz	60 GHz	300 GHz	1 THz
Bandwidth	40 MHz	~ 2 GHz	= 47 GHz	up to 110 GHz
Data rate	600 Mbps	~ 4 Gbps	~ 100 Gbps	> 100 Gbps
Path loss @ 5 m	= 54 dB	~ 82 dB	~ 96 dB	~ 106 dB
Antenna type	~ 3 dBi	up to 25 dBi	up to 35 dBi	up to 40 dBi

At THz regime, the propagation mechanism primarily differs from the lower frequency bands. For instance, the frequencies above 300 GHz are throbbled with significant atmospheric attenuation outside spectral windows [15], notably larger free space path loss [16], and high penetration as well as reflection losses [17]. In addition, indoor building materials such as granular wallpaper and plaster walls which are considered as smooth at lower frequencies (i.e., 2.4 GHz, 5 GHz, Ultra-Wideband, 60 GHz) have become rough now due to the significantly shorter wavelength at THz frequencies and thus scatter [18]. Further, the increasing trend of using formidable range of raw materials (e.g., cinder block, limestone slab, cork sheet etc.) for designing the interior of the indoor environments is on the rise. Consequently, the knowledge of scattering properties of indoor building materials is mandatory [19]. As such, higher frequencies with shorter wavelengths lead to smaller sized RF components including antennas. Nevertheless, when constructing sub-THz designs, compact sizes and wide bandwidths are preferred. In addition, high gains are also paramount for these designs in order to alleviate high

propagation losses to sustain communication links. For instance, the highest gain antennas such as horns owing to their well defined beam patterns with relatively low sidelobe structures are quite useful. These horns coupled with additional beam collimating lenses are the best option particularly in case of fixed radio links. Whereas electrically steered antennas will most likely be used for *in-room* T-WLANs. Moreover, less directive horns (with beam divergence) at both transmitter (TX) and receiver (RX) will be sufficient for close proximity communications. It should be emphasized that these unique features lead to developing new models to characterize the multipath THz propagation channel and consequently, extend the research of channel propagation modeling. In fact, the transmission at THz band is limited to indoor short-range communication and the outdoor applications greatly rely on line-of-sight (LoS) propagation of a few tens of meters.

1.2 The Research Projects

The presented work is a part and parcel of two projects, namely, *Tera50* and *MARIE M01*. A brief overview of the projects is summarized below:

Tera50 Project

The Tera50 is a part of the DFG-SPP (Deutsche Forschungsgemeinschaft - Special Priority Program) funded by the German Research Council (Deutsche Forschungsgemeinschaft, DFG) during the period 06/2012–08/2016 in the first phase. *Tera50+* in the second phase is scheduled to span from 09/2016–09/2019. It is coordinated by IHP GmbH and as of today comprises of 11 research projects from 16 German universities. The key objective of the DFG priority program SPP 1655 (Wireless 100 Gb/s and beyond) is to increase the data rates of mobile wireless systems from today (year 2012) of around 1 Gb/s to future 100 Gb/s and higher. Such an enormous boost in the data rate by a minimum of two orders of magnitude requires either an extremely high spectral efficiency or an extreme wide bandwidth of several tens of GHz or a trade-off between them. In order to reach this ambitious goal, a suitable carrier frequency and bandwidth are required under several constraints, including the worldwide regulation, the wireless propagation effects and various technology constraints like power consumption, semiconductor technology, processing performance, and circuit design.

MARIE M01 Project

Whereas the vision of MARIE (Mobile Material Characterization and Localization by Electromagnetic Sensing), a Collaborative Research Centre / Transregio 196, is to precisely and dynamically characterize and localize even moving materials in our daily surroundings. In order to achieve this vision, suitable devices and overall systems are needed to carry out the localization, characterization and visualization of materials. The final goal is the achievement of a mobile **MAteRIal TranscEiver** that can either be interpreted as a novel compact sensory organ that extends the human senses or, on a more industrial level, as a device that systematically creates material maps for searching and classifying objects in arbitrary environments. MARIE is also supported by the German Research Council. It is structured in three phases with a duration of 4 years each: in Static Lab (2017–2020), advances in technology are in the foreground while the sensing frequency in the static lab environment stretches to 1.5 THz. Mobile Sensor (2021–2024) addresses energy efficiency to enable mobility with an extended frequency range towards 4 THz. Dynamic Environment (2025–2028) takes into account all remaining challenges, by fusing with additional sensing principles, to ultimately achieve the vision of a Mobile **MAteRIal TranscEiver**. The spokesperson and coordinator of the CRC/TRR 196 is my advisor, Prof. Thomas Kaiser. As of today, 5 German universities and two Fraunhofer Research Centers with 23 research projects are thriving for the MARIE vision.

1.3 Novelty of this Dissertation

The motivation behind this dissertation is a need worthy of further exploration. The primary novelty aspects and significance of this work with respect to the existing work on THz communication and material characterization are summarized as follows:

Novelty 1

Development of a novel self-programmed broadband THz three dimensional (3D) ray-tracing algorithm (RTA) tool using MATLAB based graphical user interface (GUI) implementing the four famous and widely used scattering models: (i) Rayleigh-Rice (R-R); (ii) Effective Roughness (ER); (iii) classical Beckmann-Kirchhoff (cB-K); and modified Beckmann-Kirchhoff (mB-K) to examine the implications of diffuse scattering on a channel for several different roughnesses and dielectric constants of the random rough surfaces at THz frequencies. Unlike others,

ER introduces two scattering radiation pattern models: Lambertian and Directive Model. The main characteristics of these aforementioned models and the THz RTA are discussed in detail in Chapters 3 and 4, respectively. *This exceptional RTA is uniquely possessed by only three groups in the world.*

Novelty 2

We employ the B-K model to report the first results of channel capacities of indoor THz massive multiple-input multiple-output (MIMO) channels considering smooth and rough surfaces for both LoS and non-line-of-sight (NLoS) scenarios. We assume $N = 64$ antennas at both TX and RX. Besides, we consider both single-user MIMO (i.e., transmitting to each user independently) and multi-user MIMO (i.e., transmitting to each user simultaneously) for computing the channel capacity. As the rough surface gives rise to an influx of diffuse scattered paths in addition to the specular reflected path, the anticipating multiplexing gain is found to apparently enhance the channel capacity particularly for NLoS scenario (for a certain RX location and upon certain degree of surface roughness). More detail hereafter in Chapter 4.

Novelty 3

We employ a THz *Swissto12* system to report the first transmission measurements for a wide choice of indoor material groups such as *wood, plastic, paper, brick, glass* and *leather* at frequencies from 750 GHz to 1.1 THz using up-conversion (frequency-domain) method. By using this new and non-invasive electromagnetic technique, THz material characterization kit (MCK), *Swissto12* enables the measurement of both the reflection coefficients (S_{11} , S_{22}) and transmission coefficients (S_{12} , S_{21}). The frequency dependent complex dielectric properties of materials (i.e. relative permittivity) are extracted from the scattering measurements using Nicolson-Ross-Weir (NRW) method. Previously, only THz time-domain spectroscopy (THz-TDS) system based on down-conversion (time-domain) method has been employed to determine the materials' dielectric properties at THz frequencies.

Novelty 4

The author is obliged to be a part of the Tera50 project. During its course, the world-record spectral efficient 64-QAM-OFDM Terahertz (325 GHz) transmission using the Tera50 system

with a world-record high data rate up to 59.0625 Gb/s per 10 GHz RF channel bandwidth has been demonstrated. Also, the world-record spectral-efficient 1024-QAM-OFDM 60 GHz over the air transmission using the Tera50 system with a maximum data rate of 9.7656 Gb/s per 1 GHz RF channel bandwidth has been demonstrated. For more details on this joint work, see [20].

1.4 Organization of this Dissertation

The primary contribution of this dissertation is to comprehensively study the THz propagation channel, deal with the scattering problem of random rough surfaces using advanced modeling approaches and finally develop a THz RTA tool. Moreover, the characterization of indoor materials is also a major part of this in order to fulfil the vision of MARIE project, hence, contributing to the mobile THz systems' development. This dissertation is composed of 6 chapters and an overview of each chapter is summarized as follows:

- **Chapter 2: Terahertz Wave Characteristics**

In this chapter, the formulae for THz multi-ray model are derived along with background information about the distinct THz propagation and scattering mechanisms. However, no attempt has been made to evaluate the impact of diffraction phenomena which I perceive is present though pivotal at lower microwave regions only. This chapter opens with the fundamental concepts of quantifying the smooth and rough surfaces, whilst the prime focus will remain on the rough surfaces characterized with two statistical roughness parameters, namely, the standard deviation height and the surface correlation length. In order to avoid repetition, the correlation length is discussed in the next Chapter 3 as it is more relevant to the Gaussian rough surface topic elaborated there. Prior to this, an analysis of the candle flame impact on ultra-broadband THz communication links across a spectrum of interest from 300 to 310 GHz is experimentally performed to elaborate the propagation loss factor. The dependencies of the reflection coefficient on three parameters, polarization, grazing angle and frequency are also briefly analyzed. Some details of the approval of IEEE Std 802.15.3d-2017 Standards for the lower THz frequency range are also revealed.

The contributions of this chapter are the harbinger of one journal and three conference papers:

- **F. Sheikh**, M. Alissa, A. Zahid, Q. Abbasi, and T. Kaiser, “Atmospheric Attenuation Analysis in Indoor THz Communication Channels”, IEEE AP-S Symposium on Antennas and Propagation and USNC-URSI, pp. 1-2, Atlanta, USA, July 2019
- **F. Sheikh**, N. Zarifeh, and T. Kaiser, “Terahertz Band: Channel Modelling for Short-range Wireless Communications in the Spectral Windows”, IET Microwaves, Antennas & Propagation, vol. 10, no. 13, pp. 1435-1444, October 2016
- **F. Sheikh**, M. El-Absi, Y. Gao, and T. Kaiser, “Terahertz Band: Analysis of Sounding Bandwidth and Center Frequency on Power Delay Profile Model”, Antennas and Propagation Conference (LAPC), pp. 1-5, Loughborough, UK, November 2015
- **F. Sheikh**, M. El-Hadidy, and T. Kaiser, “Terahertz Band: Indoor Ray Tracing Channel Model Considering Atmospheric Attenuation”, IEEE AP-S Symposium on Antennas and Propagation and USNC-URSI, pp. 1782-1783, Vancouver, Canada, July 2015

• Chapter 3: Advances in THz Scattering Models

In this chapter, we discuss surface scattering models divided into those that consider the effect of surface roughness in the specular direction of reflection only (i.e., R-R) and those that additionally attempt to predict the implications of non-specular diffuse scattering (i.e., ER, cB-K, mB-K) on channel models. These different scattering models and their working methodologies followed by the models’ capabilities and limitations are elaborated. The four models presented herein are probably the most well-known, and perhaps the most widely accepted also. The basic physics of diffuse scattering, i.e., two classes of surface and volume scattering open this chapter. Then, the nature of Gaussian and non-Gaussian rough surfaces and their impact at THz frequencies are discussed. This dissertation considers a homogenous, single layer, isotropic, and Gaussian random rough surface. But prior to this the example environments in which we perform the simulations are described.

The contributions of this chapter are a prelude to three conference papers:

- **F. Sheikh** and T. Kaiser, “A Modified Beckmann-Kirchhoff Scattering Model for Slightly Rough Surfaces at Terahertz Frequencies”, IEEE AP-S Symposium on Antennas and Propagation and USNC-URSI, pp. 1-2, Atlanta, USA, July 2019
- **F. Sheikh**, Q. Abbasi, and T. Kaiser, “On Channels with Composite Rough Surfaces at Terahertz Frequencies”, in Proc. 13th European Conference on Antennas and Propagation (EuCAP), pp. 1-5, Krakow, Poland, April 2019
- **F. Sheikh** and T. Kaiser, “Rough Surface Analysis for Short-Range Ultra-Broadband THz Communications”, IEEE AP-S Symposium on Antennas and Propagation and USNC-URSI, pp. 1-2, Boston, USA, July 2018

- **Chapter 4: Novel THz Ray-Tracing Algorithms**

This chapter begins with a description of the GUI and the comprising elements of our THz RTA. In addition to the ray-based methods, the self-developed ultra-broadband THz RTA tool integrates the aforementioned THz scattering models of rough surfaces. All of the basic propagation predictions' quantities such as received and scattered power, path loss, and the geometrical data of each path are generated as an output file with a few exceptions. Importantly, the developed RTA also employs the critical feature of THz propagation mechanisms such as specular reflection losses, diffuse scattering, depolarization, atmospheric attenuation, and high reflection losses of indoor common building materials. At present, our RTA tool does not consider any near zone fields. The chapter concludes with discussion on the obtained results.

The contributions of this chapter are the harbinger of one journal paper (accepted) and two conference papers:

- **F. Sheikh**, Y. Gao, and T. Kaiser, "A Study of Diffuse Scattering in Massive MIMO Channels at Terahertz Frequencies", accepted by IEEE Transactions on Antennas and Propagation, August 2019
- **F. Sheikh**, D. Lessy, and T. Kaiser, "A Novel Ray-Tracing Algorithm for Non-specular Diffuse Scattered Rays at Terahertz Frequencies", IEEE 1st Int. Workshop on Mobile THz Systems (IWMTS 2018), pp. 1-6, Velen, Germany, July 2018
- **F. Sheikh**, D. Lessy, M. Alissa, and T. Kaiser, "A Comparison Study of Non-specular Diffuse Scattering Models at Terahertz Frequencies", IEEE 1st Int. Workshop on Mobile THz Systems (IWMTS 2018), pp. 1-6, Velen, Germany, July 2018

- **Chapter 5: Novel THz Material Characterization Techniques**

In this chapter, a non-invasive technique based on *Swissto12* System (VNA-based) is introduced for measuring both the reflection and transmission coefficients at frequencies from 750 GHz to 1.1 THz. We characterized six (6) material groups comprising of 20 common indoor building materials and the complex dielectric properties of those materials are extracted from the scattering measurements using NRW method. Furthermore, another novel analysis technique such as Kramers-Kronig (K-K) relations is reviewed to convert S-parameters to complex dielectric properties in contrast to the THz-TDS system based on down-conversion method previously employed for these measurements.

The contributions of this chapter are a prelude to two conference papers:

- **F. Sheikh**, I. Mabrouk, A. Alomainy, Q. Abbasi, and T. Kaiser, "Indoor Material Properties Extraction from Scattering Parameters at Frequencies from 750 GHz to 1.1 THz", IEEE MTT-S Interna-

tional Microwave Workshop Series on Advanced Materials and Processes (IMWS-AMP), pp. 1-3, Bochum, Germany, July 2019

- J. Barowski, J. Jebramcik, I. Alwaneh, **F. Sheikh**, T. Kaiser, and I. Rolfes, “A Compact Measurement Setup for In-Situ Material Characterization in the Lower THz Range”, IEEE 2nd Int. Workshop on Mobile THz Systems (IWMTS 2019), pp. 1-5, Bad Neuenahr, Germany, July 2019

- **Chapter 6: Conclusions and Future Challenges**

Finally, in this chapter we suggest remaining challenges and future directions, reiterate our contributions, and then conclude this dissertation.

The structure and main contributions of this dissertation along with the harmonious relationship among the chapters are schematically shown in Fig. 1.2.

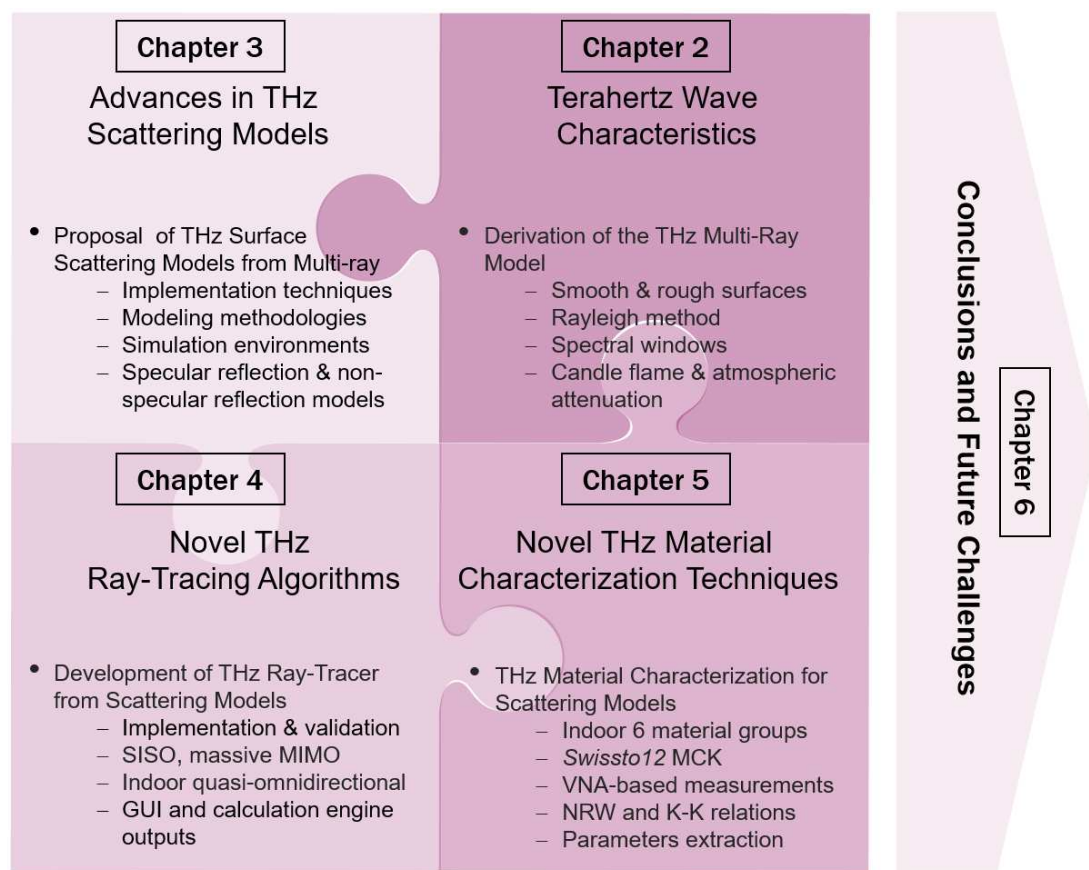


Figure 1.2: Schematic structure and main contributions of the dissertation.

Terahertz Wave Characteristics

The THz communication systems promise to transfer huge files in the blink of an eye by offering wireless data transfer of 100 Gb/s and beyond for indoor networks. Now, it is of interest in this chapter to understand the distinct THz propagation mechanisms, which form the basis for reliable high-speed and ultra-broadband mobile THz system design. This chapter encompasses research published in [13], [21]– [23].

2.1 Advances in THz Multi-Ray Model

We briefly describe the individual propagation mechanisms with the notion to provide an overall THz multi-ray model of the indoor THz wireless channel. Note that we mention only the essential propagation mechanisms neglecting transmission, since indoor material thicknesses in the order of few centimeters cause high transmission attenuations up to several 10 dBs for the material groups chosen in this study (*cf.* Sec. 5.2). At THz frequencies, all the surfaces of the common building materials reflect radio waves rather allowing transmission of the waves. Thereupon, transmission never contributes to the multipath propagation for indoor scenarios and can most often be disregarded at THz frequencies. While two major barriers, namely free space path loss (FSPL) and transmission attenuation (room entry or exit loss through walls), limit the signal transmission distance and coverage range to *in-room* scenarios. As mentioned earlier, the term *wireless* cites to the point-to-point radio systems propagating inside rooms. The THz multi-ray model for LoS propagation (direct path), reflected (specular), diffracted and diffuse scattered (non-specular) paths is expressed in Eq. (2.1).

$$\mathbf{E}_{\text{RX}} = \mathbf{E}_{\text{LoS}} + \mathbf{E}_{\text{Ref}} + \mathbf{E}_{\text{Diff}} + \mathbf{E}_{\text{Scatt}} \quad (2.1)$$

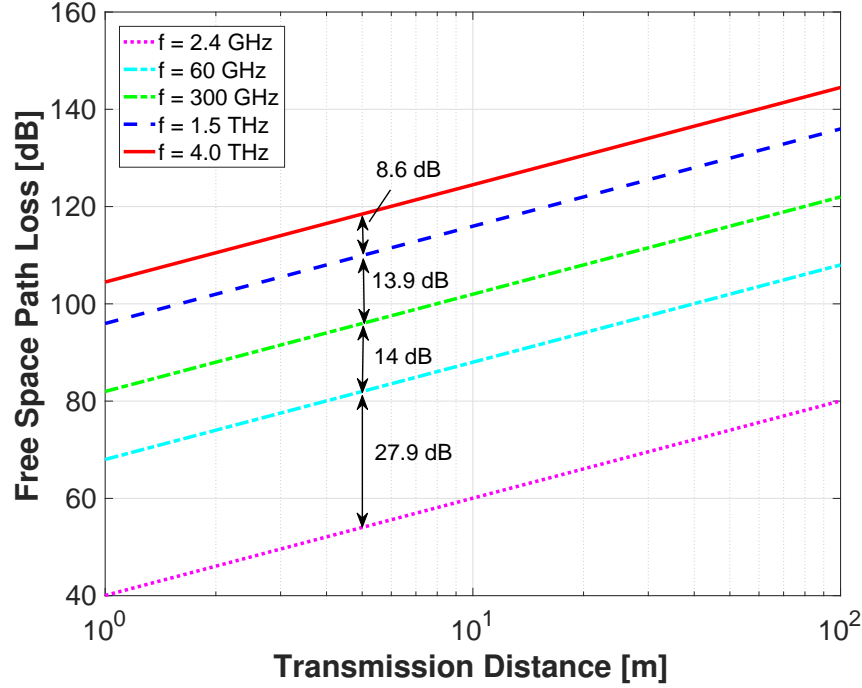


Figure 2.1: Free space path loss vs. transmission distance d .

2.2 Free Space Propagation

LoS propagation is the most simplest mode in which the propagation path between TX and RX does not consider any interaction with the absorbing or reflecting materials. It is also referred to as free space propagation. The LoS electric field \mathbf{E}_{LoS} received by an antenna RX accounting for the polarization vector as well as corresponding antenna gain \mathbf{G}^{RX} , and related to the emitted field \mathbf{E}_{TX} radiated by the TX antenna with polarization and antenna gain \mathbf{G}^{TX} is obtained from [24] as

$$\mathbf{E}_{\text{LoS}} = \left[\mathbf{G}_{\text{LoS}}^{\text{RX}} \right]^* \mathbf{G}_{\text{LoS}}^{\text{TX}} L_{\text{LoS}} \mathbf{E}_{\text{TX}} \quad (2.2)$$

Furthermore, the FSPL can be calculated based on the Friis equation as a function of transmission distance d and signal wavelength λ with the following definition in decibels (dB) [25]

$$\text{FSPL} = \left(\frac{4\pi d}{\lambda} \right)^2 \text{ [dB]} \quad (2.3)$$

The Eq. (2.3) is only valid when the distance is greater enough to fulfill the far-field condition. At THz regime, there is much more FSPL than at lower frequencies since it increases quadratically with the frequency assuming gain of the antennas is constant, as illustrated in Fig. 2.1. This FSPL is the fundamental cause that even without any additional attenuation in the transmission path of the THz wave, the received power is much lower than the transmitted power. It poses a major constraint on the communication distance and makes THz regime a promising candidate in delivering 100 Gb/s and beyond indoors rather than in outdoor applications.

2.3 Propagation Loss Factor of Atmospheric Attenuation

At THz frequencies, the LoS propagation is not only affected by FSPL, i.e. spreading of energy, the power is also lost along a transmission path due to the phenomena called atmospheric attenuation or molecular absorption. Therefore, the term L_{LoS} from Eq. (2.2) includes both of these losses. It is worth mentioning that the resonances for frequencies below 100 GHz occur at 24 GHz for water molecules and 60 GHz for oxygen, whilst the frequency range from 100 GHz to 1 THz is dominated by only water molecules as evident in Fig. 2.2. Conclusively, an

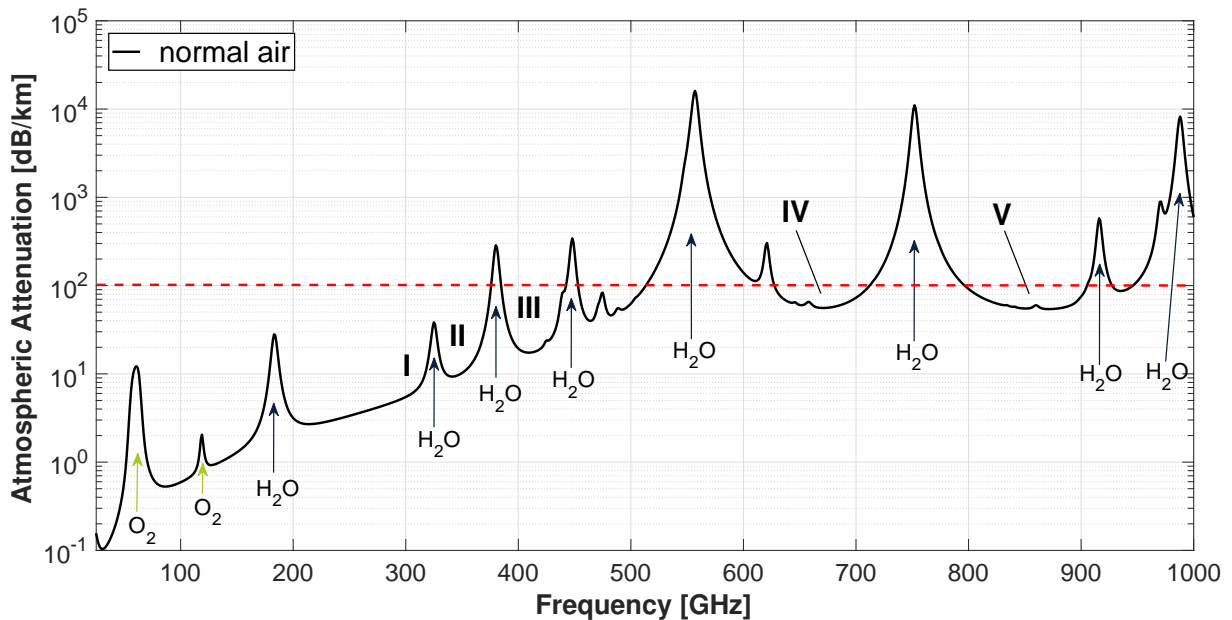


Figure 2.2: Atmospheric attenuation resulting from oxygen absorption and water vapor attenuation (water content 7.5 g/m^3 , pressure 1013 hPa , and atmospheric temperature 20°C).

approximation of total free space loss for the traveling wave in THz regime thereupon can be defined as the addition in dB of the FSPL and atmospheric attenuation loss

$$\text{Total Free Space Loss [dB]} = \text{FSPL [dB]} + \text{Atmospheric Attenuation Loss [dB]}$$

Table 2.1: List of five potential spectral windows at THz frequencies with corresponding minimum attenuations [26].

Window Number [#]	Center Frequency [GHz]	Bandwidth [GHz]	FSPL (at 5 m) [dB]	Atmospheric Attn. [dB/km]
I	300	47	~ 96	> 3
II	350	47	~ 97	> 3
III	410	51	~ 99	12
IV	670	87	~ 103	38
V	850	111	105	51

Despite the atmospheric attenuation, there are certain spectral windows available for *THz communication*. For instance, spectral windows centered at 300 and 350 GHz carrier frequencies offer 47 GHz of continuous bandwidth each with atmospheric impact amounts to no more than 2.8 dB/km, which allows a 100 Gb/s high throughput even with a simple modulation scheme for short-range wireless communications [3].

Atmospheric attenuation values can vary hugely depending on the transmission distance, frequency and the medium composition (i.e., how many molecules it interacts with). Between 250 GHz and 1 THz, five windows can be identified where the worst-case attenuation is below 100 dB/km based on the method described in the Recommendation P.676-10 from the International Telecommunications Union (ITU) [26]. Table 2.1 lists associated carrier frequencies of the five potential spectral windows available for wireless communications with the lowest possible attenuations along with the bandwidths.

Meanwhile, in Fig. 2.3, the channel transfer functions (CTFs) are depicted by ignoring and considering the atmospheric attenuation for LoS scenario. The geometry is given in Fig. 3.6 (second environment, *cf.* Sec. 3.3) where the TX and RX are at heights 2 m and 0.75 m respectively, and separated by a distance of 5 m. In order to show the impact of atmospheric attenuation only, the rough plaster walls and ceiling are modeled as ideally smooth surfaces ($\sigma_h = 0$). The details about smooth and rough surfaces are given in Sec. 2.5 and Sec. 2.6.

2.3. Propagation Loss Factor of Atmospheric Attenuation

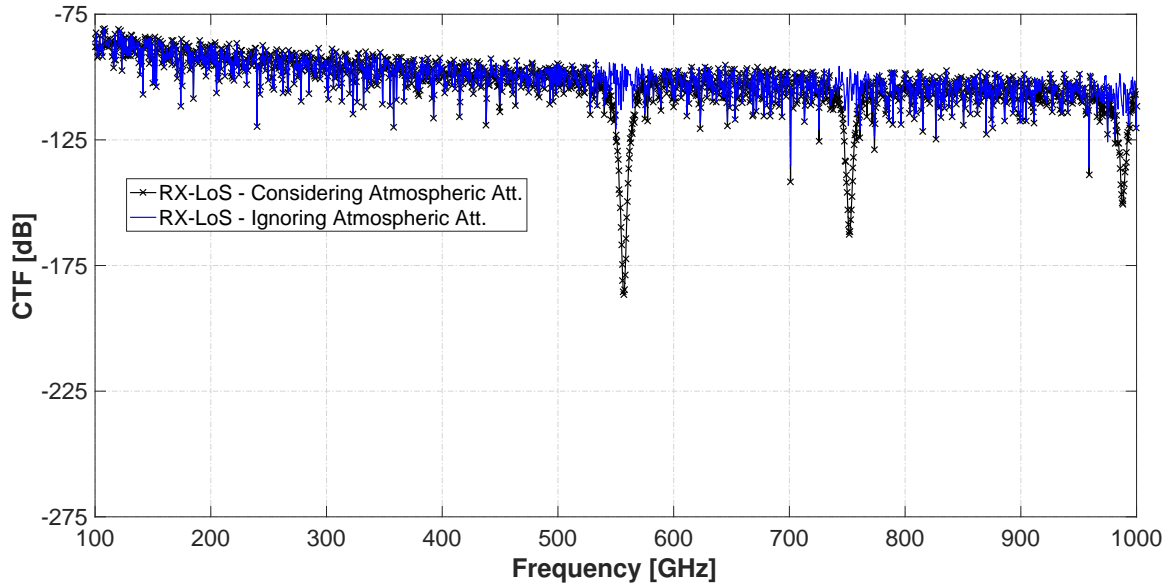


Figure 2.3: CTFs with and without considering the atmospheric attenuation for receiver location RX-LoS.

As deduced the peak-to-peak frequency dependent variation of up to 87.5 dB at $f_c = 557$ GHz (water vapor resonances) is well evident. Conversely, it is 0.1 dB at $f_c = 300$ GHz (spectral window). The atmospheric attenuation for short-range indoor wireless communications in LoS transmission links can thus be neglected.

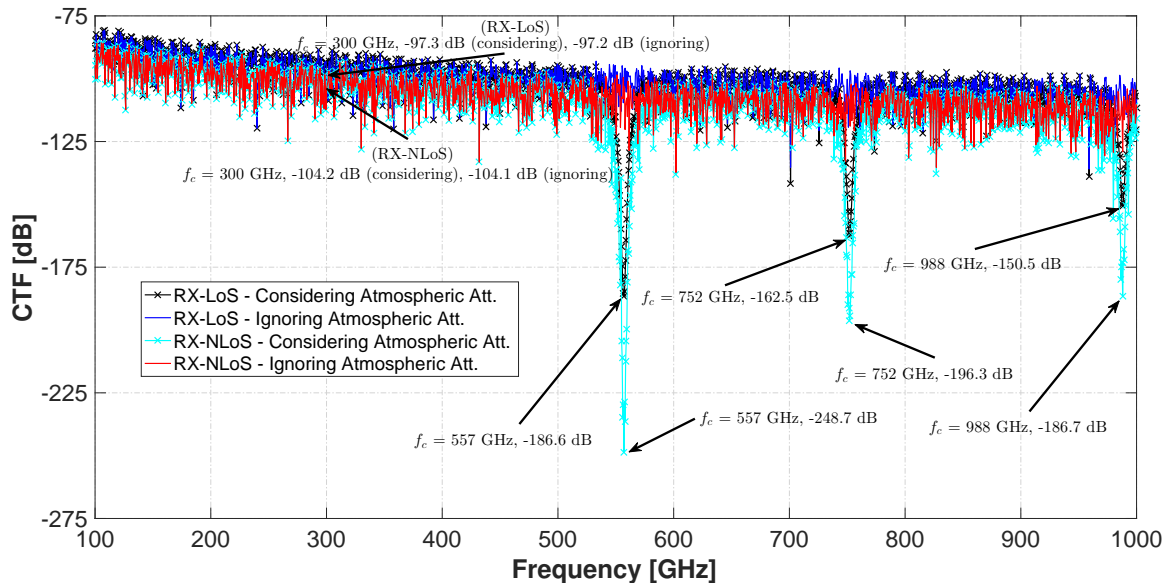


Figure 2.4: CTFs with and without considering the atmospheric attenuation for receivers RX-LoS and RX-NLoS.

As expected, in Fig. 2.4 the results depict that the multipaths are comparatively more attenuated for NLoS case. Moreover, in NLoS scenario most of the total received power contribution comes from reflections. For LoS scenario, however, the contribution of reflection is less poignant and the total received power depends highly on direct path. Unlike LoS, the peak-to-peak frequency dependent variation of up to 138.5 dB at $f_c = 557$ GHz, 87.8 dB at $f_c = 752$ GHz, and 57.6 dB at $f_c = 988$ GHz are ascertained. Nevertheless, at $f_c = 300$ GHz (spectral window) the atmospheric attenuation for both LoS and NLoS cases is identical.

2.4 Novel Findings from Candle Flame Analysis

To exploit the power and peril of THz frequencies in the presence of fire, a preliminary analysis of candle flame impact on the ultra-broadband THz communication links across the spectrum of interest from 300 to 310 GHz is investigated. The measurement setup is schematically illustrated in Fig. 2.5. This approach is based on recording the frequency dependent complex scattering parameter S_{21} extracted from channel measurements using a Rohde & Schwarz vector network analyzer (VNA) ZVA67 to study the variations in total received power and phase. All S_{21} , in addition to the system losses include the respective antenna gains (i.e., 25.5 dBi for horn antenna and 9.7 dBi for open-ended waveguide antenna).

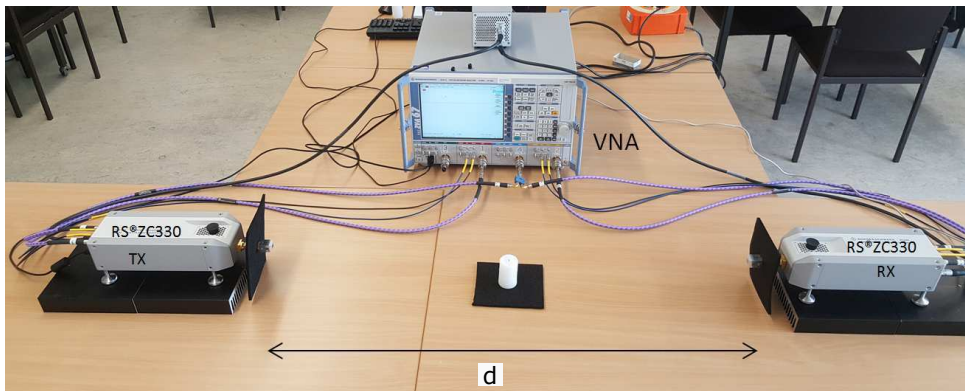


Figure 2.5: 300 GHz VNA-based channel sounder.

In Fig. 2.6, the open-ended waveguide and horn antenna are depicted. The channel measurements are performed in a lecture room under LoS environment. The chosen distances d between TX and RX are 0.5 m and 1 m, respectively. Perfect phase coherence is mandatory to get correct measurements for experimental analysis. Measurements are taken in different scenarios with respect to distance between the two RS@ZC330 extenders as well as the three

different antenna configurations namely, Horn-Horn, Horn-Open, and Open-Open. The number of chosen sweep points are 801 and the output power level from the extender is -8 dBm. A two-port TOSM (through, open, short, match) calibration is executed on the converter's waveguide ports considering our experiment's parameters. A detailed description of the scenario is omitted here because of its minor relevance in the results, found in the author's separate publications [27, 28].

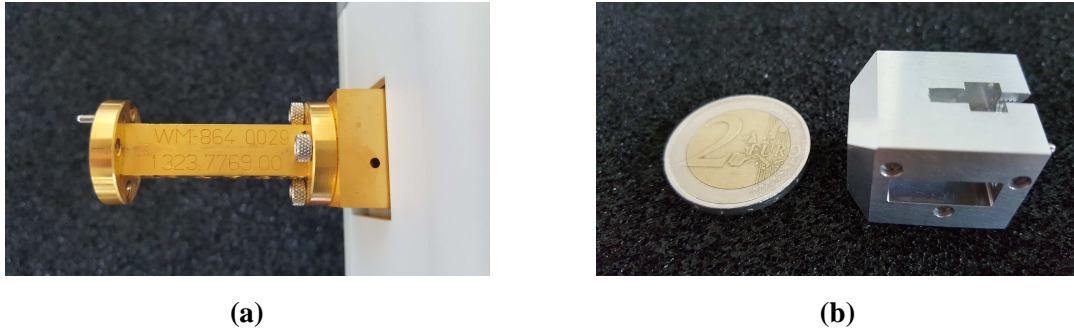


Figure 2.6: Measurement setup (a) Waveguide WM-864 (b) Horn antenna.

The transfer functions for the three scenarios are illustrated in Fig. 2.7 for $d = 0.5$ m and in Fig. 2.8 for $d = 1$ m. The respective phase shift is also illustrated for the above mentioned distances later in Figs. 2.9 and 2.10. In the measurement process the S_{21} is calculated by averaging 10 snap shots taken at different time instances as

$$PL[dB] = -10 \log_{10} \left[\frac{1}{N} \sum_{i=1}^{10} |S_{21}(f_i)|^2 \right] \quad (2.4)$$

The conclusions drawn from this work are:

- For both scenarios (i.e., $d = 0.5$ m and $d = 1$ m) in all the three channel configurations (i.e., Horn-Horn, Horn-Open, Open-Open), the experimental results demonstrate that the THz electromagnetic wave (EM) propagation is exposed to slight attenuation (i.e., amplitude) in the course of free space propagation through candle flame and this is mainly caused by water vapor attenuation. Hence, this slight attenuation does not pose any serious challenge to the precise characterization and localization of materials at THz frequencies.
- For both distances and all of the three channel configurations in the considered scenarios, we experimentally investigated the THz EM wave propagation concluding that the wave propagation is delayed (phase shifted). However, this phase shift is more prominent in (both) Open-Open antenna configurations.

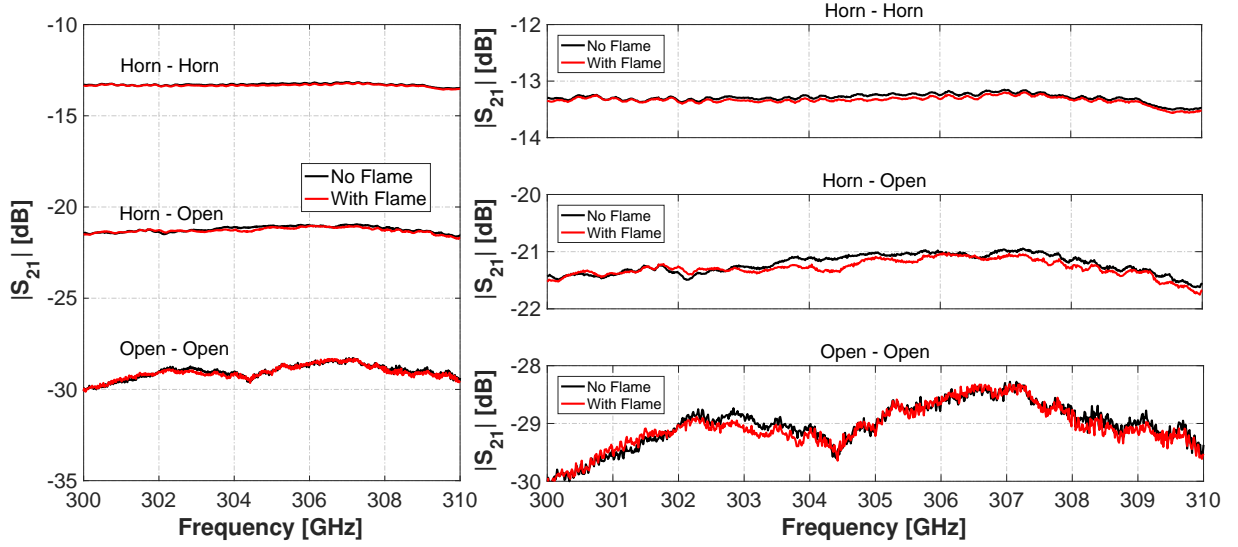


Figure 2.7: Transfer functions for three channel scenarios: Horn-Horn, Horn-Open, Open-Open for $d = 0.5$ m.

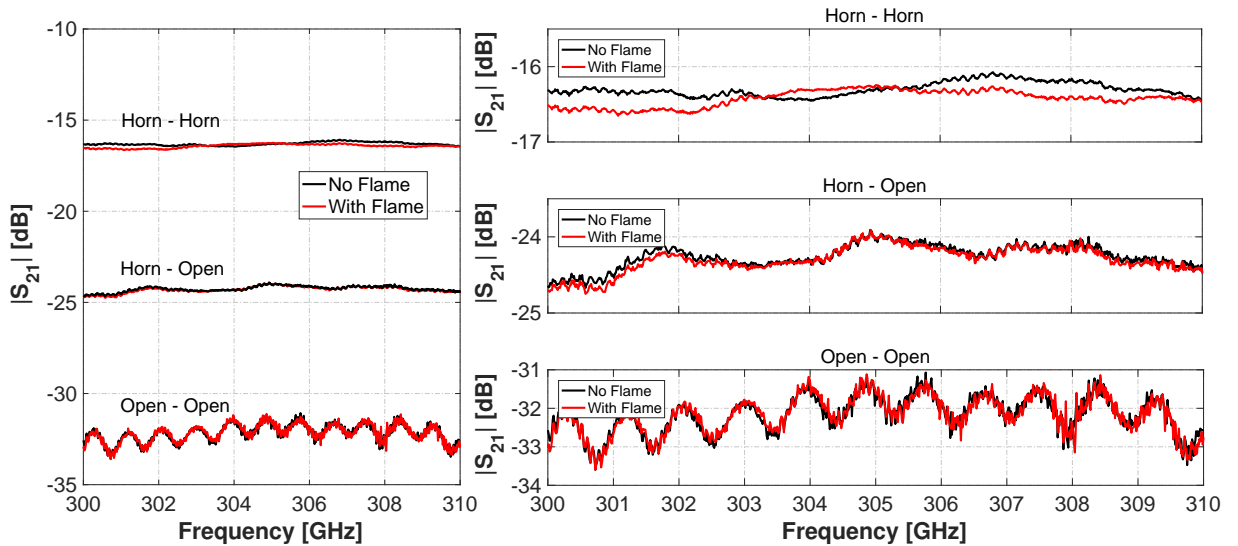


Figure 2.8: Transfer functions for three channel scenarios: Horn-Horn, Horn-Open, Open-Open for $d = 1$ m.

- The above results provide useful information for designing the ultra-broadband mobile THz system. Meanwhile, adaptive beamformers on TX as well as on the RX sides play a crucial role for precise localization of materials and adequately addressing the time-variant nature of the THz wireless channel.

The beam spot size for free space propagation (after the beam exit from the horn antenna) is bypassed. The beam spot size for 1 m distance is about 16.6 cm at $f = 300$ GHz in horizontal

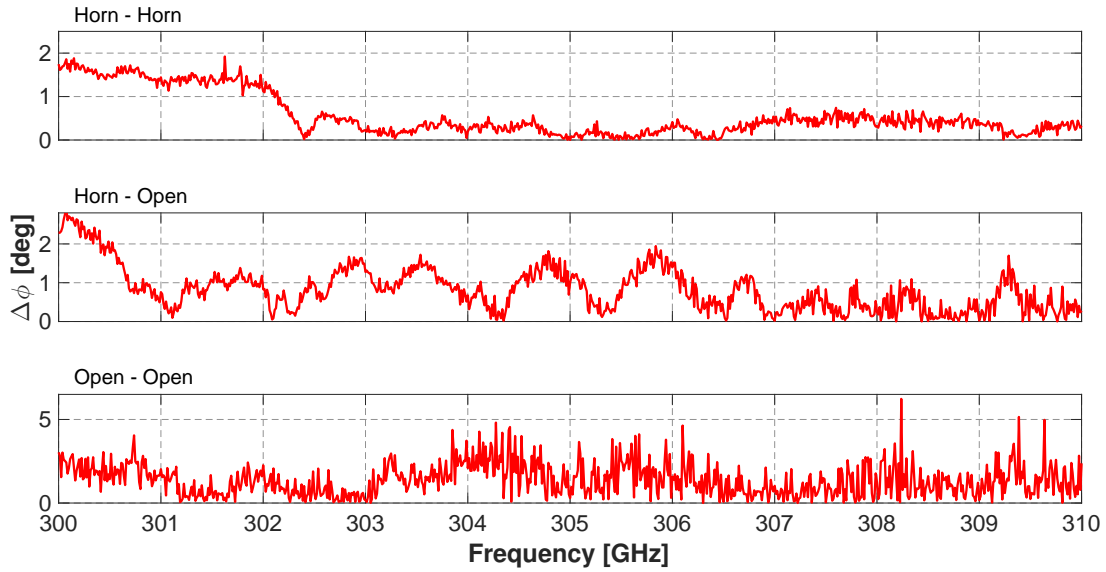


Figure 2.9: Phase difference with and without candle flame for three channel scenarios: Horn-Horn, Horn-Open, Open-Open for $d = 0.5$ m at 801 frequency points for $f = 300\dots310$ GHz in free space measurements.

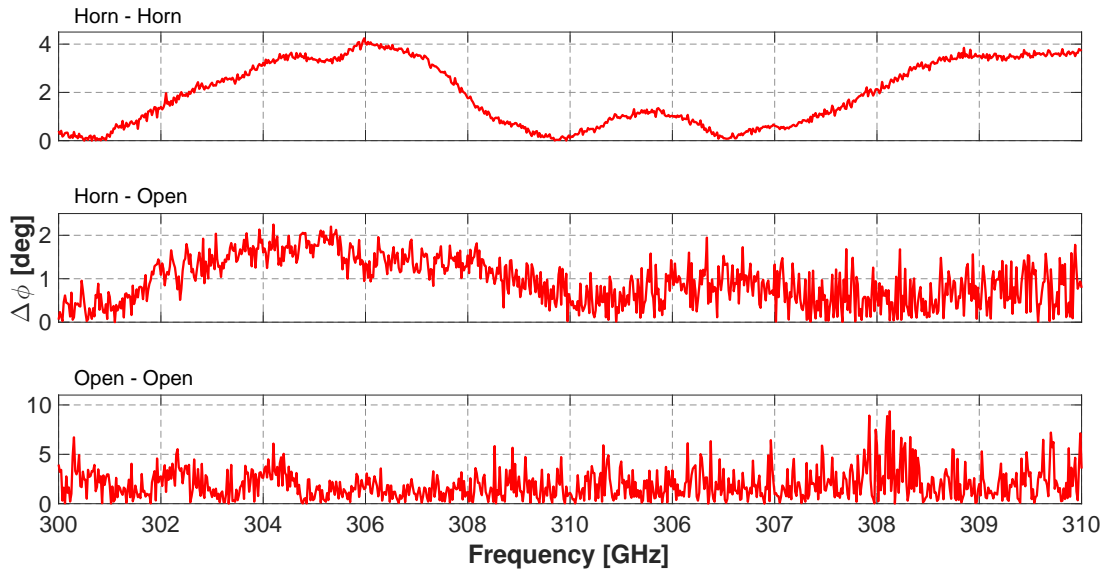


Figure 2.10: Phase difference with and without candle flame for three channel scenarios: Horn-Horn, Horn-Open, Open-Open for $d = 1$ m at 801 frequency points for $f = 300\dots310$ GHz in free space measurements.

and 12.5 cm in vertical, the measurements cannot be performed in the lab to study this, due to safety reasons. Interestingly, horn antennas have a divergent beam (i.e., in their spatial structure unless collimating lenses are used) where the beam spot size gets larger at farther distances.

2.5 Reflection by a Smooth Surface

A reliable communication link can be guaranteed only if a THz communication system utilizes indirect paths (i.e., reflections) as a backup. The direct paths could be completely blocked by moving objects into the LoS propagation, such schemes have to rely on NLoS propagation paths by making use of multiple reflections from the walls, floor and the ceiling. The indoor propagation environments usually have dielectric and conducting materials in their surroundings. The surfaces of these materials could be either smooth or rough. When an EM wave is incident on a smooth surface, a portion of the wave is reflected and part of the energy is lost due to the transmission into the material. This reflection can be perceived as specular in a single direction, where the angle of incidence and reflection angle are equal. If the reflection point belongs to the dimension of the surface, the first-order reflected field at the receiving point O can be expressed from [24] as

$$\mathbf{E}_{\text{Ref}}(O) = \left[\mathbf{G}_{\text{Ref}}^{\text{RX}} \right]^* \mathbf{R} \mathbf{G}_{\text{Ref}}^{\text{TX}} L_{\text{Ref}} \mathbf{E}_{\text{TX}} \quad (2.5)$$

where

$$\mathbf{R} = \mathbf{R}_{\text{RX}} \begin{pmatrix} \Gamma_{\text{TE}} & \zeta_1 \\ \zeta_2 & \Gamma_{\text{TM}} \end{pmatrix} \mathbf{R}_{\text{TX}} \quad (2.6)$$

Please note that the path length of reflections in L_{Ref} is the path length from TX to reflection point and then further from reflection point to point O . The ζ_1 and ζ_2 are cross polarization coupling coefficients. For specular reflection paths, these coefficients are equal to zero [11]. Note that \mathbf{R}_{RX} and \mathbf{R}_{TX} are the geometrical depolarization vectors from RX and TX, respectively [29], explained in more detail later in Section 2.6.

At THz frequencies, in case of ideally smooth and homogeneous surfaces such as glass and wood, the characteristics of the reflection can be described by the well-known Fresnel reflection coefficient Γ . The smooth surface Fresnel reflection coefficient depends not only on the electrical properties (permittivity, permeability, and conductivity) of the reflecting material, but also on the polarization, frequency, and grazing angle briefly explained below. Here, a definition of grazing angle will be beneficial to comprehend the reason of our considering grazing angle. The angle between the surface and the incident EM wave is the grazing angle in contrast to the incident angle which is between the surface normal and the incident EM wave. The grazing angle is sometime more useful particularly in case of small incident angles.

2.5.1 Dependence of the Reflection Coefficient on Polarization

The Fresnel reflection coefficient expressions for perpendicular (Γ_{TE}) and parallel (Γ_{TM}) polarizations for smooth surfaces can be found in [30, p. 21], as

$$\Gamma_{\text{TE}}(f, \Theta_i) = \frac{Z \cos \Theta_i - Z_0 \cos \Theta_t}{Z \cos \Theta_i + Z_0 \cos \Theta_t} \quad (2.7)$$

and

$$\Gamma_{\text{TM}}(f, \Theta_i) = \frac{Z \cos \Theta_t - Z_0 \cos \Theta_i}{Z \cos \Theta_t + Z_0 \cos \Theta_i} \quad (2.8)$$

Here, Θ_i is the incident angle, $\Theta_t = \arcsin(\sin(\Theta_i)Z/Z_0)$ is the angle of refraction, $Z_0 (=377 \Omega)$ the free space impedance and Z the wave impedance of the reflecting material, calculated as

$$Z = \sqrt{\frac{\mu_o}{\epsilon_o \left(n^2 - \left(\frac{\alpha c}{4\pi f} \right)^2 - j \frac{2n\alpha c}{4\pi f} \right)}} \quad (2.9)$$

where μ_o , ϵ_o , c , and f are free space permeability, permittivity, velocity, and the frequency of the incident wave, respectively. α the absorption coefficient and n the frequency dependent complex refractive index of the smooth surface, and are given by

$$n = \sqrt{\tilde{\epsilon}_r}, \quad \text{and} \quad \epsilon_r = \tilde{\epsilon}_r - j\tilde{\epsilon}_i = \tilde{\epsilon}_r - j60\lambda\sigma \quad (2.10)$$

where $\tilde{\epsilon}_r$, $\tilde{\epsilon}_i$, λ and σ are the real part of the relative complex permittivity, imaginary part of the relative complex permittivity, the wavelength at hand and the medium conductivity in mhos/meter, respectively. The empirically computed complex dielectric constants (ϵ_r) of the indoor materials at 300 GHz carrier frequency used in our modeling approaches are tabulated in Table 3.1.

In case of smooth surface, Γ_{TM} corresponds to vertical linear polarization, whilst Γ_{TE} corresponds to horizontal polarization. Comparing these two reflection coefficients, one can see that the response of horizontal polarization increases with increasing the incident angle, as indicated in Fig. 2.11.

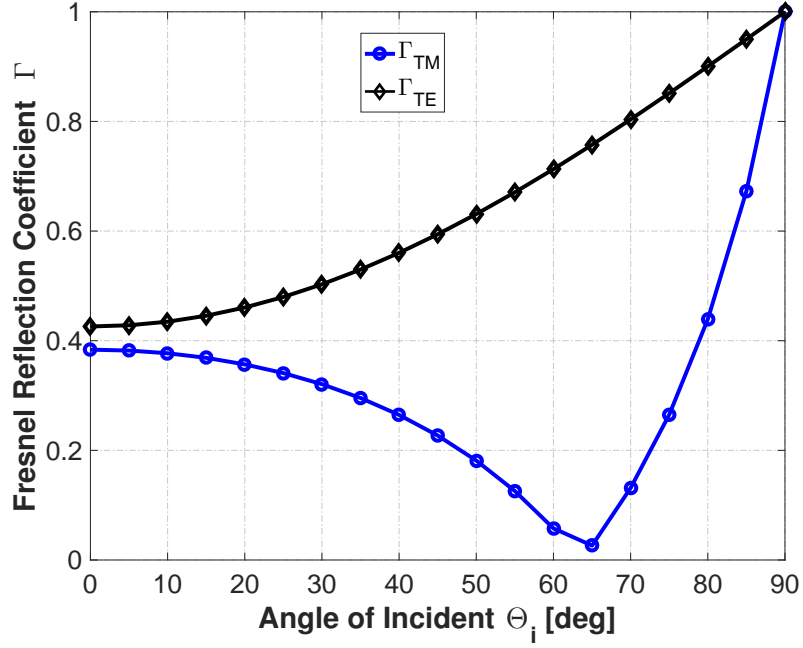


Figure 2.11: Magnitude of reflection coefficients Γ_{TE} and Γ_{TM} from smooth plaster ($\tilde{\epsilon}_r = 3.691$, $\tilde{\epsilon}_i = 0.217$) at $f = 350$ GHz for angle of incidence between 0° and 90° .

2.5.2 Dependence on the Grazing Angle

The minimum in Γ_{TM} occurs at the Brewster's polarization angle (*cf.* Fig. 2.11), the angle where the transmitted wave is completely absorbed by the surface but a sudden increase in the response of vertical polarization is witnessed again with further increase of the grazing angle. In other words, the grazing angle marks the sign change in the real part of the reflection coefficient for parallel polarization. Furthermore, in case of very small grazing angle ($\Theta_i \approx 0^\circ$), we have

$$\Gamma_{TE} = \Gamma_{TM} \quad (2.11)$$

Conversely, when ($\Theta_i \approx 90^\circ$), we get

$$\Gamma_{TE} = -\Gamma_{TM} \quad (2.12)$$

2.5.3 Dependence on Frequency

The Fresnel equations have the frequency dependent refractive index and absorption coefficient in the equation of wave impedance Z , which means the reflectivity is also frequency dependent. At THz frequencies, however, the refractive indices do not vary considerably with frequency

for common indoor building materials [31]. In contrast, a significant increase of the absorption coefficient with the frequency is conspicuous.

Coverage Simulations Attributive of Reflection Order of Multipaths

Fig. 2.12 illustrates the reflection order of path dependent coverage simulations in terms of relative received power. The simulation setup depicted in Fig. 3.6 (second environment, *cf.* Sec. 3.3) is 7 m in (*length*) x 7 m in (*width*) x 3 m in (*height*). An access point (TX) is assumed at the points $x = 6$ m, $y = 1$ m, $z = 2$ m. Coverage maps are simulated with ray-tracing for $x = 0.125 \dots 6.875$ m and $y = 0.125 \dots 6.875$ m in discrete steps of $\Delta x = \Delta y = 0.125$ m in x and y directions, respectively. All walls, the ceiling and floor are made of smooth plaster (i.e., $\sigma_h = 0$ mm) with $\tilde{\epsilon}_r = 3.691$, $\tilde{\epsilon}_r = 0.217$. The furniture (tables, chairs, cabinets, wardrobe) is made of identical pine wood with $\tilde{\epsilon}_r = 1.734$, $\tilde{\epsilon}_r = 0.073$ and considered smooth as well. The three glass windows with $\tilde{\epsilon}_r = 6.656$, $\tilde{\epsilon}_r = 0.539$ are also modeled smooth. Isotropic omnidirectional antenna are used at both TX and RX ends. There are 729 receiver points (RXPs) covering the entire office. Taking into account the worst-case coverage, all chosen RXPs are 0.25 m in height. Ground reflections from the floor are also included. The diffraction around the edges and wedges is disregarded for an isolated quantification of the reflection orders. Next, in case of Fig. 2.12(d), up to three reflections (i.e., thrice reflected paths) are considered. We neglected the multipaths that leave the office room and bounce back by setting the receiver sensitivity level to -140 dBm. Such multipaths are too weak to be considered for coverage map studies at THz frequencies.

Note that the power of all incident rays is summed up at each point to average out unwanted multipath fading effects. Multipath propagation in indoor environments is strongly affected by the dimensions of the surroundings and density of furniture. From Fig. 2.12, we can deduce that a reliable high-speed communication link can only be maintained when and if the THz communication system relies on reflections as a backup. The direct paths could be blocked completely by the intervention of mobile objects into the direct path with wavelengths around 1 mm at 300 GHz, such scenario has to consider multiple reflections from the walls, floor and the ceiling. The key finding from these simulations is that; a better coverage can be achieved, if transmission paths with one and two reflections from walls, ceiling and floor are considered. Recently, in experiment [32] the first specular NLoS link from a typical indoor wall has been demonstrated at (discrete) THz frequencies, opening up a new horizon of scientific investigation

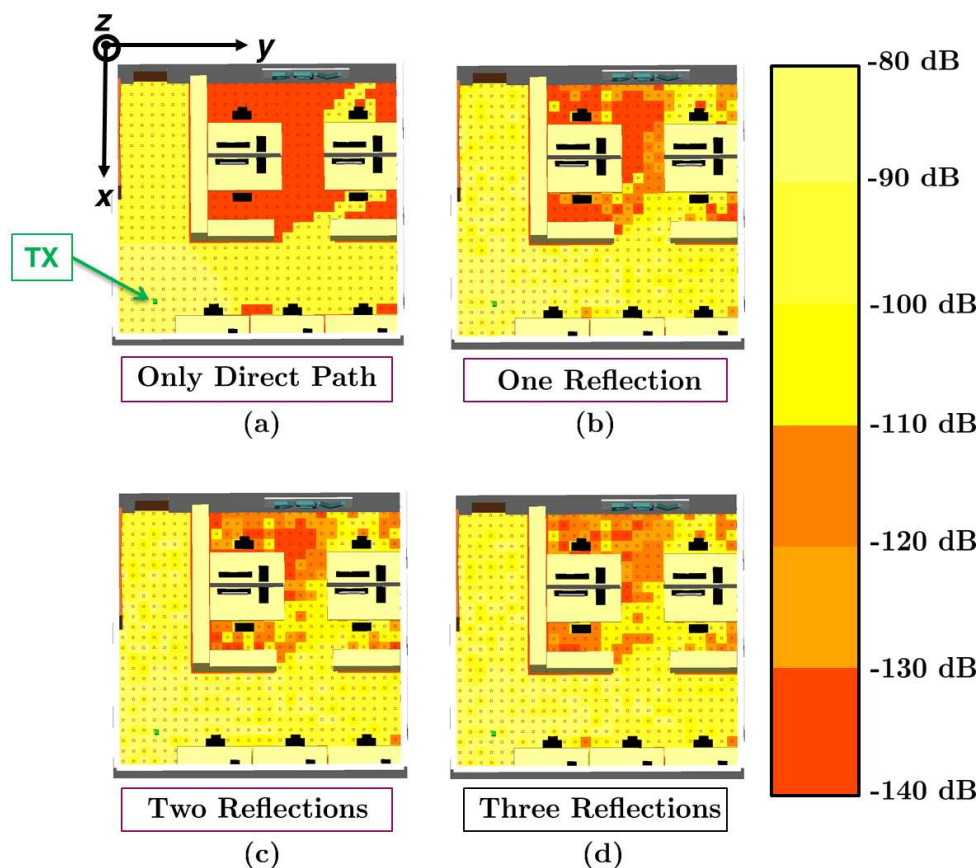


Figure 2.12: Coverage maps attributed of direct path and reflection order of multipaths. TX at the position $x = 6$ m, $y = 1$ m, $z = 2$ m, 729 RXPs are 0.25 m in height, and at $f = 300$ GHz.

for NLoS THz communications. However, due to notably larger path loss and high reflection losses, higher order of reflections (i.e., 3rd order) may not contribute to the multipath THz channel.

2.6 Reflection by a Rough Surface

Reflection by a rough surface or diffuse reflection is the most critical and important propagation phenomenon at THz frequencies. The diffuse reflection of EM waves is merely dependent on the surface roughness, incident angles, complex refractive index of materials and wavelength at hand. At THz frequencies, diffuse reflection tends to be particularly strong due to the increased surface roughness and this causes an additional attenuation even in the specular direction of reflection (*cf.* Fig. 6a–b in Ref. [19]). Generally speaking, when an EM wave is incident on a rough surface, the phenomenon of diffuse scattering splits the wave into a specular and many

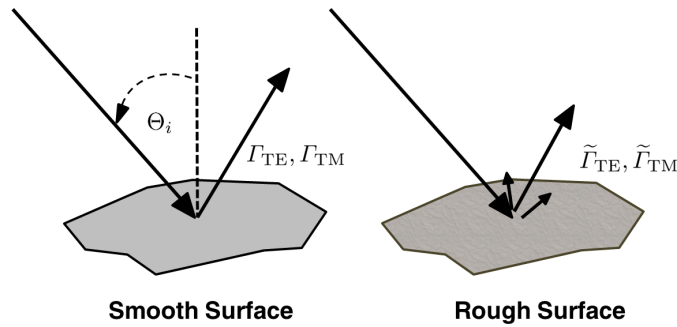


Figure 2.13: Specular reflection by a smooth (left) and diffuse reflections by a rough (right) surface.

scattered paths. When a wave is scattered, the resulting reflections occur in many directions, though certain privileged directions may receive more energy as depicted in Fig. 2.13. It is noteworthy to mention that we deal with *random rough surfaces* throughout this dissertation. The reason is straightforward, the shape of the indoor rough surfaces met in practise can merely be described by a random function of coordinates, hence, described statistically. Henceforth, the diffuse scattering from indoor surfaces should also be dealt as a statistical problem for finding the statistical characteristics of the scattered field (distribution functions, moments, correlation functions, etc.) from the statistical properties of the real physical surface [33].

Additionally, the surface topography of any real indoor material reveals that we are actually not encountering periodic surfaces. Likewise, even little violations of periodicity lead to qualitatively unique phenomena, namely, disappearance of specular lobe and distortion of the side lobes. Besides, it is nonessential to investigate the fine structure of the scattered field, and a knowledge of certain parameters of the reflected signal, averaged over a whole class of surfaces and reflecting objects, proves sufficient [33]. As a matter of fact, the statistical approach to the solution of scattering problems from a rough surface received broad acceptance in the past [30], [34]– [37].

2.6.1 Basic Geometry of Scattering

Let us assume the incident field E_{TX} , a harmonic plane wave of unit amplitude, is incident on the random rough surface element dS . The elevation angle of incidence is represented as Θ_i and the elevation and azimuth reflected angles in the scattered region as Θ_r and Θ_s , respectively. To avoid confusion while representing single scattered ray in a basic geometry, we actually need two reflection angles to define it. One angle (Θ_r) which goes from the normal (*cf.* Fig. 2.14, it is z -axis) and the other angle (Θ_s) which goes from the incident plane (it is y -axis). However,

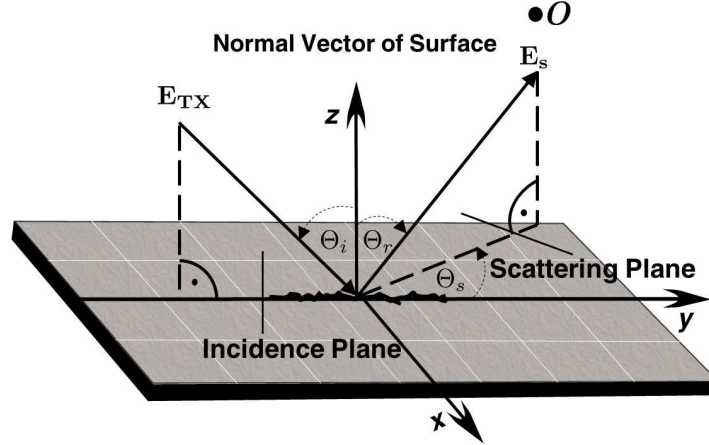


Figure 2.14: Illustration of the basic scattering geometry.

there are various other scattered rays also, not displayed in the figure. The angles are measured with respect to the z -axis as schematically shown in Fig. 2.14.

Let the observation point O is far above the selected rough surface to fulfil the far-field condition. The scattered field at the receiving point O has the following expression:

$$E_{\text{Scatt}}(O) = \left[G_{\text{Scatt}}^{\text{RX}} \right]^* \mathbf{R} G_{\text{Scatt}}^{\text{TX}} L_{\text{Scatt}} E_{\text{TX}} \quad (2.13)$$

Notably, for diffuse scattering from rough surfaces now the terms ζ_1 and ζ_2 in \mathbf{R} are not equal to zero. Rather, it is determined by the perturbation theory [38]. Moreover, due to the rough surface, the Γ_{TE} and Γ_{TM} are also changed in \mathbf{R} . Please see the modified reflection coefficients in Sec. 2.5.3.

2.6.2 Statistical Description of Rough Surface

A surface categorized as rough in macro-scale might be smooth in micro-scale and vice versa [39]. Perhaps, surfaces can be rough in various ways, i.e., they can be periodically rough like sinusoidal, saw-tooth or rectangular. Nevertheless, the surfaces just mentioned have one common thing — *they produce a scattered field*. In consequence, there is a need to describe a rough surface accurately and concisely. In more general terms, the physical characteristics of a random rough surface are described by its simplest statistical functions, like the height and slope distribution functions. These can be computed as non-cumulative or cumulative. Basically, these functions are computed as normalized histograms of the height or slope values. Note that the height and slope distribution quantities belong to the first-order statistical quantities,

2.6. Reflection by a Rough Surface

thus, describing only the statistical properties of the individual points. To simplify the discussion, a rough surface can be defined with the surface height having a non-zero variance $\sigma_h \neq 0$ with respect to the mean height \bar{h} , which constitutes an absolutely smooth reference surface. In Fig. 2.15, we show a rough surface with standard deviation height of the surface roughness $\sigma_h = 0.10$ mm, whilst the corresponding surface height histogram is illustrated in Fig. 2.16. The average surface height \bar{h} or the 1st-moment of the random variable $h(\mathbf{r})$ at a position \mathbf{r} is assumed zero. The $\bar{h} = 0$ mm for any position on the surface warrants that the random field $h(\mathbf{r})$ is homogeneous.

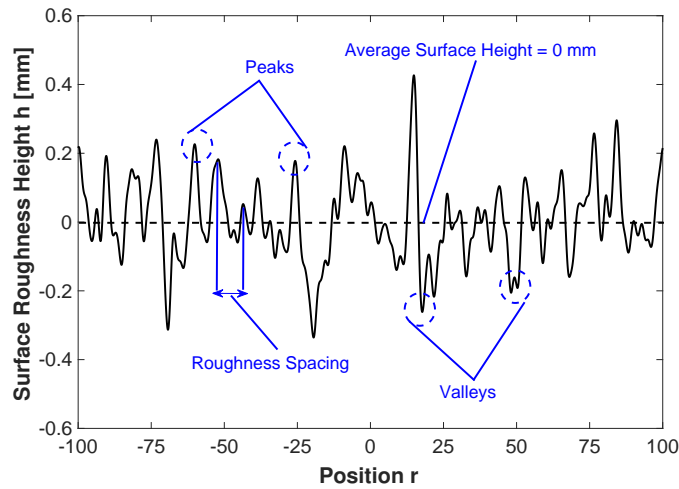


Figure 2.15: Rough surface with $\sigma_h = 0.10$ mm. The dotted lines in the figure indicate the average surface height positions.

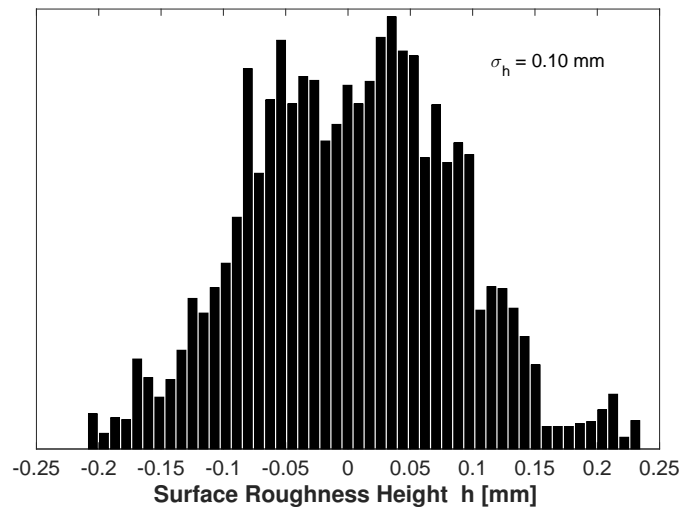


Figure 2.16: Histogram of rough surface with $\sigma_h = 0.10$ mm from the Fig 2.15.

2.6.3 The Rayleigh Method

To account for decrease in the reflected energy in specular direction due to the roughness of materials in the THz range, Fresnel reflection coefficients must be multiplied by the Rayleigh roughness factor [30]. Namely, the field reflected from the rough surface is reduced from that of a smooth surface by this factor. Thus, the scattering losses for the specular reflections are equal to the Rayleigh roughness factor (ρ_{spec}) expressed as

$$\rho_{\text{spec}} = e^{-\frac{g}{2}} = \exp\left(-\frac{8\pi^2 f^2 \sigma_h^2 \cos^2 \Theta_i}{c^2}\right), \quad \rho_{\text{spec}} \in [0, 1] \quad (2.14)$$

where,

$$g = \sigma_h^2 (2\pi f/c)^2 (\cos(\Theta_i))^2 \quad (2.15)$$

or

$$g = k^2 \sigma_h^2 (\cos(\Theta_i) + \cos(\Theta_r))^2$$

Here, g is the roughness parameter of a material, f the frequency of incident wave, σ_h the standard deviation height of surface roughness, Θ_i the angle of incidence and reflection relative to surface normal, and c the velocity of light. The parameter g , an interesting and simple means of estimating the degree of EM roughness of a surface, i.e., if a surface can be qualified as smooth ($g = 0$), slightly rough ($g \ll 1$), moderately rough ($g \geq 1$), or very rough ($g \gg 1$) as depicted from its reflection and scattering pattern in Fig. 2.17.

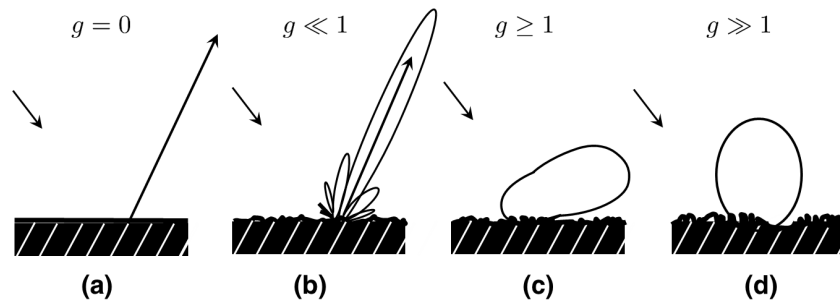


Figure 2.17: Transition from specular reflection to diffuse scattering. The surfaces are: (a) smooth, (b) slightly rough, (c) moderately rough, and (d) very rough. Figure adapted from Fig. 5.1 in [30].

From Eq. (2.14), it is apparent that the roughness parameter g of a material depends on standard deviation height σ_h , angle of incidence Θ_i , and the carrier frequency f . Further, the consequence

of cosine function in the g formula indicates that the surface roughness impact for an impinging wave is lower towards higher angles of incidence. The corresponding g values of the rough materials, i.e., plaster x1, plaster x2, plaster x3 used in our scenario are illustrated in Fig. 2.18 for the frequency range between 100 GHz and 1 THz for two angles of incidence: 30° and 45° .

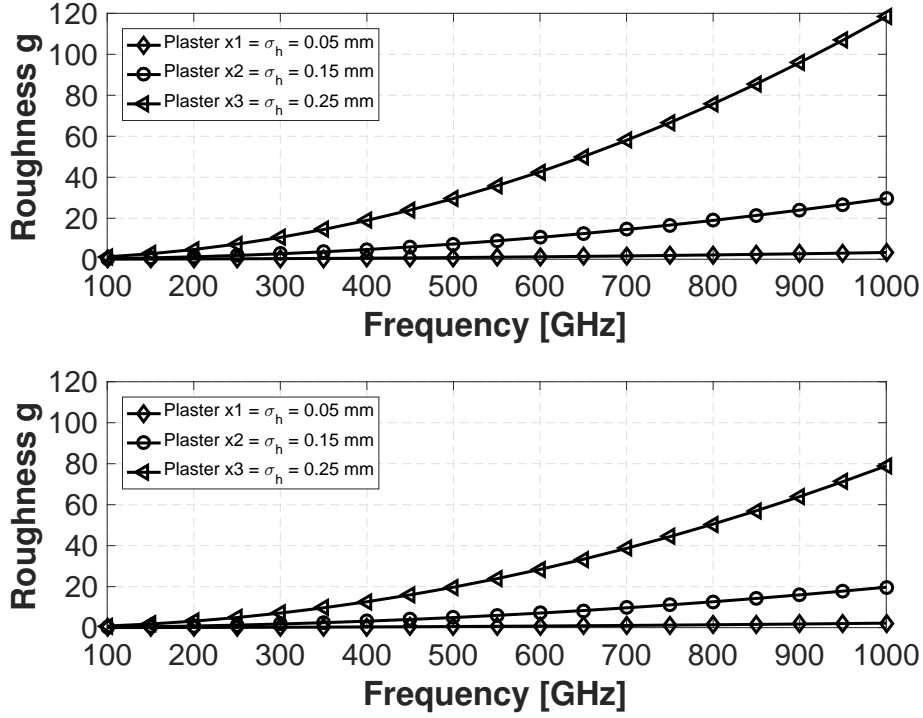


Figure 2.18: Calculated roughness parameter g of three different plasters ($\tilde{\epsilon}_r = 3.691$, $\tilde{\epsilon}_r = 0.217$) for angles of incidence 30° (top) and 45° (bottom).

The modified reflection coefficients for parallel $\tilde{\Gamma}_{TE}$ and perpendicular $\tilde{\Gamma}_{TM}$ polarizations in the presence of rough surfaces taking into account the different standard deviation heights are then

$$\tilde{\Gamma}_{TE}(f, \Theta_i) = \rho_{\text{spec}} \Gamma_{TE}(f, \Theta_i) \quad (2.16)$$

also

$$\tilde{\Gamma}_{TM}(f, \Theta_i) = \rho_{\text{spec}} \Gamma_{TM}(f, \Theta_i) \quad (2.17)$$

From Eq. (2.17), it is apparent that $\tilde{\Gamma}(f, \Theta_i)$ is always smaller than $\Gamma(f, \Theta_i)$. In [18], the THz-TDS is used to measure the absorption coefficient and refractive index of rough surfaces (i.e., granular wallpaper and concrete plaster). Then, the reflection coefficients for the specular reflection are calculated using the conventional Fresnel equations. Next, the modified reflection

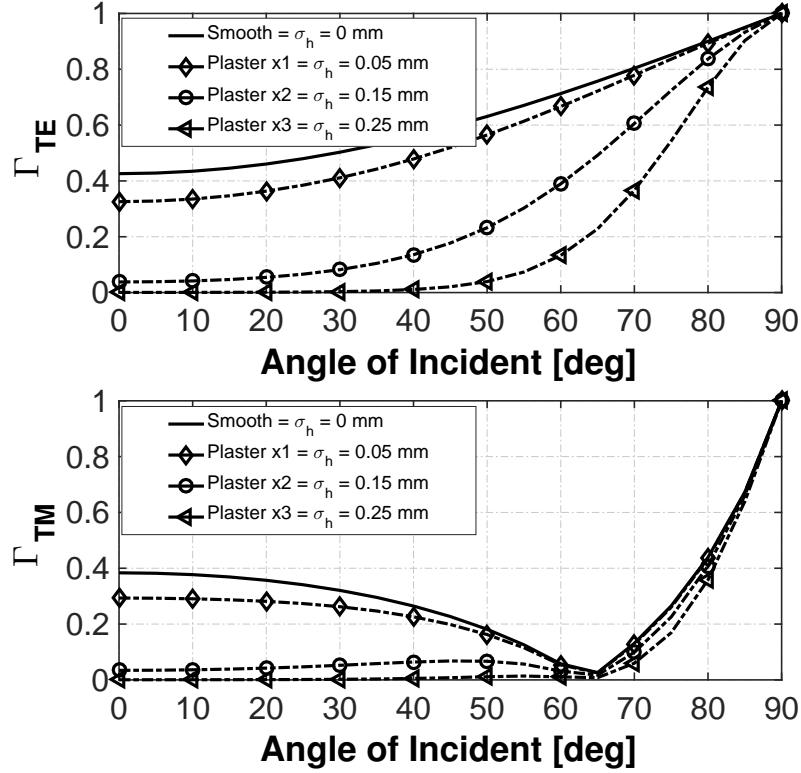


Figure 2.19: Magnitude of (modified) reflection coefficient for angle of incidence between 0° and 90° at a frequency of 350 GHz for TE and TM polarized wave (material: plaster).

coefficients $\tilde{\Gamma}$ are calculated from Eq. (2.16) and Eq. (2.17) owing to the roughness ($g \neq 0$) of the investigated samples. By using the aforementioned procedure, the coverage simulation results in [18] show good agreement with measurements upon comparison. Please note that for materials which are optically smooth, the conventional reflection coefficients Γ do conform with the measurements for long wavelengths (i.e., at lower frequencies) but deviate for shorter wavelengths (i.e., at THz frequencies) by virtue of the roughness of the optically smooth indoor materials that become evidently rough at THz frequencies and thus scatter. Consequently, this entails channel models with surface roughness at THz frequencies and the novel scattering algorithms [16]. Thus, in [18] this deviation is rectified by including the Rayleigh roughness factor. We now employ this to calculate magnitude of the reflection coefficients Γ_{TE} and Γ_{TM} , shown in Fig. 2.19 as a function of angle of incidence at the center frequency 350 GHz, for the three rough plasters used in our study's scenario depicted in Fig. 2.20. The solid line (*cf.* Fig. 2.19) is used as a benchmark for comparing smooth (i.e., $\sigma_h = 0$) and rough plasters.

Once $\Gamma(f, \Theta_i)$ and $\tilde{\Gamma}(f, \Theta_i)$ are determined, then rearrangement of Eq. (2.16) or (2.17) evaluates the Rayleigh roughness factor ρ_{spec} as

$$\rho_{\text{spec}}(f, \Theta_i, \sigma_h) = \frac{\tilde{\Gamma}(f, \Theta_i)}{\Gamma(f, \Theta_i)} \quad (2.18)$$

Coverage Simulations Attributive of Roughness

The diffuse reflection of EM waves is merely dependent on the surface roughness, incident angles, complex refractive index of materials and wavelength at hand. At THz frequencies, diffuse reflection tends to be particularly strong due to the increased surface roughness and this causes an additional attenuation even in the specular direction of reflection. In the above figures, we have theoretically evaluated the influence of standard deviation height σ_h in case of smooth and rough plasters. However, in order to investigate the influence of different materials along with their roughness on the 300 GHz propagation channel, simulations in a realistic environment are indispensable. This expedites the perception of plausible TX/RX constellations and assists in spotting out the materials that affect the quality of the THz links as a result of scattering.

These simulations are carried out in an empty office room of 7 m (*length*) x 7 m (*width*) x 3 m (*height*) which is an LoS cubic scenario. The TX is placed at the points $x = 6$ m, $y = 1$ m, $z = 2$ m. There are once again 729 RXPs. Taking into account the table top terminals, RXPs are chosen to possess a *height* = 0.75 m. All walls and the ceiling are made of plaster identical to the description already given previously in the coverage simulations except for the floor. The floor is covered by smooth polyvinyl chloride (PVC) with $\tilde{\epsilon}_r = 2.788$, $\tilde{\epsilon}_i = 0.069$. Due to the smooth flooring, only specular reflections from the floor are included. Up to twice-reflected paths (i.e., 2nd order) are considered in the modeling. To maximize scattering contributions and lower scattering losses, vertically polarized omnidirectional antennas are chosen at both TX and RXPs. The diffraction (i.e., no objects) and transmission are neglected. Receiver sensitivity level is once again set to -140 dBm.

The results in Fig. 2.20 show the impact of surface roughness on the THz propagation channel in terms of coverage maps obtained from ray-tracing simulations under LoS scenario. As deduced, the roughness (i.e., variable roughness σ_h ranging from 0.05 to 0.25 mm) peculiarly persists without any noticeable influence on the relative received power, where an average attenuation of around 91.72 dB is recorded ignoring the surface roughness. Regardless of the direct path, the scattering is quite significant in the points near to the walls and distant from the TX. Nevertheless, the average attenuations for $\sigma_h = 0.05$ mm, $\sigma_h = 0.10$ mm, $\sigma_h = 0.15$ mm, $\sigma_h = 0.20$ mm and $\sigma_h = 0.25$ mm are recorded as 92.08, 92.72, 93.13, 93.30 and 93.38 dB,

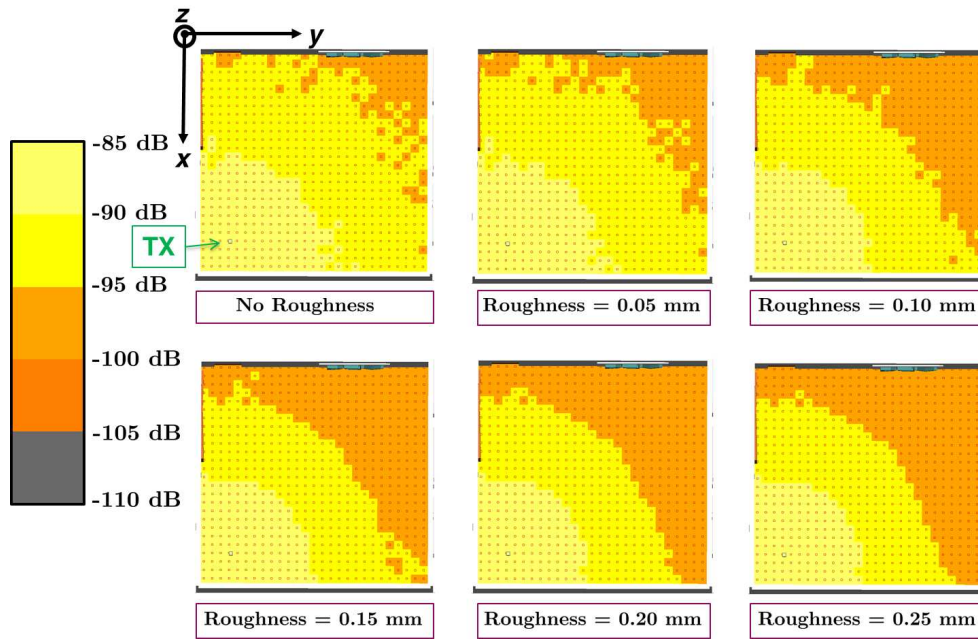


Figure 2.20: Coverage maps attributive of roughness dependence on the total received power at 300 GHz for LoS scenario. TX at the position $x = 6$ m, $y = 1$ m, $z = 2$ m and 729 RXPs are 0.75 m in height.

respectively. Intuitively, these almost identical average attenuations are perhaps highlighting the effect of a dominant LoS path components (direct path) compared to the scattered channel paths with almost negligible effect.

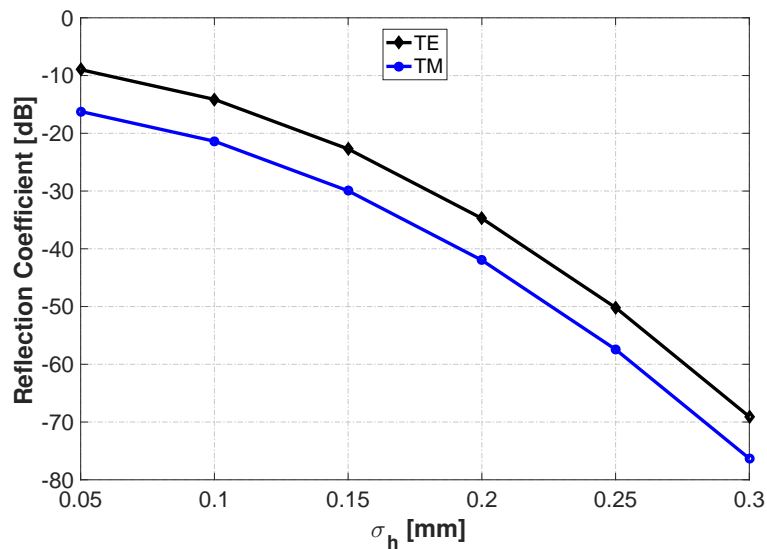


Figure 2.21: Calculated magnitude of reflection coefficients \tilde{I}_{TE} and \tilde{I}_{TM} for specular direction on rough plaster ($\tilde{\epsilon}_r = 3.691$, $\tilde{\xi}_r = 0.217$) at $f = 300$ GHz for incidence angle $\Theta_i = 45^\circ$ and standard deviation heights σ_h from 0.05 mm to 0.30 mm.

Furthermore, in Fig. 2.21 we calculate the modified reflection coefficients $\tilde{\Gamma}_{\text{TE}}$ and $\tilde{\Gamma}_{\text{TM}}$ of the corresponding material (rough plaster) used in all walls and ceiling taking into account the different standard deviations of surface height to identify exactly how the material is impairing the quality of THz links for first-order reflections.

2.6.4 Depolarization

Reflection by a rough surface is not only scattering the field towards non-specular directions but also depolarizing it. This is the change in polarization of the incident wave on being scattered at the surface, proportional to the surface roughness of the material in a distinctive manner. Thus, one should distinguish between depolarization that occurs due to the scattering effects from a rough surface and geometrical depolarization. Both of these polarization effects can be measured in terms of the cross-polar discrimination ratio (XPD), where an orthomode transducer enables the vertically polarized transmitting signal to capture both horizontal (cross-polar) and vertical (co-polar) signal components at the receiver end. The XPD is defined in [40] by the expression

$$XPD = 10 \log_{10} \left(\frac{P_V}{P_H} \right) \quad (2.19)$$

where P_V and P_H correspond to the received power of the vertical and the horizontal component, respectively. In [40], it is shown that the depolarization is more dominant in case of rough surfaces than that caused by smooth surfaces. Besides, the XPD becomes bigger for higher incident angles but no dependency on distance was observed. Similarly, in [41], it is shown that depolarization arises in backscattering from dielectric rough surface. However, in [42] it is concluded that neither depolarization nor polarization dependence is found in scattering from a perfectly conducting rough surface. Note that rough surface is often assumed to be perfectly conducting such that the boundary condition is satisfied. Perhaps, the scattering from a perfectly rough surface is also a convenient starting point as an assumption for the development of mathematical models.

2.7 Diffraction

Diffraction occurs when an obstacle with sharp irregularities (i.e., wedges, edges and circular cylinders) and large dimensions as compared to the propagated wavelength comes between

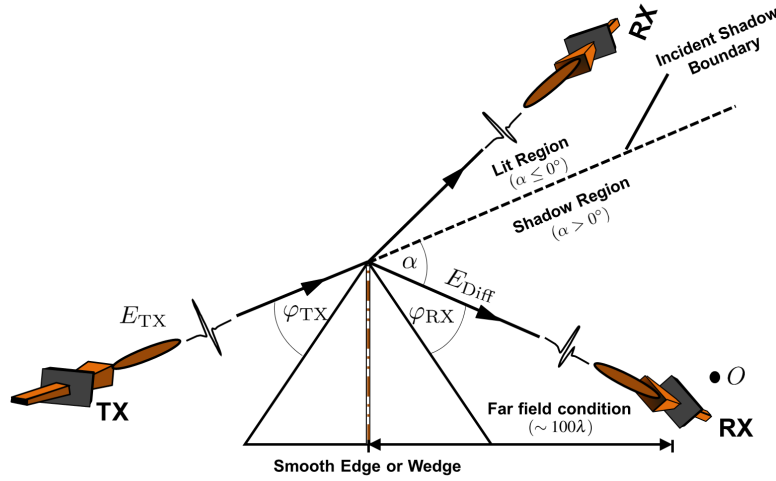


Figure 2.22: Geometry for smooth edge/wedge diffraction.

TX and RX. Even a moving person blocking the path of an EM wave can be considered as a diffracting object at THz frequencies [43]. Apart from persons, the diffracting objects in an indoor environment are metallic or wooden edges of file cabinets, bookshelves, cupboards, tables, workplace-privacy panels, open windows and doors. Due to diffraction phenomena, the propagated wave bends around the obstacle and continues propagating in the geometrical shadow region (or incident shadow boundary) behind the obstacles, as evident from Fig. 2.22.

The well-known models with analytical description of the diffraction behaviour of many different objects are the uniform theory of diffraction (UTD) [44] and the knife edge diffraction (KED) [38]. The first approach not only holds valid for various objects with arbitrary dielectric parameters, but also accounts for polarization in contrast to the latter approach. However, the complexity of UTD is very high and it requires numerical solutions for path loss [45]. The first order diffracted field at the receiving point O can be expressed from [24] as

$$\mathbf{E}_{\text{Diff}}(O) = \left[\mathbf{G}_{\text{Diff}}^{\text{RX}} \right]^* \mathbf{G}_{\text{Diff}}^{\text{TX}} D(\varphi_{\text{TX}}, \varphi_{\text{RX}}) Q(d_{\text{TX}}, d_{\text{RX}}) L_{\text{Diff}} \mathbf{E}_{\text{TX}} \quad (2.20)$$

Based on (Eq. 2.20), \mathbf{E}_{Diff} depends on D and Q . The diffraction coefficient D is determined by diffraction angles at objects and the boundary conditions. Likewise, the geometry factor Q considers the distance from TX and RX to the edge or wedge. Thus far, a very few angular dependent diffraction measurements at THz frequencies have been reported [43], [46]– [48]. In [48], the analysis of the frequency dependency on wedges (metallic cuboids) between 275 and 325 GHz is experimentally studied, and no significant dispersion of the diffracted wave is

noticed. Moreover, the measurements show good agreement with the calculations based on the UTD regardless of the polarization and angular range. To summarize, the UTD proves well-suited for the diffraction modeling at 300 GHz from smooth surfaces. *However, the diffraction from rough surfaces at THz frequencies has not been studied yet.*

2.8 Channel Performance at THz Frequencies

Fact that many radio scientists around the globe are interested in THz regime for wireless communications is due to the overwhelming extreme wide bandwidths available which is essential in terms of high capacity, flexibility and explicitly attractive for Tbps wireless applications. Although scientists have to overcome certain device (components) as well as nontrivial wireless channel challenges, but steadily paving the way for the ever-accelerating technological advancement. For instance, an ultrahigh-speed IC for wireless front-end capable of wireless transmission of 100 Gb/s in a 300 GHz band is recently reported [49] and this mixer circuit applies a unique proprietary high isolation design technology with an Indium phosphide high electron mobility transistor (InP-HEMT). This unique high isolation technology enlarges the transmission bandwidth and improves the signal-to-noise ratio (SNR). As such, the compound semiconductor transistors (i.e., GaAs, InP technologies) with superior high frequency performance are particularly the choice of fortune for mm-wave and THz frequencies, but low cost and large volume manufacturing is unforeseeable. Nevertheless, in cell-phone amplifiers, the largest production volume is indeed that of GaAs-based heterojunction bipolar transistor (HBT). In addition, Si-based devices (SiGe and CMOS) are not out of picture. Recently, a CMOS single-chip THz transceiver that can transmit or receive digital data at 80 Gb/s has been reported [50]. Moreover, SiGe technology is also dominant for delivering low power commercial solutions for applications like local WiFi amplifiers and potentially for phased-array systems for 5G communication radios. Note that Si benefits from low-cost and tremendous integration capability with 8–12 levels of interconnect. Meanwhile, the maximum oscillation frequency f_{max} of the latest compound semiconductor transistor exceeds 1 THz [51, 52], and f_{max} of the SiGe bipolar transistor exceeds 500 GHz [53]. To summarize, several other functional circuits and components such as amplifiers [54, 55], oscillators [56, 57], modulators/demodulators [58, 59], and phase locked loops [60, 61] are reported for THz applications.

Let us quantify the achievable data capacity of a short-range wireless communication of THz wireless link of 5 m based on a simple link budget using Friis formula. The simplified

link budget equations which determine the received power P_{RX} and the SNR_{dB} at the RX can be expressed as

$$P_{RX} = P_{TX} + G^{TX} + G^{RX} - 20 \log \left(\frac{\lambda_c}{4\pi d} \right) - (\alpha_a(f_c) d) - X_m \quad (2.21)$$

The Shannon's data capacity C can be represented as

$$C = B \log_2(1 + SNR_{dB}) \quad (2.22)$$

where SNR_{dB} at the RX is

$$SNR_{dB} = P_{RX} - (N_0 + 10 \log(B) + NF + M) \quad (2.23)$$

where P_{TX} is the transmitted power, G^{TX} and G^{RX} are the gains for transmitter and receiver antenna, respectively. λ_c and d are the wavelength at hand and distance, respectively. α_a is the atmospheric attenuation at frequency f_c and X_m represents the excess loss, not included in the FSPL. B is the system noise bandwidth, NF and M are the noise figure of the receiver and the system margin, respectively. Note that for simplicity, all losses and antennas are at 290 K and hence, the effect of losses is simply to reduce the signal level while the noise stays at the same level. Besides, the thermal noise is assumed as additive white Gaussian noise (AWGN).

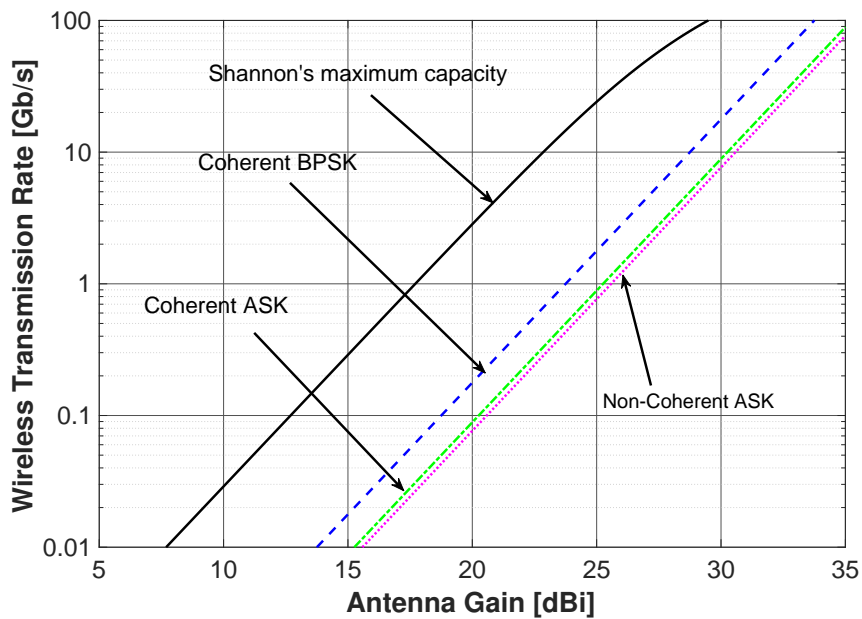


Figure 2.23: Calculated Shannon's maximum data capacity for spectral efficiency of 1 bps/Hz and available data rates at a BER of 10^{-6} for different binary modulations.

Table 2.2: Most significant parameters for Fig. 2.23.

Parameter	Symbol	Value
Transmit power	P_{TX}	0 dBm
Carrier frequency	f_c	300 GHz
Wavelength	λ_c	1 mm
Distance	d	5 meter
Atmospheric attenuation	α_a	0.01 dB/m @ f_c
Excess loss	X_m	0 dB
Noise spectral density	N_o	-174 dBm/Hz
Spectral efficiency	η	1 bps/Hz
Noise bandwidth	B	Data rate \times spectral efficiency
Total noise figure	NF	15 dB
System margin	M	10 dB
Bit error rate	P_e	10^{-6}

As previously mentioned, a spectral window centered at 300 GHz can be utilized that offers 47 GHz of continuous bandwidth, which allows a 100 Gb/s high throughput even with a simple modulation scheme. For this analysis, therefore, coherent and non-coherent amplitude-shift keying (ASK) is assumed. Meanwhile, binary phase-shift keying (BPSK) with coherent detection is also part of our analysis to calculate the required antenna gains for 100 Gb/s high throughput. The antenna gains at both sides are considered equal for simplification. Table 2.2 gives the necessary parameters used in the calculation of Shannon's data capacity considering a bit error rate (BER) of 10^{-6} .

For designing a very high speed 5 m wireless link that offers 50 Gb/s (*cf.* Fig. 2.23), the THz communication systems employ an antenna gain between 32 and 34 dBi dependent on the modulation format. It is workable as THz frequencies leading to smaller-sized RF components including antennas. For example, an antenna with a gain of 32 dBi at 300 GHz has an effective antenna aperture of about 126 mm^2 , so that even antenna arrays with a large number of antennas have a reasonable form factor. On the other hand, the physical area for the same antenna gain at 5 GHz has drastically increased, unfeasible to be integrated into consumer electronics or at user terminal, difficult if not impossible. At 300 GHz, the form factor compared to 5 GHz is at least 60 times smaller.

2.9 Development of THz Standards

In this section, we briefly discuss the current status of the regulation and standardization effort of the physical layer (PHY) for the lower THz frequency range. THz technology has come of age and the standards of IEEE 802.15.3d-2017 operating from 252 GHz to 325 GHz, designed for data rates of up to 100 Gb/s for intra-device communication (e.g., board-to-board communication), close proximity communication, wireless data centers and backhaul/fronthaul links, are already approved [62]. Two PHYs modes are defined in the specification for the THz PHY, namely, the single carrier (THz-SC PHY) and the on-off keying mode (THz-OOK PHY). The two PHYs are mapped to the distinctive advantages in supporting specific applications. For instance, the THz-SC PHY is aimed for extremely high data rates up to 100 Gb/s. Besides, it is designed to support a wide range of modulations, namely, $\pi/2$ BPSK, $\pi/2$ QPSK, $\pi/2$ 8-PSK, $\pi/2$ 8-APSK, 16-QAM, and 64-QAM. The modulations of $\pi/2$ BPSK and $\pi/2$ QPSK are mandatory for THz-SC PHY, whilst the other modulations are optional. On the other hand, THz-OOK PHY is designed to support low-cost and simple design. However, it supports a single modulation scheme, on-off keying (OOK), and three forward error correction (FEC) schemes. The Reed Solomon code is mandatory here. The standard IEEE 802.15.3d-2017 provides 69 channels with eight ranges of channel bandwidths from 2.16 GHz to 69.12 GHz.

2.10 Concluding Remarks

A thorough insight into the basic propagation mechanisms at THz frequencies is presented in this chapter:

⇒ We neglected transmission phenomenon due to the resultant several 10 dBs transmission attenuation losses for the material groups (*wood, plastic, paper, brick, glass, leather*) chosen in this study, thus limiting the transmission distance and coverage to *in-room* scenarios.

⇒ Similarly, the diffraction effect can also be neglected particularly for the indoor environments under study due a number of reasons. Depending on the modeling environment, the diffraction is either not present as in the case of *First* and *Second Environments* without furniture and reflection points, respectively. Whereas in the *Third Environment*, the diffraction is present but not taken into account to avoid elaborate computations and long simulation times spanning over a few days.

⇒ The simulation findings point out that a better coverage can be achieved only if the transmis-

sion paths with merely one and two reflections from walls, ceiling and floor are considered to attain a reliable communication link relying on these as backup.

⇒ The simulations carried out in the spectral windows reveal that the atmospheric attenuation for both LoS and NLoS scenarios in case of short-range *in-room* wireless communications can be neglected. Nevertheless, at $f = 300$ GHz (spectral window) the atmospheric attenuation for both LoS and NLoS cases is identical (0.1 dB).

⇒ The impact of candle flame on the ultra-broadband THz communication links is analyzed with three different antenna configurations (Horn-Horn, Horn-Open, and Open-Open) for two distances (0.5 m and 1 m) to demonstrate that the resulting slight attenuation in amplitude and delay in phase pose no threat in precisely localizing and characterizing the materials or objects at THz frequencies.

⇒ The coverage maps obtained from the ray-tracing simulations in case of LoS scenario unfold the peculiar pattern of scattering being significant in the points near to the walls, distant from the TX. Hence, the rough surface does not exert a dominating influence on the THz propagation channels under LoS conditions when the effect of surface roughness in the specular direction of reflection is considered.

⇒ Finally, a link budget calculation for designing a very high speed 5 m wireless link that offers 100 Gb/s discloses that the THz communication system requires an antenna gain between 32 & 35 dBi for both the transmitter and receiver.

Advances in THz Scattering Models

In this chapter, the most famous diffuse scattering theories are adopted to establish a scattered channel modeling approach and interpret the scattering phenomenon of indoor rough materials at the frequency of choice. At THz frequencies, diffuse reflection tends to be higher due to the increased surface roughness, thus causing an additional attenuation even in specular direction of reflection (by the amount that is scattered into non-specular directions). The R-R vector perturbation approach predicts diffuse reflection from optically smooth surfaces ($\sigma_h/\lambda \ll 1$), whilst B-K theories (classic and modified) in addition attempt to predict the angular distribution of the scattered field from very rough surfaces ($\sigma_h/\lambda \gg 1$). The composite rough surfaces considered in the aforementioned work have a Gaussian probability density of height and a Gaussian correlation function. Moreover, ER model has also been chosen to study the diffuse scattering phenomenon as proposed in [63]. In this approach, a sort of effective roughness is associated with the objects' infinitesimal surface element (tiles of rough material), which not only takes into account real surface roughness but also the mean and statistical values of the object discontinuities. Then, the far-field component of the wave scattered by the surface elements, i.e., the field strength and power delay profile (PDP) is computed directly from the surface element distance and orientation with simple analytical formulas. This chapter encompasses research published in [64]– [66].

3.1 Physics of Diffuse Scattering in THz

The primary indoor materials encountered in this work are only solid surfaces. A general typology of the solid surface is shown in Fig. 3.1. Besides, most solid surfaces in nature have an

inherent roughness, though they appear smooth or give a smooth feeling when touched physically. For instance, every sheet of paper (surface) in this dissertation may switch from very rough at optical wavelengths, to slightly rough at submillimeter wavelengths, and smooth at microwave wavelengths. Also, a surface that appears rough from a shorter distance may appear smooth from a longer distance. Likewise, observing the surface from different locations may change surface imperfections and a rough surface can be made to appear smooth. When studying scattering, the solid rough surfaces are firstly broken down using the surface reflection theories based on EM wave theory to distinguish between smooth and rough surfaces; further classifying them. The EM wave theory uses Maxwell's equations to study the wave propagation.

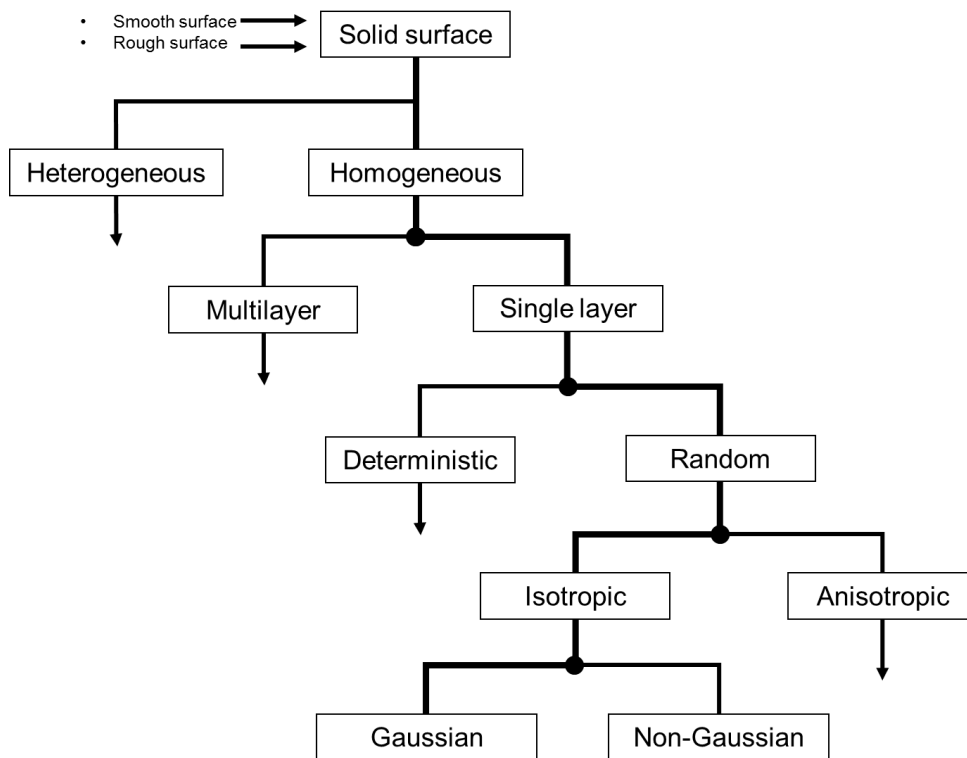


Figure 3.1: Flow chart for solid surface breakdown.

Homogeneous properties are constant throughout the solid, while heterogeneous properties vary. Moreover, keeping statistical properties of rough surfaces in view, they can be categorized as deterministic and random rough surfaces. A deterministic surface is one in which the surface height fluctuation can be expressed as a deterministic function of the surface position and the knowledge of the form of height function enables to determine the property of the whole surface. Whereas, the surface height fluctuation of a random rough surface cannot be expressed in the former way and is best described by using a random process. When elaborating the terms

isotropic and anisotropic, in the former one the surface height fluctuation is independent of the surface direction whilst a vice versa situation describes the latter one. Henceforth, one may want to use the property of roughness instead.

3.1.1 Surface and Volume Scattering

Generally, the scattered field behaviour points towards two extremes, i.e., (i) surface scattering and (ii) volume or subsurface scattering. Surface scattering is the case wherein scattering occurs only on the border surface (exterior) between two different but homogenous media with different electric and magnetic properties. The scattering on the exterior surface increases with the increase in complex permittivity, whilst the reflection and scattering pattern of surface scattering depends on the surface roughness previously shown in Fig. 2.17. Moreover, the models for single scattering are quite different from multiple scattering (*cf.* Fig. 3.2). The multiple scattering becomes prominent in case of highly scattering environments but might be neglected at THz frequencies due to the extreme reflection losses. Thus, characteristics of surface scattering are also cardinal in modeling the indoor multipath THz channel.

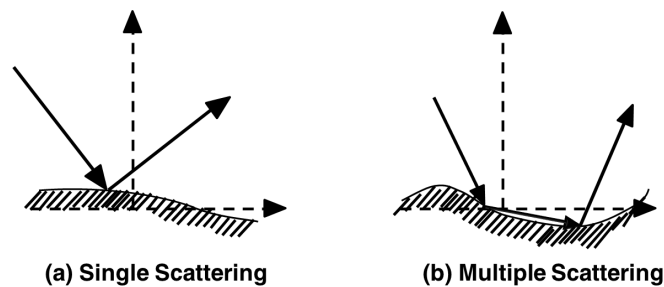


Figure 3.2: Schematic view of surface scattering.

In contrast to that, volume scattering is the scattering of EM wave in the subsurface (interior) of a material, i.e., when EM wave transmits from one medium to another, it is scattered at different levels and in different ways. Volume scattering arises when the incoming wave penetrates into a medium. One might experience volume scattering together with surface scattering and either of the two may vary depending on material properties. The *scattering coefficient* is the deciding factor to verify the contribution from the respective scattering extremes. Importantly, the choice of roughness parameters (i.e., standard deviation height and correlation length) is crucial such that the surface and volume scattering contributions are distinguishable in the angular behaviour of the total scattering pattern.

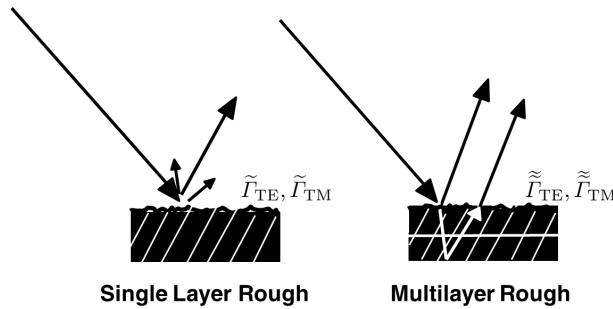


Figure 3.3: Models of single layered and multilayered surfaces.

As a rule of thumb, the standard deviation height $\sigma_h = \lambda/10$ and the correlation length $\ell_{cr} = \lambda$ are previously considered to split the two extremes. The correlation length is described later in Sec. 3.2.1. It is worth mentioning that the surface scattering contribution is most likely visible close to the specular lobe, whilst the volume scattering is independent of scattering angles, in fact almost constant everywhere in the diffuse lobe and hence, may be distinguishable at larger angles where the surface scattering becomes negligible. The diffuse reflection of a plane wave from single layered and multilayered rough surfaces is schematically shown in Fig. 3.3.

3.1.2 Coherent and Incoherent Scattering

Reflection at THz frequencies from typical indoor building materials that are slightly rough ($0 < g \ll 1$) comprises of three reflection components, i.e., the specular spike, the specular lobe, and the diffuse lobe. The manner in which an incoming wave is reflected by a surface is dependent on the microscopic shape of the surface morphology in addition to the surface roughness, incident angles, complex refractive index, and wavelength at hand. The scattering by which the phase is affected in a well-known and predictable way is called as *coherent scattering*. In other words, the scattered paths have non-random relative phases in the direction of interest. The scattering from a slightly rough surface actually yields a combination of coherent and diffuse components. However, the coherent component becomes more prominent when the surface gets smoother. On the other hand, in case of *incoherent scattering*, the scattered paths have random relative phases in the direction of interest. Moreover, the scattered path lengths are random too. Likewise, incoherent scattering is always weaker than coherent scattering.

3.2 Rough Surfaces at THz Frequencies

In this section, we interrogate the statistical description of random rough surfaces encountered in indoor environments which may have implications on the throughput of THz communication systems. The earlier discussion (*cf.* Sec. 2.5.2) encompasses surface profiles to be functions of coordinate x only and their physical characteristics are further described by one-dimensional (1D) distribution function namely height distribution function. These surfaces are termed as 1D. In fact, most common random surfaces met in practise are two-dimensional (2D) interpreted as functions of two spatial directions, i.e., the surface height h is expressed as a random function of the two coordinates x and y . Basically, the surface height distribution function describes the 2D variation in surface elevation and azimuth above an arbitrary plane. Hereupon, to approximate the scattering pattern of random rough surfaces, the roughness parameters and characteristic functions are absolutely imperative. They are categorized as Gaussian and non-Gaussian with several approaches being used to describe the statistical nature of the surface. The random rough surface considered in this study is homogeneous, single layered, isotropic and Gaussian distributed.

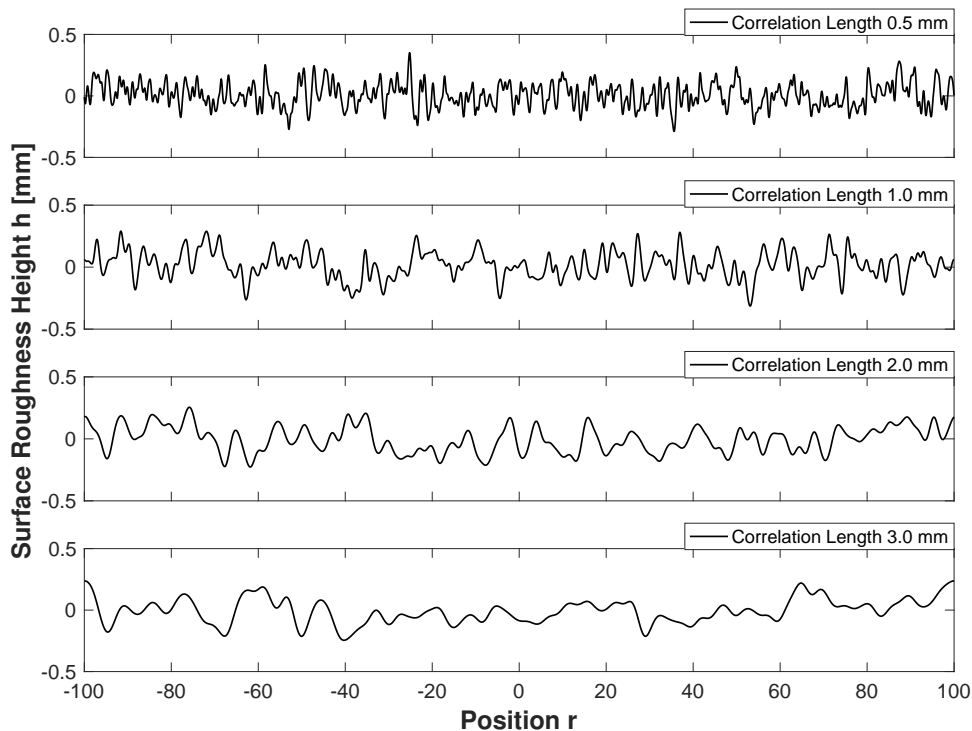


Figure 3.4: Random rough surface with the unique standard deviation height σ_h but different correlation lengths ℓ_{cr} .

3.2.1 Gaussian Rough Surfaces

The behaviour of diffuse scattering of an incoming wave from typical indoor rough surfaces inside rooms is ascertained by the statistical surface characteristics. The surface height h as already mentioned is a random function of the two coordinates x and y . The probability distribution of h then facilitates to figure out the shape of that surface. The surface heights of indoor materials used in our simulated environments (*cf.* Sec. 3.3) are assumed to be Gaussian distributed (i.e., the surface heights are normally distributed). In Gaussian height distribution, surface height fluctuates systematically around the average surface height [39]. Let us consider h normally distributed with average surface height $\bar{h} = 0$ and standard deviation σ_h . Then, the probability distribution of h is given by

$$p_h(h) = \frac{1}{\sqrt{2\pi}\sigma_h} e^{-\frac{h^2}{2\sigma_h^2}} \quad (3.1)$$

The standard deviation σ_h represents the surface roughness. This is among the most important physical parameters but insufficient to express anything about the lateral distance between the peaks and valleys of the surface profile. For instance, though apparently non identical, the rough surfaces shown in Fig. 3.4 exhibit identical Gaussian distribution (i.e., \bar{h} and σ_h are same for both surfaces). The reason for this difference in appearance is the surface correlation length ℓ_{cr} . The correlation length gives us the typical distance between two irregularities (peaks) on the surface profile. It represents the lateral dimension of a rough surface. In other words, the correlation length provides information whether the surface consists of densely packed irregularities or slowly varying features. In brief, the two statistical parameters necessary for characterizing indoor rough surfaces are: (i) the standard deviation height σ_h ; (ii) the correlation length or correlation distance ℓ_{cr} [67]. In fact, by varying these two statistical parameters one can generate surfaces that match in appearance to almost any rough surface met in practise. It is noteworthy to mention here the use of an autocorrelation function $C(\tau)$ of the surface to determine the correlation length. The autocorrelation function is of fundamental importance in describing the surface morphology of random rough surfaces. In particular, it gives the distance beyond which two surface points can be considered independent of each other. The autocorrelation function widely used and assumed mostly is *Gaussian*. This normalized Gaussian autocorrelation function for the computation of the correlation length in a single dimension is expressed from [30,

p. 81] as

$$C(\tau) = e^{-\frac{\tau^2}{\ell_{cr}^2}} \quad (3.2)$$

Here, τ is the distance between two surface points (x_1, y_1) and (x_2, y_2) randomly selected at the respective surface heights $h_1 = h(x_1, y_1)$ and $h_2 = h(x_2, y_2)$. Hence, the correlation length is the value of distance τ for which the autocorrelation function $C(\tau)$ drops to e^{-1} of its value. Most noteworthy in this Eq. (3.2) is the assumption of an isotropically rough surface. However, different rough surfaces may have different correlation functions and it is quite likely that other autocorrelation functions may give a better fit to the measured surface data.

3.2.2 Non-Gaussian Rough Surfaces

In practice, the surface height distribution is not always Gaussian. A non-Gaussian rough surface requires additional statistical parameters such as skewness and kurtosis, in addition to the standard deviation height σ_h and correlation length ℓ_{cr} [39]. Thus, the fundamental question arises as to how this non-Gaussian height distribution affects the total received and scattered power, and what scattering models may be adopted for resolving these problems at THz frequencies? Let us not delve deep in that and rather continue with the efforts mainly on Gaussian rough surfaces and keep this research gap open for the time.

3.3 Scenarios Environments

As far as propagation in a real environment is concerned, the office room BB121 in our Institute of Digital Signal Processing (DSV) has been modeled. This typical office room of 7 m (*length*) x 7 m (*width*) x 3 m (*height*) covers both LoS and NLoS scenarios. In general, NLoS links can either take the form of specular reflection, diffuse scattering (non-specular reflection) or diffracted paths. Note that the diffraction effect can be neglected particularly for the indoor environments considered in this study and shall be reasoned later within each environment in the following subsections. Up to twice-reflected paths (i.e., 2nd order) have been considered in the modeling process unless otherwise stated. We have also neglected the multipaths that bounce back and have path amplitudes lower than -200 dB by using the threshold function of ray-tracer [68]. Note that the minimum path amplitude applied to the simulations is selected to mindfully investigate the maximum influence of diffuse reflection omitting any paths with very small power levels from the latter stages of the computations.

An access point serving as the TX is positioned in a corner of the office just below the ceiling at the points $x = 6$ m, $y = 1$ m, $z = 2$ m. The transmitting antenna is kept away from any obstructions in order to provide maximum coverage. The transmit output power is 0 dBm. Taking into account the table top terminals (i.e., laptops, tablets and cellular phones), all RXs are chosen to have the 0.75 m height, unless otherwise indicated. Moreover, the simulations are performed with isotropic omnidirectional antennas at both TX and RX with radiation pattern in the azimuth plane to realize an estimation of the maximum occurring multipath influence, despite the demand of the THz frequencies for directional antennas of high gains. It is noteworthy to mention that the directional antenna though supports the multipath suppression and the temporal dispersion, but simultaneously shows a high sensitivity against mispointing. Please refer to [69] for antenna directivity impact and [70] for misalignment impact on THz indoor channel characteristics.

The ceiling and walls are covered with rough plasters given in Table 3.1 possessing identical electrical parameters but with different statistical surface parameters of standard deviation height and correlation length. The key idea is to use realistic statistical surface parameters measured by the authors in [18], and by varying these statistical parameters of rough plasters our focus is to investigate and demonstrate the influence of degree of roughness on the 300 GHz propagation characteristics. The floor is made of concrete and covered with ideally smooth PVC, unless otherwise indicated. Hence, due to the smooth flooring, only specular reflections are included from the floor. In order to attain coverage of the whole office, maximize scattering contributions and lower scattering losses, vertically polarized antennas are chosen at both TX and RXs ends. The three glass windows 1.65×1.7 m² each are modeled. These windows are 1.05 m above the floor and separated by a distance of 0.45 m from each other. The white board on the wall is an inactive object in the simulation environment. In Fig. 3.6, the pine wood wardrobe of dimensions $2.25 \times 2.6 \times 0.1$ m³ is clearly depicted. The wooden door towards the corridor is 2.1 m high and 1.05 m wide. The other comparatively smaller door is 1.9 m high and 0.8 m wide.

First Environment (Modeling)

At THz frequencies, the environment where channel modeling and measurements are of great interest are offices, residential structures, conference rooms, corridors and libraries with distance up to 10 m. The simulated model of an empty office shown in Fig. 3.5 is an LoS cubic

scenario. The ultimate goal of this empty office model is to efficiently yield accurate predictions on radio propagation key statistics including complex impulse responses, received signal strengths for mobile locations, angular spreads, delays of direct/indirect rays, electric and magnetic field strengths, and interference measures. Besides, this empty environment is also the choice of fortune to study the propagation channels when only the impact of roughness on THz ultra-broadband channel is the focus of investigation. The line-of-sight receiver (RX-LoS) is chosen to have the 0.75 m height at the points $x = 2$ m, $y = 4.4$ m, $z = 0.75$ m. Hereupon, the TX and the RX have a separation distance of 5 m. The diffraction in this empty office scenario is not considered (i.e., no furniture).

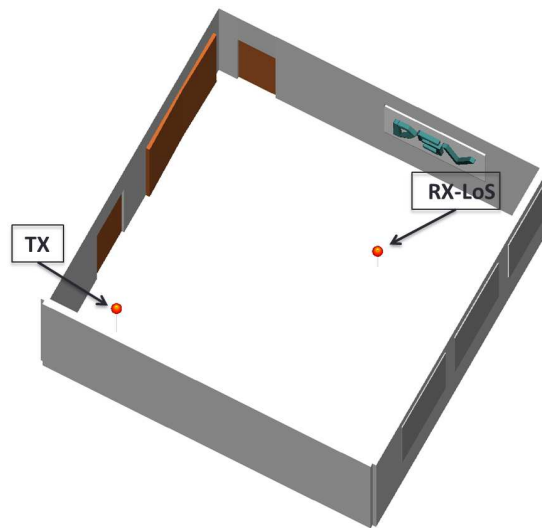


Figure 3.5: 3D view of simulated empty office room BB121 (*First Environment*).

Second Environment (Modeling)

Figure 3.6 shows a simple environment which ascertains both LoS and NLoS scenarios. The RX-LoS and the non-line-of-sight receiver (RX-NLoS) are chosen to have the 0.75 m height each at the points $x = 3.5$ m, $y = 4.45$ m, $z = 0.75$ m and $x = 1.7$ m, $y = 2.75$ m, $z = 0.75$ m, respectively. The empty workplace has a height of 0.7 m, width of 1.8 m and length of 0.8 m. This workplace is separated by metallic panel of 1.8 m x 0.55 m dimensions and pine wooden tables with metallic legs. The TX and the two RXs are 5 m apart. This environment is the core for all single-input single-output (SISO) propagation results. *Please note that no diffraction is observed when conducting simulations in the presence of an empty work space. The reason being the absence of any reflection points that occur near sharp edges and wedges.*

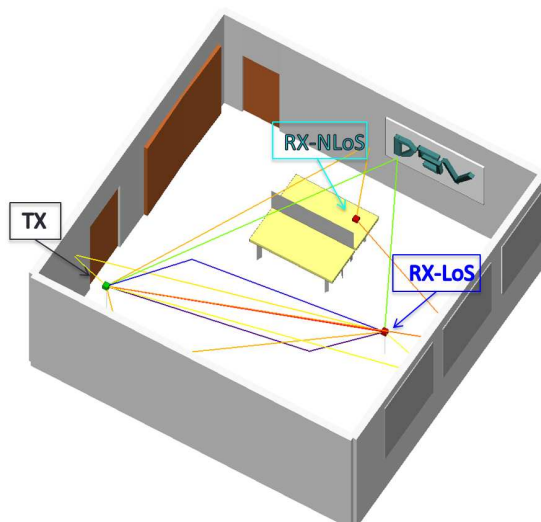


Figure 3.6: 3D view of office room BB121 with an empty work place (*Second Environment*).

Third Environment (Modeling)

Fig. 3.7 illustrates the third environment which is rather complex. The seven workplaces have a height of 0.7 m, width of 1.8 m and length of 0.8 m each. These workplaces are separated by metallic panels of 1.8 m x 0.55 m dimensions and pine wooden tables with metallic legs. There are five file cabinets, each having dimensions 1.5 x 1.6 x 0.4 m³ and characterized by 3 cm thick pine wood. In order to reduce the complexity of the environment, all desktop computers and TFTs are modeled with an identical material of polycarbonate (PC).

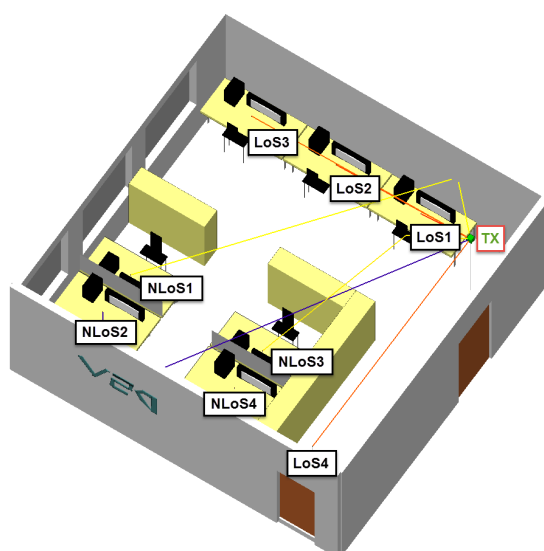


Figure 3.7: 3D view of office room BB121 with seven (7) work places (*Third Environment*).

This environment is mainly used for MIMO propagation results. Diffraction from furniture and other objects is not taken into account to cut down on the computational burden otherwise leading to long simulation times spanning over few days in case of massive MIMO systems (*cf.* Sec. 4.3) assuming $N = 64$ antennas at both TX and RX ends.

3.4 Frequency Dependence of Material Properties

In the lower microwave region (below 6 GHz) with a fairly long wavelength (e.g., the wavelength is 60 mm at 5 GHz), reflections from common building materials hardly consider surface roughness, and simply treat surfaces as smooth, flat and reflective. However, multiple works at mm-wave frequencies such as [40, 71, 72], investigated the impact of surface roughness (diffuse scattering) experimentally. The experiments in most of these works are setup for outdoor rough surfaces with standard deviation heights of few centimeters. The authors in [19] measured the statistical parameters of rough surfaces of indoor common building materials such as wallpaper and plaster using commercially available equipment [73]. *Please note that the lateral and vertical scan resolutions are the most important characterization parameters for surface roughness measurements but not the carrier frequencies.*

Table 3.1: Materials and their parameters used in ray-tracing (from [19, 31, 74]).

Material	$\tilde{\epsilon}_r$	$\tilde{\tilde{\epsilon}}_r$	ℓ_{cr}	σ_h
Plaster x (perf. smooth)	3.691	0.217	0.00 mm	0.00 mm
Plaster x1 (slightly rough)	3.691	0.217	1.30 mm	0.05 mm
Plaster x2 (slightly rough)	3.691	0.217	1.70 mm	0.15 mm
Plaster x3 (very rough)	3.691	0.217	1.80 mm	0.25 mm
Wood (perf. smooth)	1.734	0.073	0.00 mm	0.00 mm
PVC (perf. smooth)	2.788	0.069	0.00 mm	0.00 mm
Polycarbonate (perf. smooth)	2.750	0.011	0.00 mm	0.00 mm
Glass (perf. smooth)	6.656	0.539	0.00 mm	0.00 mm

The calculated relative standard deviations of the surface height are 130 μm and 50 μm for wallpaper and plaster x1, respectively. These standard deviations are comparatively small even at mm-wave frequencies, and thus are usually neglected. On the contrary, the THz frequencies have a wavelength on the order of several hundred micrometers (e.g., $\lambda_{300\text{GHz}} = 1 \text{ mm}$) which is comparable to the surface deviation heights. Hence, the impact of roughness is to be investigat-

ed quantitatively. Thereupon, the empirical parameters of the materials used in our modeling approach along with their standard deviation heights and correlation lengths are tabulated in Table 3.1.

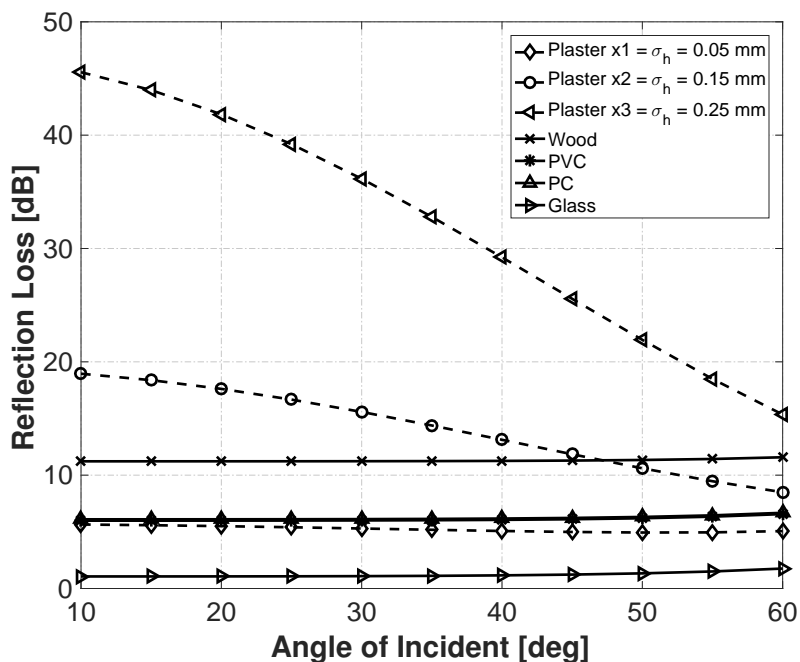


Figure 3.8: Reflection Losses from combined Fresnel at 300 GHz with different incident angles for materials listed in Table 3.1.

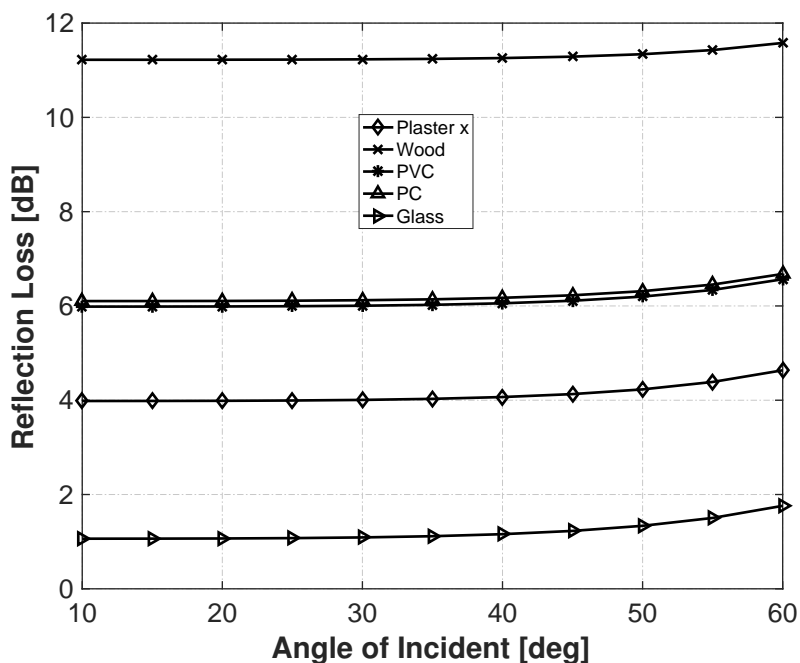


Figure 3.9: Reflection Losses from combined Fresnel at 300 GHz with different incident angles (smooth materials).

Fig. 3.8 shows the reflection loss for common building materials at 300 GHz for different incident angles corresponding to the experimentally calculated Fresnel reflection coefficient in [74]. It is evident that the roughness of a surface costs far more reflection loss than done by its electrical properties. Apparently, this higher reflection loss is also due to shorter wavelength at THz frequencies. In contrast, for larger wavelengths the reflection loss is comparatively less. Now, if rough plasters are assumed to be smooth (i.e., plaster x), the resulting reflection losses are illustrated in Fig. 3.9 which clearly depict the dominance of material electrical properties.

3.5 Novel Solution of the Scattering Problem in THz

Among the major challenges at THz frequencies is the modeling of the most significant propagation phenomenon of diffuse scattering, by which an incident ray may split into a specular and several non-specular rays after bouncing off from rough materials. Notice that the scattering problem of EM waves is still not completely solved and no exact closed-form solutions exist as of yet. However, numerous approximate methods have been developed for wave scattering at rough surfaces in order to predict and interpret experimental data. Amongst these, four popular surface scattering models are: (i) Rayleigh-Rice model; (ii) Effective Roughness model; (iii) classical Beckmann-Kirchhoff model; and (iv) modified Beckmann-Kirchhoff model. Pertaining to the roughness characteristic, ER model [75] depends only on standard deviation height σ_h which is irregular and arbitrary in distribution, whereas B-K model [30] considers not only the standard deviation height which takes Gaussian hypothesis on the height distributions into consideration, rather considers the irregularity or aperiodicity of surface roughness in spatial direction also. This second statistical parameter is called correlation length l_{cr} . In fact, by varying these two statistical parameters one can generate surfaces that match in appearance to almost any rough surface met in practise. The main characteristics of these aforementioned models are summarized in more detail in the preceding subsections. *In order to save the readers from confusion, the ER model (cf. Fig. 3.13) and B-K model (cf. Fig. 3.14) are explained separately based on two different scattering geometries.*

3.5.1 Rayleigh-Rice (R-R) Model

The R-R approach can be seen as the most rigorous analytical solution of Maxwell's equations for the limiting case of optically smooth surface (i.e., slightly rough surface). Rayleigh

expressed optical smoothness by following the accurate criterion from [76] as

$$(4\pi\sigma_h \cos \Theta_i / \lambda)^2 \ll 1 \quad (3.3)$$

Notice that Eq. (3.3) does not contain the scattering angle as an argument. The reason is straightforward, no assumptions are made regarding this angle when developing the theory. Thus, when employing the R-R model, the incoherent diffuse scattering is considered as multipath not directed towards RX and is therefore neglected. Besides, the optically smooth surface check can be a formidable figure depending on the composite surface or wavelength at hand. It is usually formulated as: $\sigma_h / \lambda \ll 1$. Unfortunately, there is no explicit number to decide whether the criterion is fulfilled or not. For example, in [76] and [77] it is stated that σ_h / λ should be smaller than 0.01 and 0.05, respectively. However, in case of THz frequencies, the optically smooth surface requirement is possibly reinstated owing to the extremely short wavelength. Therefore, in our simulation model, we hypothetically assume that slightly rough surfaces have $\sigma_h = 0.15$ mm and $\sigma_h = 0.30$ mm. We consider $\sigma_h = 0$ mm as a benchmark for conceptualizing ideally smooth surfaces as opposed to rough surfaces.

The R-R theory is developed on the basis of boundary conditions for a perfectly conducting surface. Besides, this theory takes polarization of the incident and scattered wave into account. A small parameter of this theory is the Rayleigh roughness parameter (ρ_{spec}). For a Gaussian height probability density function, this term is equal to (cf. Eq. 2.14). If the electric fields are summed up without phase information, the averaged received power is given by

$$P_{\text{RX}} = P_i \mathbb{1}_{\text{LoS}} + \sum_{k=1}^{N_p} P_k \quad (3.4)$$

Here, P_i is the direct path and $\mathbb{1}_{\text{LoS}}$ is the indicator function that is equal to 1 or 0 in case the direct path is present or not, respectively. N_p is the number of paths and P_k is the time averaged power of the k^{th} specular path. P_i affected by the free space loss only is given as

$$P_i = P_{\text{TX}} \left(\frac{\lambda}{4\pi d_i} \right)^2 \left| g_{T,\theta}(\theta_D, \phi_D) g_{R,\theta}(\theta_A, \phi_A) + g_{T,\phi}(\theta_D, \phi_D) g_{R,\phi}(\theta_A, \phi_A) \right|^2 e^{-\alpha_a(f_i) d_i} \quad (3.5)$$

where d_i stands for the path length between TX and RX, θ_D and ϕ_D give the direction in which the ray leaves from the TX. Likewise, θ_A and ϕ_A point to the direction from which the ray arrives at the RX, and $\alpha_a(f_i)$ is the atmospheric attenuation coefficient at frequency f_i for given path

length. The generic equation for direction of arrival is given by

$$g_{\theta}(\theta, \phi) = \sqrt{|G_{\theta}(\theta, \phi)|} e^{j\psi_{\theta}} \quad (3.6)$$

where G_{θ} is the theta component of the receiving antenna gain and ψ_{θ} is the relative phase of the θ component of the far-field electric field. Thereupon, the time averaged power P_k of the k^{th} specular path accounting for the reflection from rough surface in the THz range is

$$P_k = \frac{\tilde{\Gamma} \lambda^2}{8\pi Z_0} |E_{\theta,k} g_{\theta}(\theta_k, \phi_k) + E_{\phi,k} g_{\phi}(\theta_k, \phi_k)|^2 e^{-\alpha_a(f_i) d_k} \quad (3.7)$$

where $E_{\theta,k}$ and $E_{\phi,k}$ are the theta and phi components of the electric field of the k^{th} path at the RX, respectively. θ_k and ϕ_k give the direction of arrival. The modified Fresnel reflection coefficient (i.e., $\tilde{\Gamma} = \rho_{\text{spec}} \Gamma$) is previously explained (*cf.* Sec. 2.6.3) and the expressions for conventional reflection coefficient (Γ) for a smooth surface are given in Eq. (2.7) and Eq. (2.8).

At THz frequencies, diffuse reflection tends to be higher due to the increased surface roughness and this surface roughness causes an additional attenuation even in a specular direction of reflection (by the amount that is scattered into non-specular directions). The surface scattering process for diffuse reflection has been analyzed based on R-R theory (i.e., the specular losses occur due to the diffuse reflection). Simulations are conducted in order to study the indoor multipath propagation and its impact on the ultra-broadband THz channel by considering two different degrees of surface roughness (i.e., $\sigma_h = 0.15$ mm and $\sigma_h = 0.30$ mm), respectively. And as a benchmark compared with the ideally smooth wall (i.e., $\sigma_h = 0$ mm).

The simulation setup is depicted in Fig. 3.5 (first environment, *cf.* Sec. 3.3). All walls, the ceiling and floor are made of plasters ($\tilde{\epsilon}_r = 3.691$, $\tilde{\epsilon}_r = 0.217$) with focus to investigate and demonstrate the influence of degree of roughness on the ultra-broadband 300 GHz propagation characteristics. The multipaths between TX and RX are computed in terms of the frequency-domain CTF according to Kirchhoff Approximation (KA), which accounts for specular losses by introducing Rayleigh roughness factor calculated from the surface height distribution. The time-domain channel impulse response (CIR) or $h(t)$ is obtained via inverse fast Fourier transform (IFFT). Here it shall be noted that at each frequency point, the frequency dependent complex impulse response (CxIR) of the channel has been computed with the corresponding number

of multipaths, angle of arrival (AoA), angle of departure (AoD) and time of arrival (ToA) of individual paths. The complete CTF is then obtained through the coherent addition of the individual CxIR. We employ the tangent plane approximation to scattering properties of common building materials in our propagation models which take Gaussian hypothesis on the height distributions into consideration. For the sake of conciseness, we refer the reader to author's separate publication [66] for the detailed description of the scenario.

At THz frequencies, the multipath propagation characteristics are likely to vary significantly over the band of interest in case the environment is surrounded by rough surfaces. This is actually the case in our simulation model. Fig. 3.10 and Fig. 3.11 depict the LoS results with and without scattering. Upon dual analysis (*cf.* Figs. 3.10 and 3.11), in case of no scattering (or no roughness) the highest frequency selectivity of the channel is observed. In contrast, the impact of surface roughness on the THz propagation channel leads to hardening of the THz channel. However, the average attenuation over the whole bandwidth in Fig. 3.10 is found to be 96.59, 97.02 and 97.04 dB for $\sigma_h = 0$ mm, $\sigma_h = 0.15$ mm and $\sigma_h = 0.30$ mm, respectively.

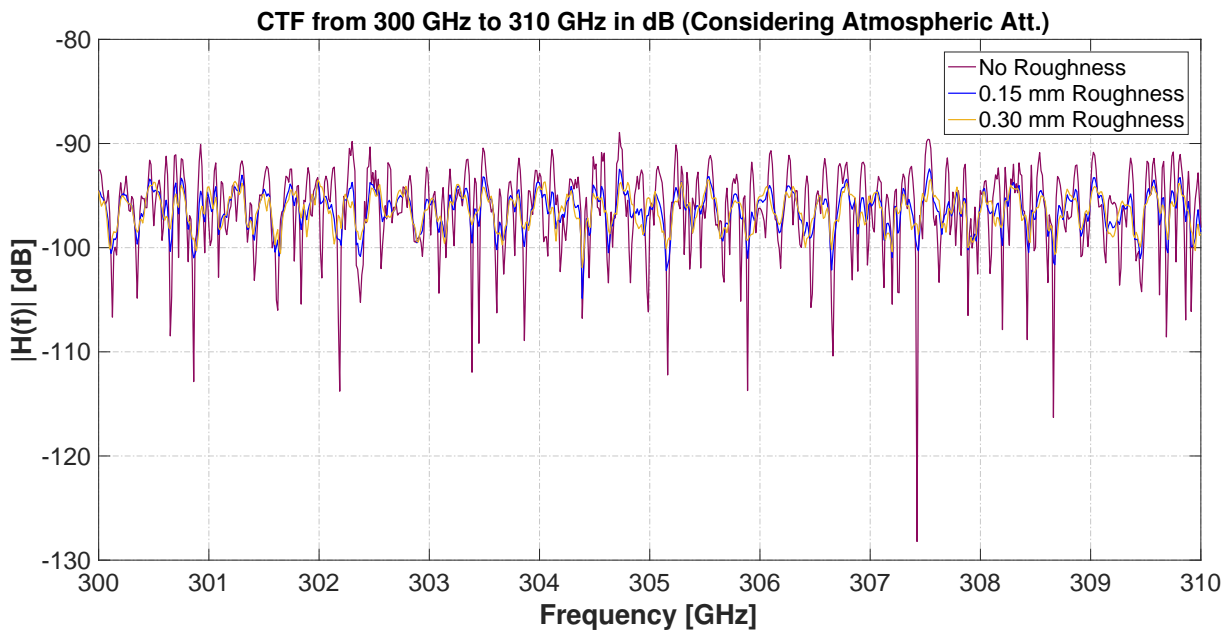


Figure 3.10: CTF of ray-tracing simulation of twice reflected TE polarized plane wave when considering smooth and rough surfaces.

Apparently, the relatively identical average attenuation observed for $\sigma_h = 0.15$ mm and $\sigma_h = 0.30$ mm is most probably due to the presence of a dominant LoS path (direct path) and the scattered channel paths may exert little or no impact on the total received power. In other words, varying σ_h does not affect the relative scattered power in LoS case. Furthermore, if the

surface roughness is not properly taken into account in the propagation modeling, the received power levels for the worst scenario (i.e., frequency point $f = 307.4$ GHz) are miscalculated up to 28.3 dB and 30.5 dB for $\sigma_h = 0.15$ mm and $\sigma_h = 0.30$ mm, respectively. This approves the necessity to include scattering in THz propagation modeling.

Next, Fig. 3.11 presents quite interesting results. Varying the σ_h from $\sigma_h = 0.15$ mm and $\sigma_h = 0.30$ mm, it is evident that the longer paths are crossing the threshold limit because their amplitudes are impacted. Thus, the surface roughness on one hand increases the scattering richness but on the other hand decreases the channel strength.

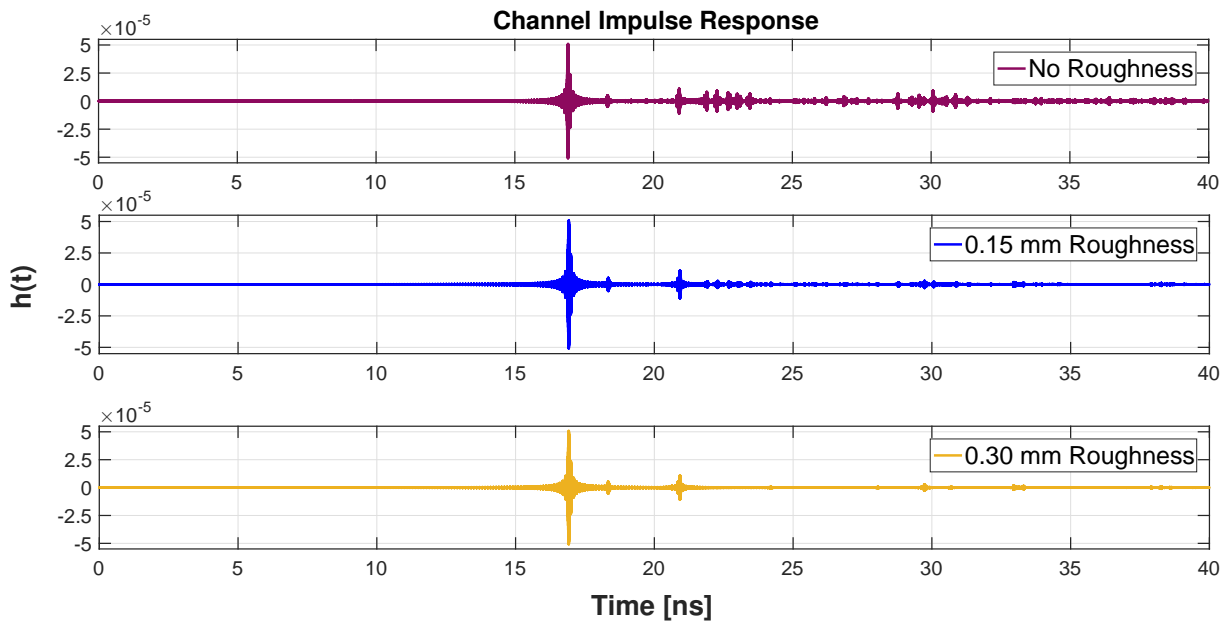


Figure 3.11: CIR of ray-tracing simulation of twice reflected TE polarized plane wave when considering smooth and rough surfaces.

3.5.2 Effective Roughness (ER) Model

ER is a semi-empirical model described by Degli-Esposti and employs two approaches to define the scattering coefficient [75]. The fundamental difference between the two approaches is basically in defining the scattering parameter S .

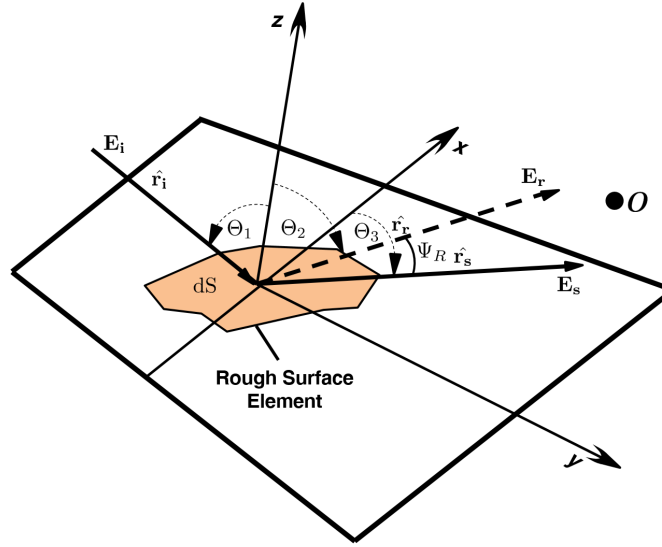


Figure 3.12: The scattering geometry of rough surface dS explaining ER model.

In our study and then later for implementation in our RTA tool, we choose ER model's approach which defines scattering coefficient S as a ratio of scattered energy with specular direction given by

$$S = \frac{|\overline{E}_s|}{|\overline{E}_r|} \Big|_{dS} \quad (3.8)$$

where \overline{E}_r and \overline{E}_s are the norms of the reflected and scattered fields on the surface element dS (*cf.* Fig. 3.12), respectively. As dS is infinitesimal and therefore, the fields on it are assumed constant. The intensity of the scattered field \overline{E}_s is evaluated based on a proper scattering coefficient along with a scattering pattern, both depending on the characteristics of common building materials' irregularities. Hereupon, S^2 is the amount of the power which is scattered in all directions at the expense of the reflected power only. Therefore, the power balance can be written as

$$\begin{aligned} \frac{|\overline{E}_i|^2}{2\eta} ds \cos \Theta_1 &= R^2 \frac{|\overline{E}_r|^2}{2\eta} ds \cos \Theta_1 \\ &+ S^2 \frac{|\overline{E}_r|^2}{2\eta} ds \cos \Theta_1 + P_P \\ &= R^2 \Gamma^2 \frac{|\overline{E}_i|^2}{2\eta} ds \cos \Theta_1 \\ &= S^2 \Gamma^2 \frac{|\overline{E}_i|^2}{2\eta} ds \cos \Theta_1 + P_P \end{aligned}$$

Here R is the reflection loss factor, P_P is the power which penetrates the wall, and $\Gamma = |\overline{E}_r|/|\overline{E}_i|$.

The factor R accounts for the specular power loss and is a well-known parameter of scattering theory [78]. Note that Γ and \bar{E}_r can be determined using the Fresnel reflection coefficients. According to this approach, the overall power balance on the surface element dS can be written as

$$1 = \Gamma^2(R^2 + S^2) + P_P/P_i \quad (3.9)$$

where P_i is the incident power density. In case of an ideally smooth wall (i.e., $S=0$, $R=1$), the power balance becomes

$$1 = \Gamma^2 + P_P/P_i \quad (3.10)$$

In principle by combining Eq. (3.9) and Eq. (3.10), we can eliminate the P_P/P_i and a relation between S and R can be obtained as

$$R \cong \sqrt{1 - S^2} \quad (3.11)$$

Note that, adopting this approach where S and R are both independent from the incident direction and thereby S can assume any value in the range $[0,1]$.

Meanwhile, ER introduces two scattering radiation pattern models: *Lambertian Model* and *Directive Model*. The main characteristics of these models are briefly discussed below.

Lambertian Model

This model has maximum power in the direction perpendicular to surface reflection without considering the direction of incidence wave. From [75, 79], we can calculate the amplitude of scattered rays as

$$dE_2^2 = K_o^2 S^2 \Gamma^2 \frac{dS \cos(\Theta_1) \cos(\Theta_2)}{\pi} \frac{1}{r_1^2 r_2^2} \quad (3.12)$$

where $K_o = \sqrt{60 G^{TX} P_{TX}}$, and G^{TX} and P_{TX} denote gain and input power of the transmitting antenna, respectively.

Fig. 3.13 depicts various radiation lobes (normalized scattering patterns) for Lambertian (for an incidence angle 45°) and Directive Models.

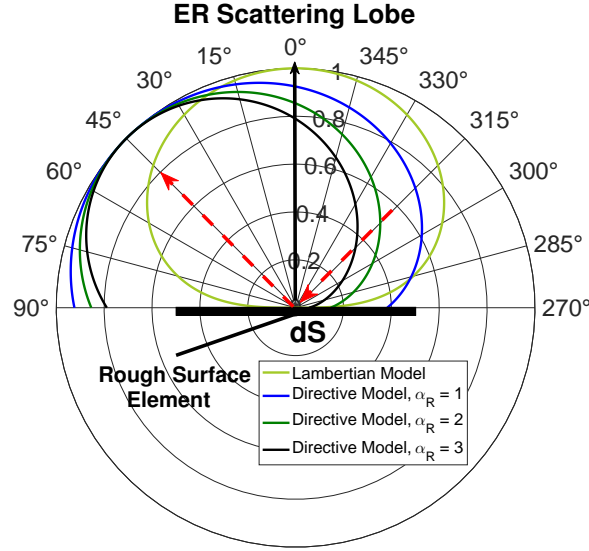


Figure 3.13: Lambertian and Directive single-lobe diffuse scattering patterns at 300 GHz from rough surface dS .

Directive Model

Similar to B-K model (explained later in this Sec.), the maximum scattering lobe is steered to the direction of specular reflection. The respective expression is rewritten as

$$dE_2^2 = E_{s0}^2 \left(\frac{1 + \cos(\Psi_R)}{2} \right)^{\alpha_r} \quad \alpha_r = 1, 2, \dots, N \quad (3.13)$$

Here, α_r is the parameter that sets width of the scattering lobe. The higher the α_r , the narrower the lobe. The expression for maximum amplitude E_{s0} is

$$E_{s0}^2 = \left(\frac{SK}{r_1 r_2} \right)^2 \Gamma^2 \frac{dS \cos(\Theta_1)}{F_{\alpha_r}} \quad (3.14)$$

where

$$F_{\alpha_r} = \frac{1}{2^{\alpha_r}} \sum_{j=0}^{\alpha_r} \binom{\alpha_r}{j} I_j \quad (3.15)$$

and I_j is then defined as

$$I_j = \begin{cases} \frac{2\pi}{j+1} & \text{if } j \bmod 2 = 0 \\ \frac{2\pi}{j+1} f(\Theta_1) & \text{if } j \bmod 2 \neq 0 \end{cases} \quad (3.16)$$

where

$$f(\Theta_1) = \cos(\Theta_1) \sum_{\omega=0}^{\frac{j-1}{2}} \binom{j-1}{\omega} \frac{\sin^{2\omega}(\Theta_1)}{2^{2\omega}} \quad (3.17)$$

3.5.3 Classical Beckmann-Kirchhoff (cB-K) Model

The cB-K model is derived from the analytical model. Its theory is more realistic and provides more insight of the physical processes involved in the surface scattering. More realistic in contrast to R-R, since cB-K accounts for the diffuse reflection impact from rough surfaces in both specular and non-specular directions. The cB-K model is validated against ultra-broadband measurements [80] and it is applicable to both dielectric and metallic surfaces. However, the cB-K theory is a scalar treatment; i.e., the wave scattering theory accounts only for the distribution of energy, and does not account for more complex effects such as *polarization*. The B-K theory is derived from the Helmholtz integral [67] and it predicts a symmetrical scattered field distribution around the specular direction under some assumptions for *slightly* and *very rough surfaces* [30]. The details of the theory along with its derivation are described comprehensively in the monograph by Beckmann and Spizzichino [30] and the key steps involved in the derivation of the model are only mentioned. But let us summarize the assumptions under which cB-K model is derived. Perhaps being forthright and honest, these assumptions ensure the validity of B-K model and it is not fair to withdraw any of the below listed assumptions at the cost of mathematical simplicity.

Assumptions

1. The surface is perfectly conducting.
2. The radius of curvature of surface irregularities is large compared with the wavelength of the incident field.
3. Shadowing and multiple scattering (*cf.* Fig. 3.2 b) is neglected.
4. The reflection coefficient of the surface has unity magnitude.
5. The incident wave is plane and linearly polarized with the electric field vector in the plane of incidence or perpendicular to it.
6. The observation point (i.e., \mathbf{P}) is sufficiently far from surface for the scattered waves to be exactly planar.
7. The rough surface has a Gaussian probability density of height and a Gaussian correlation function.

The field scattered by a surface in any direction can be determined from the field present at the surface. Let us assume the incident field E_i , a harmonic plane wave of unit amplitude, is incident at the rough surface element dS . The elevation angle of incidence is represented as Θ_i and the elevation and azimuth reflected angles in the scattered region as Θ_r and Θ_s , respectively. The angles are measured with respect to the z axis as shown in Fig. 3.14. The total scattered field \mathbf{E}_s at a point P far above the rough surface is given by

$$E_s(\mathbf{P}) = \frac{1}{4\pi} \int \int_S \left(E_i \frac{\partial \psi}{\partial n} - \psi \frac{\partial E_i}{\partial n} \right) dS \quad (3.18)$$

This is called the *Helmholtz Integral*. It's complete derivation is provided in [30]. Here, S is the reflection surface, \mathbf{n} is the normal to the rough surface element at the considered point, and ψ is a continuous scalar function given by

$$\psi = \frac{e^{jk r'}}{r'} \quad (3.19)$$

where, $j = \sqrt{-1}$ and $k = 2\pi/\lambda$ is the propagation constant of the reflected wave. \mathbf{E}_i and $\partial \mathbf{E}_i / \partial \mathbf{n}$ are the field and it's normal derivative on dS . The exact values of these two quantities in general are unknown. The KA or *Tangent Plane Approximation* may be used in approximating the values of the field and it's normal derivative at each point on the surface and then evaluating the integral in (Eq. 3.18). This approximation breaks down if the roughness includes sharp edges or sharp points compared to the wavelength of the incident wave. Thus, the field at a point on the rough surface is equal to the field that would be present on a tangent plane at that point.

Moreover, to calculate the local scattered fields E_s , the KA treats the facets (rough surface elements) of a rough surface as tangent planes and applies the Fresnel reflection coefficient Γ . Within this approximation the field on the surface S based on [30, p. 20] is defined as

$$E_s = (1 + \Gamma)E_i \quad (3.20)$$

In general, the characteristics of the reflection can be described by the well-known Fresnel reflection coefficient only in case of an ideal smooth surface. Although, we have considered a rough surface, the KA is still applicable due to it's assumption of a rough surface that is however locally smooth.

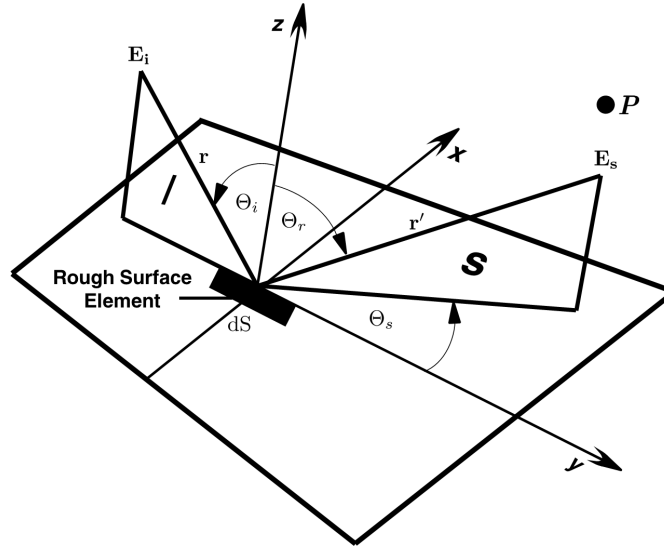


Figure 3.14: Geometry of scattered angles from a rough surface element dS , I is the incident plane and S is the scattering plane explaining B-K model.

In case of very rough surfaces, the reflection behaviour of the wave is dominated by the scattering phenomena. We introduce a scattering coefficient from [30, p. 22]

$$\rho = \frac{E_s}{E_r} \quad (3.21)$$

Here, E_r is the field specularly reflected ($\Theta_i = \Theta_r$) by a smooth and perfect conducting surface of similar dimensions as the rough one, and under the same angle of incidence at the same distance by considering vertical polarization. From [30, Appendix A], we have

$$E_r = \frac{jkA \cos(\Theta_i) e^{jkr_0}}{\pi r_0} \quad (3.22)$$

Area $A = l_x l_y$ is the rectangular surface area. The Kirchhoff solution requires the lateral dimension l_x and l_y of the area A to be much greater than the wavelength, i.e., $l_x \gg \lambda$ and $l_y \gg \lambda$.

It is worth remarking that to attain ρ , in general an integration of the scattered field over the whole surface needs to be performed. However, usually rough surfaces found in indoor environments with common building materials (i.e., wallpaper and plaster) have randomly rough Gaussian height distributions at THz frequencies [19].

From a complex quantity ρ in Eq. (3.21), we determine the mean value of $|\rho|^2$

$$\langle \rho \rho^* \rangle = \langle |\rho|^2 \rangle = \left\langle \left| \frac{E_s^2}{E_r^2} \right| \right\rangle \quad (3.23)$$

Here, the operator $\langle \cdot \rangle$ is an ensemble mean which represents a statistical average, and $(\cdot)^*$ denotes the complex conjugate.

Now, assume a rectangular surface of area $A = l_x l_y$ with infinite conductivity. In general, the average scattering coefficient of an incident wave on a rough surface of angle Θ_i , scattered at angles Θ_r and Θ_s , respectively, is determined by the following expressions [30, p. 88]

$$\langle \rho \rho^* \rangle_\infty = \left(\rho_0^2 + \frac{\pi \ell_{cr}^2 F^2}{A} \sum_{m=1}^{\infty} \frac{g^m}{m! m} e^{-\frac{v_{xy}^2 \ell_{cr}^2}{4m}} \right) e^{-g} \quad (3.24)$$

Here, ρ_0 the scattering coefficient of a plane surface with area $A = l_x l_y$ is given by

$$\rho_0 = \text{sinc}(v_x l_x) \text{sinc}(v_y l_y) \quad (3.25)$$

From trigonometry it follows,

$$v_x = k(\sin(\Theta_i) - \sin(\Theta_r) \cos(\Theta_s)) \quad (3.26)$$

$$v_y = k(-\sin(\Theta_r) \sin(\Theta_s)) \quad (3.27)$$

$$v_{xy} = \sqrt{v_x^2 + v_y^2} \quad (3.28)$$

The geometrical factor, a function of incident and scattered angles is given as

$$F = \frac{1 + \cos(\Theta_i) \cos(\Theta_r) - \sin(\Theta_i) \sin(\Theta_r) \cos(\Theta_s)}{\cos(\Theta_i) (\cos(\Theta_i) + \cos(\Theta_r))} \quad (3.29)$$

The quantity g , a measure of phase variation introduced by surface roughness σ_h is expressed as

$$g = (v_z \sigma_h)^2 = \sigma_h^2 (2\pi f/c)^2 (\cos(\Theta_i) + \cos(\Theta_r))^2$$

From expression in Eq. (3.24), it is apparent that the average scattering coefficient consists of two terms. The first term $\rho_0^2 e^{-g}$ describes the influence of the scattering in the direction of specular reflection (i.e., specular spike component) only, and the succeeding (second) term corresponds to the diffusely scattered field (i.e., side lobes components). The average scattering coefficient with different surface height distributions is schematically depicted in Fig. 3.15. Further, in Fig. 3.16 it is apparent that the incident power is reflected and scattered in and around the specular direction with an attenuation of 20.93 and 37.03 dB, respectively.

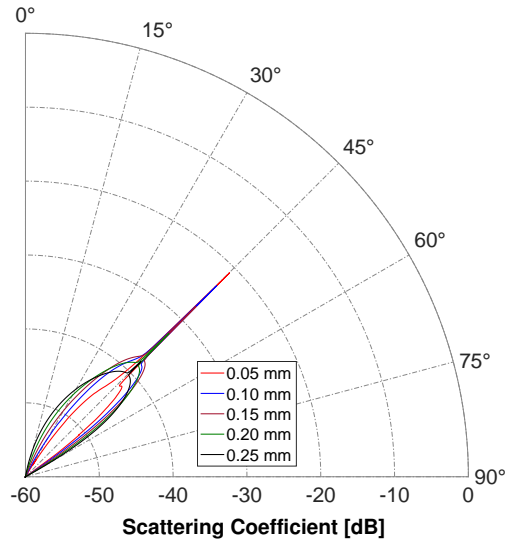


Figure 3.15: Simulated scattering coefficient at 300 GHz of the plaster x_i , ($r' = 5$ m).

Owing to Eq. (3.24), B-K model uses two statistical parameters to characterize rough surfaces: (i) the standard deviation height σ_h ; (ii) the correlation length ℓ_{cr} . In general, the height values of the topographic surface features on the mean surface level are measured at equally spaced digitized data points. On the other hand, the correlation length ℓ_{cr} is defined as the lag-length at which the Gaussian correlation function drops to $1/e$ of it's maximum [67].

The exponential series given by the summation in the lobe component can be approximated for slightly rough ($0 < g \ll 1$) and very rough surfaces ($g \gg 1$). The approximation results in simpler expressions of the scattering coefficient for these two extreme surface conditions are

$$\langle \rho \rho^* \rangle_{\text{slightly rough}} = \left(\rho_0^2 + \frac{\pi \ell_{cr}^2 F^2 g}{A} e^{-\frac{v_{xy}^2 \ell_{cr}^2}{4}} \right) e^{-g} \quad (3.30)$$

$$\langle \rho \rho^* \rangle_{\text{very rough}} = \frac{\pi \ell_{cr}^2 F^2}{A v_z^2 \sigma_h^2} e^{-\frac{v_{xy}^2 \ell_{cr}^2}{4 v_z^2 \sigma_h^2}} \quad (3.31)$$

Importantly, the above approximation in Eq. (3.24) assumed the surface to be a perfect conductor. Indeed, the materials used in our study are not perfect conductors. Next, in order to approximate the average scattering coefficient for finite conductors, we average the conventional Fresnel reflection coefficient (Γ) over the entire surface area and use the resultant value ($\langle \Gamma \rangle$) as a constant in the Helmholtz integral [67]. Finally, for finite conducting surfaces, the average

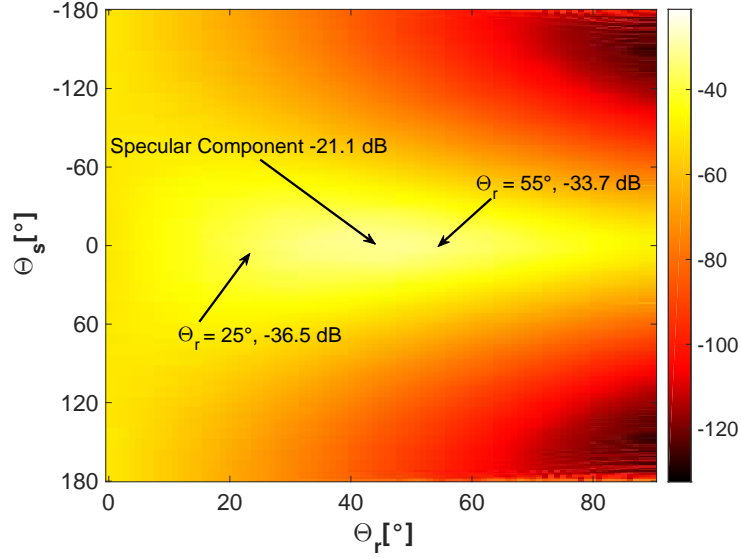


Figure 3.16: Angular dependent power reflection factor of scattering coefficient (B-K model) at 300 GHz of the plaster sample x1, ($r' = 5$ m).

scattering coefficient becomes

$$\langle \rho \rho^* \rangle_{\text{finite}} = \langle \Gamma \Gamma^* \rangle \langle \rho \rho^* \rangle_{\infty} \quad (3.32)$$

Therefore, the mean scattered power is given by

$$\langle P_s \rangle = \frac{|E_s^2|}{2Z_0} = \frac{|E_r^2|}{2Z_0} \langle \rho \rho^* \rangle_{\text{finite}} \quad (3.33)$$

Likewise, the incident power is

$$\langle P_i \rangle = \frac{|E_i^2|}{2Z_0} \quad (3.34)$$

Thus, the average power reflection coefficient of a surface area A , specifying the scattered field in a distance r' from surface to the observation point P relative to the incident power P_i leads to [30, p. 89] and let $|E_i^2| = 1$

$$\langle R_{\text{power}} \rangle_{\text{scattered}} = \frac{\langle P_s \rangle}{\langle P_i \rangle} = \langle |E_r^2| \rangle \langle \rho \rho^* \rangle_{\text{finite}} \quad (3.35)$$

The significance of this result can be seen once we substitute the value of E_r from Eq. (3.22), we find

$$\langle R_{power} \rangle_{scattered} = \frac{4A^2 \cos^2(\Theta_i)}{\lambda^2 r'^2} \langle \rho \rho^* \rangle_{finite} \quad (3.36)$$

Similarly, for the direction of specular reflection $\Theta_r = \Theta_i$, $\Theta_s = 0$, we have

$$\langle R_{power} \rangle_{specular} = \langle \rho \rho^* \rangle_{finite} = \langle \Gamma \Gamma^* \rangle \langle \rho \rho^* \rangle_{\infty} \quad (3.37)$$

since $\rho_0 = 1$ for $v_{xy} = 0$, Eq. (3.24) is rewritten as [30, p. 93]

$$\langle \rho \rho^* \rangle_{\infty} = e^{-g} \quad (3.38)$$

Substituting Eq. (3.38) in Eq. (3.37), we obtain

$$\langle R_{power} \rangle_{specular} = \langle \rho \rho^* \rangle_{finite} = \langle \Gamma \Gamma^* \rangle e^{-g} \quad (3.39)$$

3.5.4 Modified Beckmann-Kirchhoff (mB-K) Model

A modified B-K theory is attained by replacing the geometrical factor (F-factor squared) used by Beckmann in Eq. (3.24) with the $\cos(\Theta_i)$ in Lambert's cosine law. We can rewrite this for slightly and very rough surfaces as

$$\langle \rho \rho^* \rangle_{slightlyrough} = \left(\rho_0^2 + \frac{\pi \ell_{cr}^2 K g}{A} e^{-\frac{v_{xy}^2 \ell_{cr}^2}{4}} \right) e^{-g} \quad (3.40)$$

$$\langle \rho \rho^* \rangle_{veryrough} = \frac{\pi \ell_{cr}^2 K}{A v_z^2 \sigma_h^2} e^{-\frac{v_{xy}^2 \ell_{cr}^2}{4 v_z^2 \sigma_h^2}} \quad (3.41)$$

The renormalization constant K in this reformulation of scalar diffraction theory is given by the following expression

$$K = \frac{\int_{\alpha=-\infty}^{\infty} \int_{\beta=-\infty}^{\infty} L(\alpha, \beta - \beta_0) d\alpha d\beta}{\int_{\alpha=-1}^1 \int_{\beta=-(1-\alpha^2)^{\frac{1}{2}}}^{(1-\alpha^2)^{\frac{1}{2}}} L(\alpha, \beta - \beta_0) d\alpha d\beta} \quad (3.42)$$

The details about the variables used in Eq. (3.42) are given in [81]. This model can be worthy of use for the solution of scattering problems in volume scattering whilst it accommodates larger scattering angles.

3.6 Concluding Remarks

In depth studies on the general typology of the solid surfaces are elaborated in this chapter:

⇒ The four widely accepted scattering models, R-R, ER, cB-K, and mBK are chosen for resolving the scattering problems at THz frequencies.

⇒ A general classification of solid surfaces is presented and thorough studies of the material properties reveal that the roughness of a surface accounts far more reflection loss than done by its electrical properties. However, if these rough materials are assumed to be smooth then these reflection losses clearly depict the dominance of the electrical properties. Thus, concluding that the property of surface roughness plays a vital role in the diffuse scattering phenomenon.

⇒ The surface scattering characteristics are considered as cardinal in modeling the indoor multipath THz channels. Hence, the scattered field behaviour is elaborated with reference to the extremes, namely surface scattering and volume scattering. The multiple scattering experienced in case of highly scattering environments can be disregarded at THz frequencies due to the extreme reflection losses. The scattering coefficient results from B-K model back up this finding.

Novel THz Ray-Tracing Algorithms

The THz Regime, sometimes referred to as the "forbidden region" due to technological limitations along with the enormous potential of THz communication technology particularly for short-range wireless communication extends the research of channel propagation modeling. The existing models and tools in the lower frequency bands (i.e., 2.4 GHz, 5 GHz, Ultra-Wideband, 60 GHz) do not consider the roughness of a material profoundly because materials smooth for GHz frequencies become rough now for THz frequencies. In consequence, it calls for such simulation tools or RTAs that can be employed for channel modeling at THz frequencies. There are rigorous numerical simulation techniques close to Maxwell's equation to solve the scattering problem of random rough surfaces such as the method of moments (MoM) [82], finite-difference time-domain (FDTD) [83] and time-domain integral equation [84]. A major drawback of these techniques is that they require intensive computations along with a detailed description and information of the simulation scenario. Such limitations and restrictions tend to affect the accuracy of the results. Meanwhile, such techniques are ruled out for very short wavelengths ≤ 5 mm [85]. Thus, ray-tracing is a simple and reliable technique based on Geometrical Optics (GO) used to produce accurate deterministic description of the wave propagation. For many years, ray-tracing has been at the forefront in channel modeling of mm-wave indoor communications for multi-gigabit wireless transmission, whilst most of the ray-tracing tools currently provide modeling up to GHz frequencies only. The conventional GHz ray-tracer (RT) has some limitations when considering channel modeling in the THz region because the distinct THz propagation mechanisms do not obey the GO rules. Hence, this warrants a high demand for developing an RTA which can also consider these distinct THz propagation mechanisms such as specular reflection losses, diffuse scattering, depolarization, atmospheric attenuation and high

reflection losses of indoor common building materials. In order to approach this challenge, we developed our own novel THz 3D RTA tool based on GUI integrating the most famous THz scattering models of rough surfaces (mentioned in Chapter 3). This self-programmed 3D RTA tool using MATLAB can work completely standalone. Moreover, the RTA can be integrated into any commercial RT tools. The novel THz RTA is validated by comparing the path loss results against measurements in [17] at THz frequencies for modeling both LoS and NLoS scenarios and employing B-K model for correctness and comparison. Furthermore, this RTA tool does not currently consider any near zone fields. The RTA can be applied to different indoor scenarios such as offices, residential structures, conference rooms, corridors and libraries. *This one of a kind exclusive RTA is merely owned by three groups in the world.*

This chapter begins with an overview of GUI of the main window unveiling its distinct features in the calculation engine in Section 4.1. Then, Section 4.2 takes the discussion further with the major outputs of propagation predictions in terms of quantities such as received and scattered power, AoA, AoD, ToA, CxIR, CTF, and PDP. Finally, Section 4.3 continues with the self-programmed RTA tool to investigate the indoor multipath propagation and its impact on massive MIMO channels considering smooth and rough surfaces by employing the B-K model. Channel capacities of indoor THz massive MIMO channels with different surface roughness for both LoS and NLoS scenarios are calculated. This chapter embodies research published in [16, 86, 87].

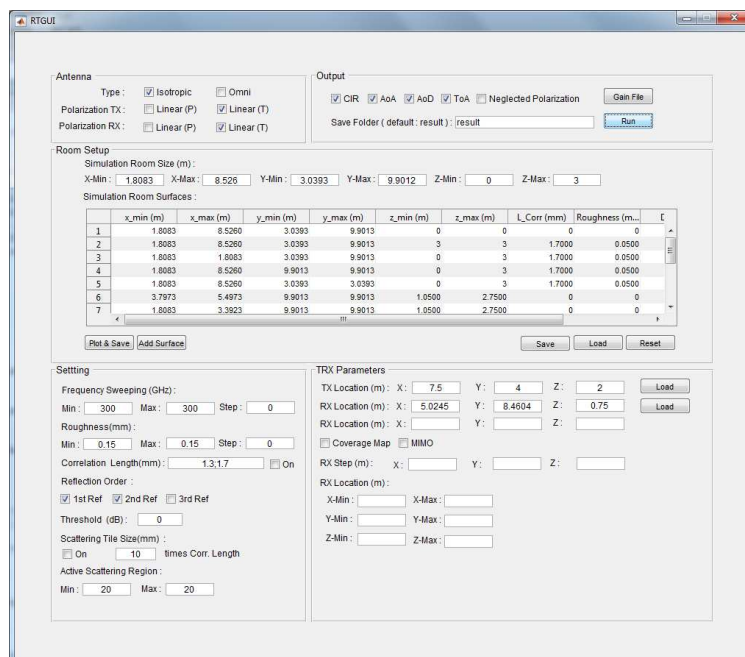


Figure 4.1: GUI of our RTA tool.

4.1 Ray-Tracing Algorithm (RTA) GUI

Fig. 4.1 shows the main window of the GUI. The GUI system for our RTA tool is a user friendly interface, thus can be operated without any prior MATLAB experience to simulate THz scenarios. This THz RTA delivers results in a number of ways. For instance, it provides visual presentations of some results such as *coverage maps*, *power distributions*, *angular distributions*, *PDPs*, and *CIRs* within the modeled environment. All output files produced by the RTA are in a readable ASCII format. The RTA is also capable of importing user defined antenna patterns from full-wave electromagnetic simulators such as CST Microwave Studio. The antenna can also be chosen from the main window using check box feature under “Antenna” tab. The user has the choice to select from two predefined *isotropic* and *omnidirectional* antennas. Whereas the location and position of the antenna can be set in a “.txt” file. To include the polarization impact on the channel model, polarization characteristics of both antennas and the propagation channel can be selected. Note that the geometrical depolarization is treated utilizing the Jones calculus [88].

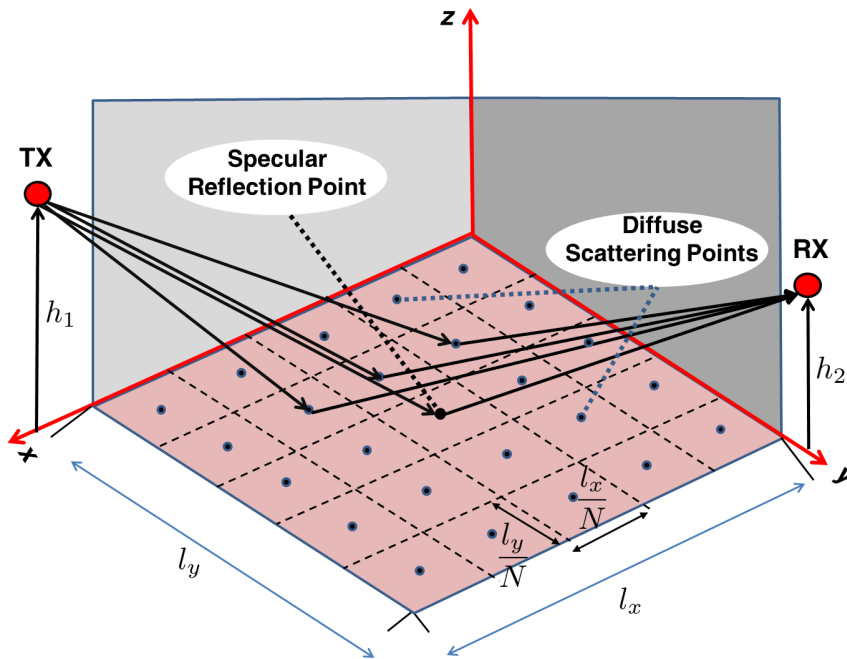


Figure 4.2: Square tiling of the rough surface (i.e., rough plaster walls and ceiling).

The user can also input the roughness parameters such as σ_h , ℓ_{cr} , along with the ϵ_r to simulate and study the influence of rough materials on the ultra-broadband THz propagation

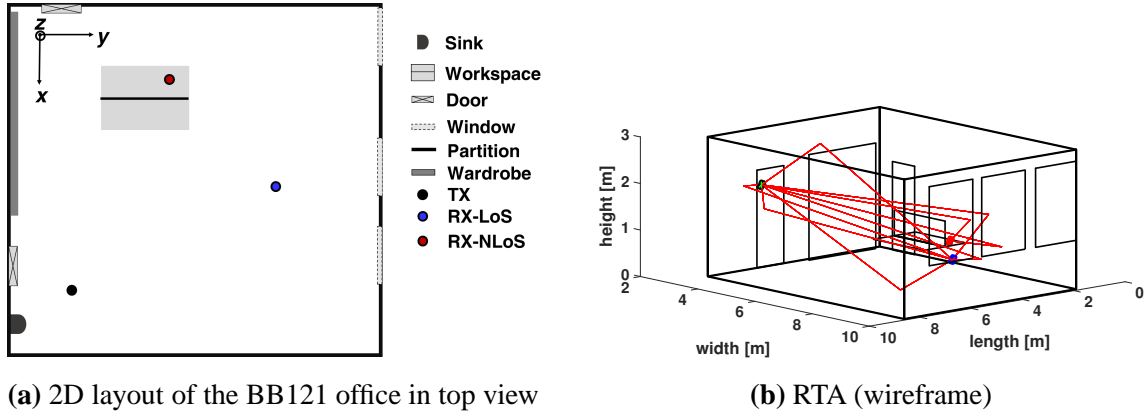


Figure 4.3: Real environment of the office room BB121.

characteristics. A rough surface area gives rise to many diffuse scattered paths (i.e., side lobe components) around the specular reflection point (i.e., specular spike). Therefore, the so called *active scattering region* have to be identified carefully in the form of $N \times N$ tiles around each specular point in order to collect all the energies of dominant side lobes. Hence, instead of considering the entire surface area as a single tile, we divide the surface into smaller square tiles as shown in Fig. 4.2. The smaller tiles allow for a higher simulation precision by computing comparatively much highly attenuated rays (e.g., 10 times ℓ_{cr} compute up to -230 dB for $N_x, N_y = 20 \times 20$). As in B-K model, the tile size side length has to be selected based on the ℓ_{cr} . The correlation term already mentioned in the Eq. (3.24) also points towards this selection. Meanwhile, in our modeling approach, we consider multipath components with minimum path amplitude up to -200 dB.

4.2 SISO Propagation and Channel Modeling

The simulation model defined for SISO systems is depicted in Fig. 4.3.

4.2.1 Received and Scattered Power

Simulations are conducted to evaluate the total received and scattered power of a rough plaster (in walls and ceiling) with different degrees of surface roughness in a real office environment. The total received power is composed of the specular reflection power and diffused scattered power. As the frequency increases, the surface changes from smooth to very rough and therefore, more power is diffusely scattered. Consequently, the ratio of specular power to the total power starts damping from maximum to minimum, lower enough to be neglected. The total received

power P_{tot} can be summarized with the following expression

$$P_{tot}(RX) = \langle R_{power} \rangle_{specular} + \langle R_{power} \rangle_{scattered} \quad (4.1)$$

As already proved in the author's work [16], the ER model with its two approaches can also be employed for channel modeling at THz frequencies. In [17], B-K model is already validated at THz frequencies, wherein measured and simulated channel impulse responses show very good agreement. Now, the comparison of ER and B-K models based on total received and scattered power is performed. In this simulation setup (*cf.* Fig. 4.3), there are five rough surfaces in total. The four walls, and one ceiling is modeled rough in this study. These five rough surfaces are divided into smaller square tiles with side lengths equal to 10 times the surface correlation length ℓ_{cr} . Besides, 20 x 20 tiles around each specular point applying to both scattering models are considered. The authors in [80] have already well-reasoned this quantity to be sufficient to get accurate results. The floor is covered with smooth polyvinyl chloride. Due to the smooth flooring, only specular reflections are included from the floor. Up to twice-reflected paths have been considered in the modeling process. In order to compare both the models, the simulation results are illustrated for both LoS and NLoS scenario in Fig. 4.4 and Fig. 4.5. For this study, particular attention is diverted to the NLoS scenario due to its imminence in terms of coverage and performance.

The results depict the same fundamental concept that the total received power depends on random rough surfaces in the simulation environment and decreases with increasing the degree of surface roughness especially for NLoS scenario. Please note that in NLoS scenario, most of the total received power contribution comes from diffuse scattering. For LoS scenario, however, the contribution of diffuse scattering is not poignant and the total received power depends highly on direct path power. Interestingly, the obtained results also point out that Directive model for $\alpha_r = 1$ is more closer to B-K model than any other scattering pattern (i.e., Lambertian model and Directive model with different alpha values). It should be noted that in LoS scenario, the results obtained for Lambertian model demonstrate an error on scattered power which is significant relative to total received power as depicted in Fig. 4.4. Next, in order to numerically verify the deviation error of total received power between ER-Lambertian, ER-Directive, and B-K models, the root mean square error (RMSE) method with reference to B-K model is employed and tabulated in Table 4.1.

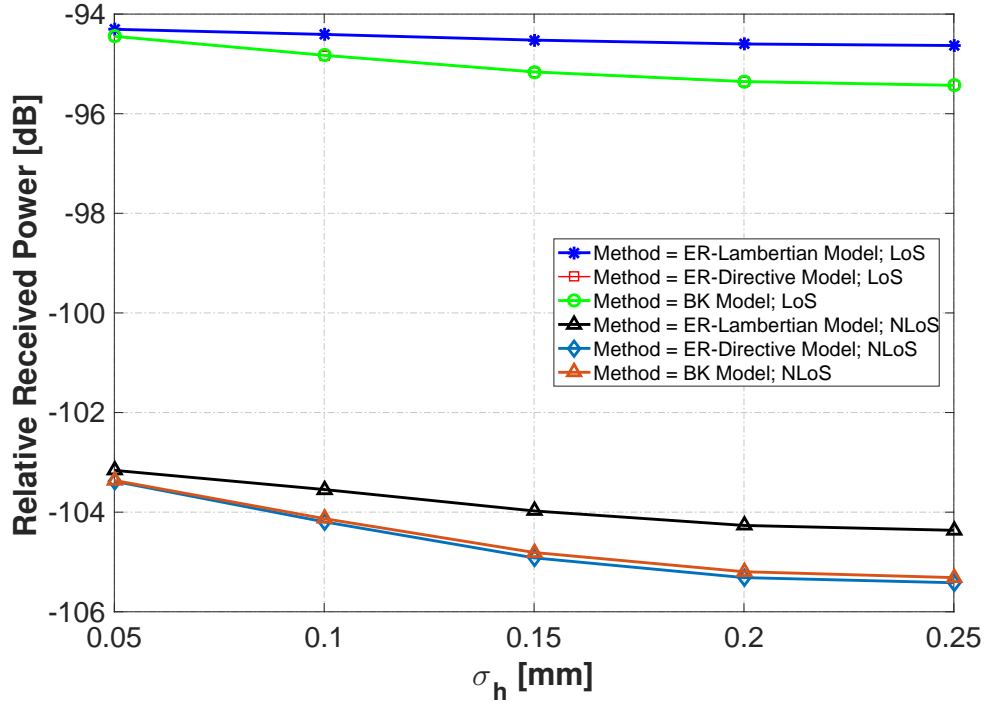


Figure 4.4: Total received power relative to input power for ER-Lambertian, ER-Directive and B-K model at 300 GHz for different roughness parameters for RX-LoS and RX-NLoS receiver locations. The surface correlation length of rough materials is $\ell_{cr} = 1.7$ mm with $l_x = l_y = 10 \ell_{cr}$.

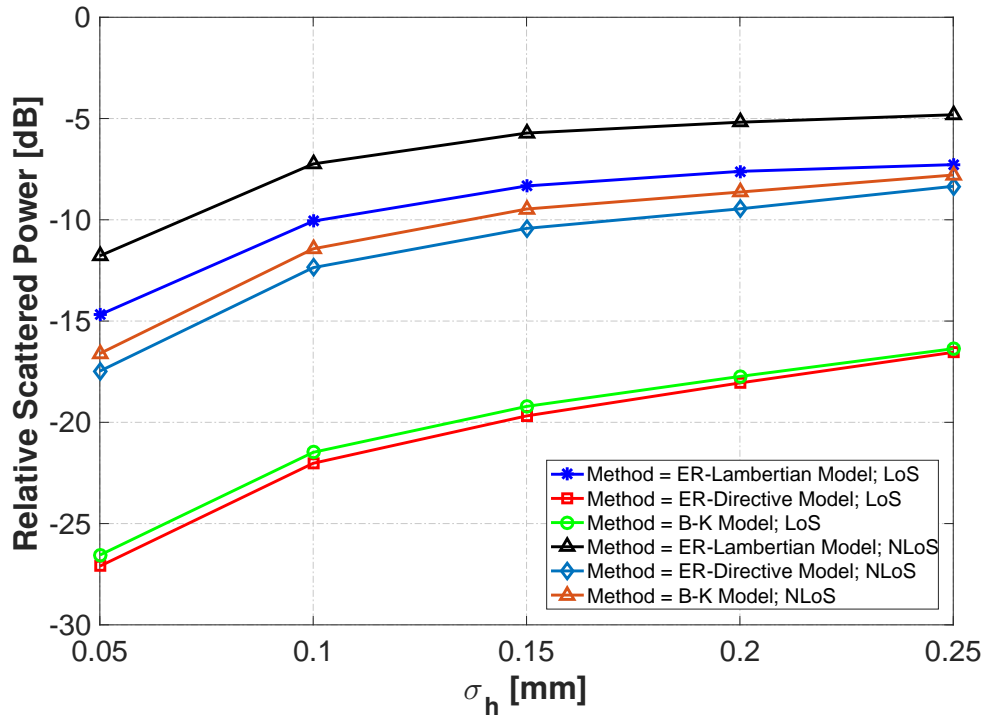


Figure 4.5: Scattered power relative to total received power for ER-Lambertian, ER-Directive and B-K model at 300 GHz for different roughness parameters for RX-LoS and RX-NLoS receiver locations. The surface correlation length of rough materials is $\ell_{cr} = 1.7$ mm with $l_x = l_y = 10 \ell_{cr}$.

Table 4.1: Deviation error of scattering models.

RMSE of total received power with reference to B-K model		
Scenario	Method	Error
LoS	Lambertian	0.64
LoS	Directive	0
NLoS	Lambertian	0.729
NLoS	Directive	0.089

4.2.2 Angle of Arrival / Angle of Departure (AoA/AoD)

At THz frequencies, due to the diffuse scattering mechanism, any reflection from the rough surfaces forms a cluster. However, the number of detectable clusters is usually small because of high reflection and penetration losses from rough materials later elaborated in Chapter 5.

The significant steps of identifying clusters in the simulation process are as follows:

1. To determine the specular reflection points either with an RTA (minimum path amplitude -150 dB).
2. To create 20 x 20 square tiles around each specular point with scattering area equal to M times correlation length. In [80], it is affirmed $M = 10$ times gives a considerable difference between input power of the transmitting antenna and scattered paths around -200 dB.
3. To take account of all angles (incidence, reflection, and scattering angle) for each path.
4. To compute the individual powers of all the scattered multipaths from the tiles by applying the respective equations from both models.
5. To calculate the received power by summing up the contributions of all the paths scattered from the tiles and applying the respective equations from both models.

Simulations are conducted to evaluate the relative received power of a rough plaster with surface roughness $\sigma_h = 0.15$ mm including the angular and temporal information of the scattered multipaths with respect to the specular reflection directions.

The results in Fig. 4.6 show the impact of surface roughness on the THz propagation channel and its influence on the received power in the specular direction. AoAs for LoS and NLoS

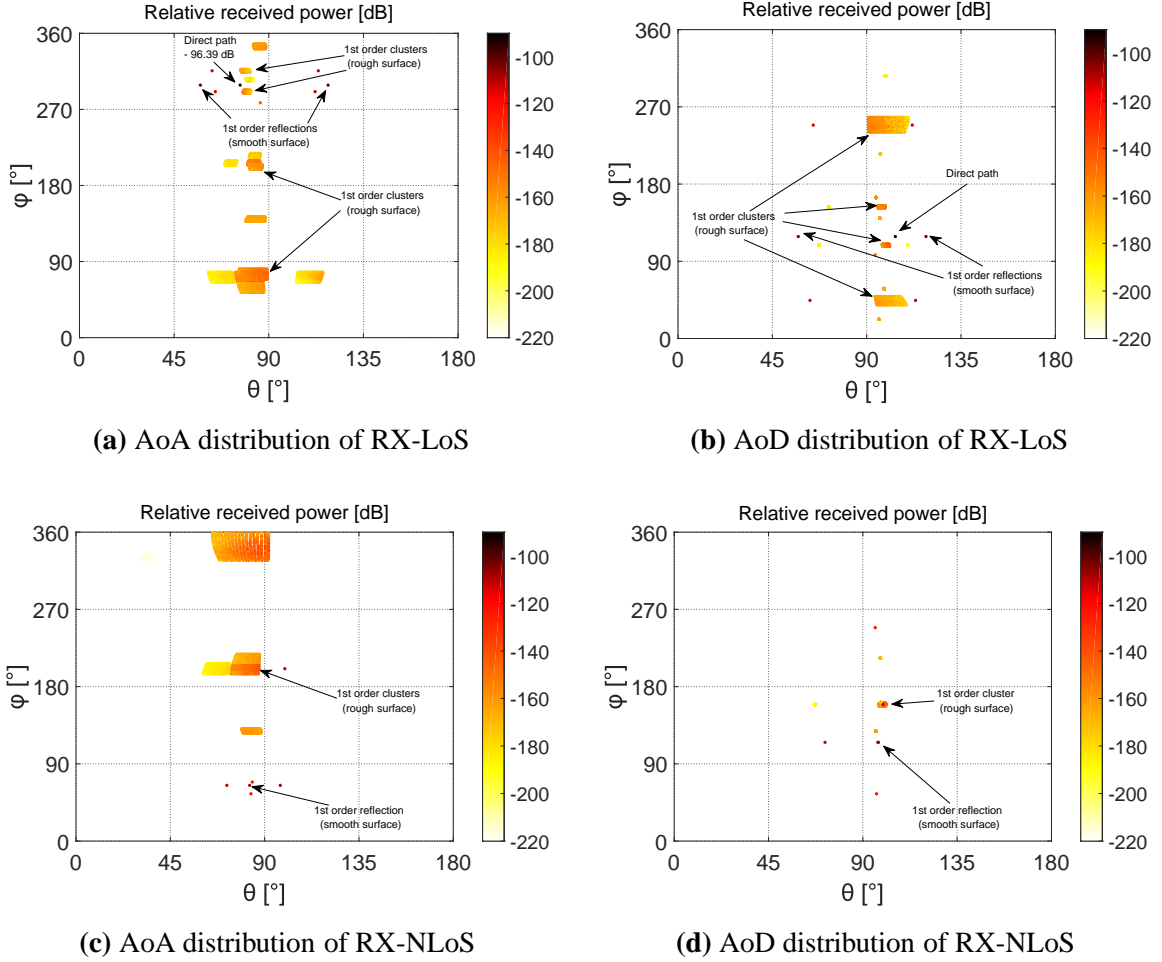


Figure 4.6: Relative received power of AoA/AoDs in the azimuth and elevation plane of the office room. The frequency is 300 GHz, $\ell_{cr} = 1.7$ mm, $l_x = l_y = 10 \ell_{cr}$, and $\sigma_h = 0.15$ mm.

scenario have identical received power distribution for all the multipath. The non-specular multipaths around the specular reflection path emerge when the incident path hits the rough surface. However, only dominant paths around the specular reflection are considered in the simulation process (i.e., in our case is a maximum of 400 non-specular diffuse scattered paths). The RTA simulates this phenomenon accurately and agrees well with literature which is already affirmed in the previous section. The threshold function of the RTA is used with the path loss threshold set to -200 dB. However, below this limit, the contribution from the diffuse scattered paths to the total received power is quite less. Moreover, AoDs' power distribution shows fewer clusters than AoAs. Owing to the fact that for second-order reflections, RTA considers only specular paths from the first encountered surfaces by neglecting the diffuse scattered multipaths. This is due to the already reduced power of the scattered multipath after hitting the first surface. For LoS scenario, about 7944 specular and non-specular paths are considered. On the other hand,

the RTA has found only 2568 valid multipaths for NLoS scenario.

4.2.3 Time of Arrival (ToA)

Fig. 4.7 shows the clustered behaviour of time of arrival (ToA) distribution for azimuth plane with respect to AoA. The multipaths arrive with particular ToAs based on the different path lengths traversed by them. Based on geometrical analysis, the specular reflection should arrive earlier and consequently consume shorter ToA relative to scattered paths with longer ToAs (due to larger paths). Our simulation results affirm that such relation of ToA and AoA does not hold for all clusters due to their dependency on the complex propagation environment. Hence, conform with that already published in literature. Unlike AoA/AoD, the clusters of ToA form a cone shape. Similar to AoA/AoD, the reflection paths which are closer to each other are combined to form a big cluster.

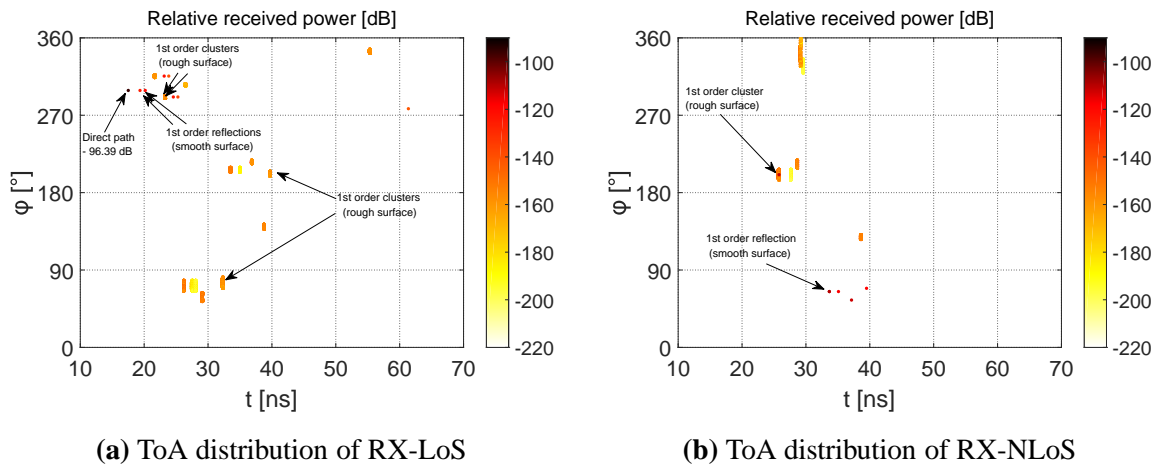


Figure 4.7: Relative received power over ToA and AoA in the azimuth plane corresponding to Fig. 4.6.

4.2.4 Channel Impulse Response (CIR)

The total propagation between a TX and a RX is defined by its multipaths. At THz frequencies, the multipaths also form a cluster pattern of CIRs around specular paths and their amplitudes decay exponentially with time as depicted in Fig. 4.8. Also in this case, the specular paths of respective clusters arrive earlier at the RX with respect to the diffuse scattered paths. Moreover, the multipaths' amplitudes reduce proportionally due to the influence of surface roughness on those with larger lengths. Further, the CIR results from the above figures closely resemble the

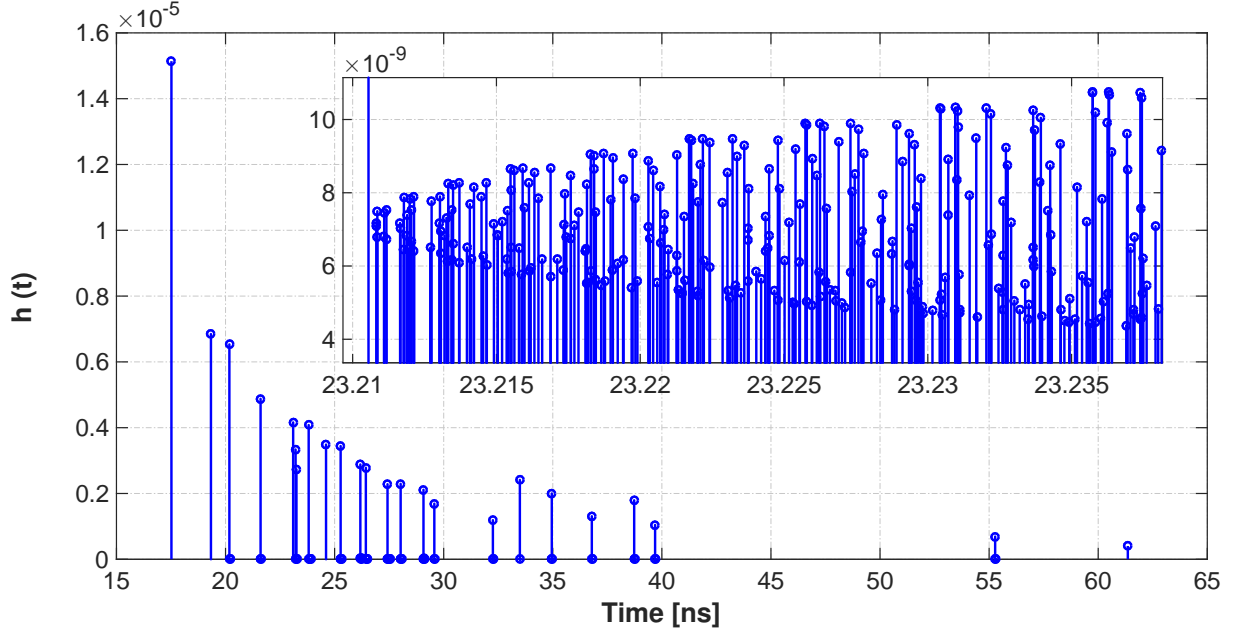


Figure 4.8: CIR of multipaths at RX-LoS employ the B-K model. The frequency is 300 GHz, $\ell_{cr} = 1.7$ mm, $l_x = l_y = 10 \ell_{cr}$, and $\sigma_h = 0.15$ mm.

Saleh-Valenzuela (SV) model [89,90]. Similarly, [91] has also reported the resemblance of their simulation results for THz indoor channel with this SV model. However, further experimental work of author [27] is still ongoing to augment the results mentioned in this research.

4.2.5 Channel Transfer Function (CTF)

In order to demonstrate a comparison between the surface scattering models along with their specific advantages and limitations, the ultra-broadband channel behaviour by using our self-developed RTA in terms of the frequency-domain CTF dynamics at 3201 frequency points for $f = 300 \dots 310$ GHz in LoS and NLoS scenarios is simulated. Fig. 4.9 and Fig. 4.10 depict the CTF results for the respective R-R, cB-K and mB-K models for Fig. 3.6 scenario. For LoS case, the respective average attenuation over the whole bandwidth is 97.02 dB, 100.86 dB and 101.59 dB. Meanwhile, the standard deviation for the respective models is 1.70, 5.96 and 5.29. However, for NLoS case the respective average attenuation is 110.09 dB, 109.90 dB and 107.95 dB with the standard deviation being 5.51, 5.46 and 5.20, respectively.

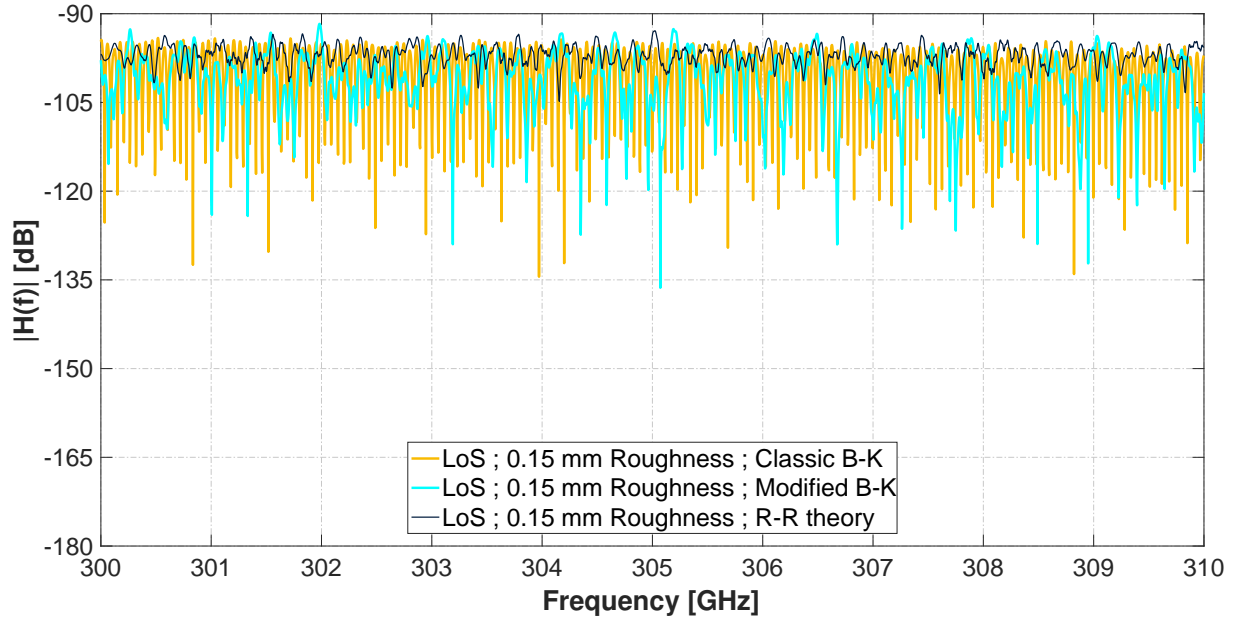


Figure 4.9: Comparison of CTFs between classical B-K, modified B-K, and R-R models in presence of slightly rough surfaces at RX-LoS ($x = 3.5$ m, $y = 4.45$ m, $z = 0.75$ m). The surface correlation length is $\ell_{cr} = 1.7$ mm, $l_x = l_y = 10 \ell_{cr}$, and $\sigma_h = 0.15$ mm.

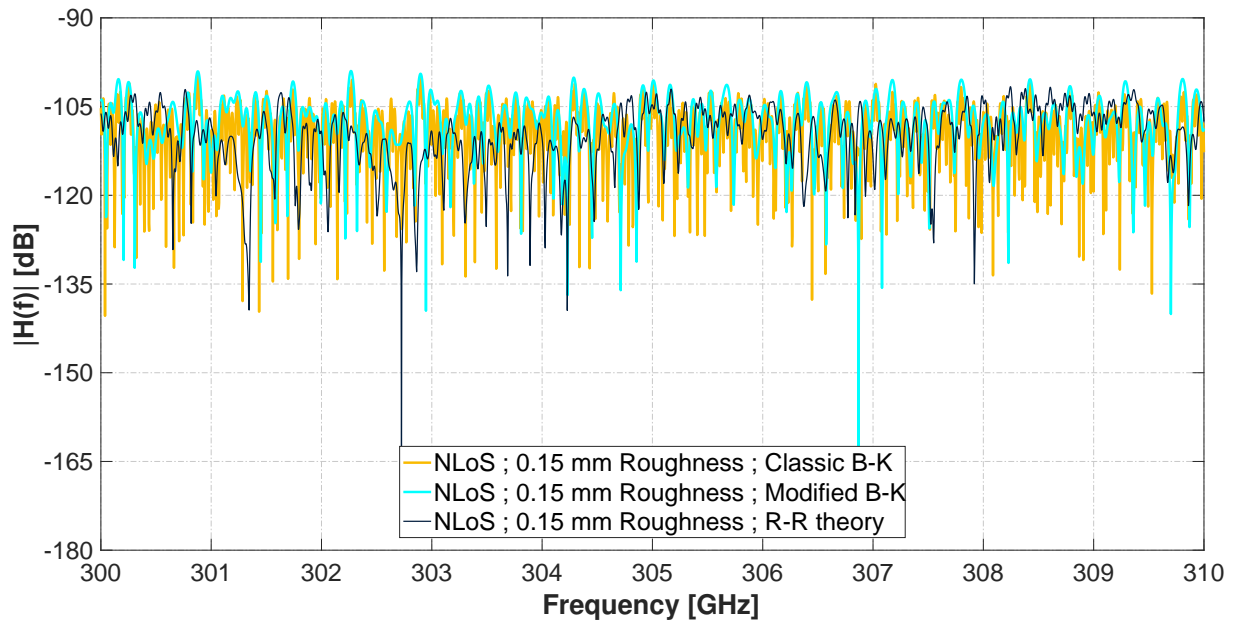


Figure 4.10: Comparison of CTFs between classical B-K, modified B-K, and R-R models in presence of slightly rough surfaces at RX-NLoS ($x = 1.7$ m, $y = 2.75$ m, $z = 0.75$ m). The surface correlation length is $\ell_{cr} = 1.7$ mm, $l_x = l_y = 10 \ell_{cr}$, and $\sigma_h = 0.15$ mm.

4.3 MIMO Propagation and Channel Modeling

The study of the propagation channels is not only an interesting research topic in itself, rather has important applications for the investigation of massive MIMO systems, which can improve the link capacity and/or reliability of wireless communication systems [92]. In massive Multiuser-MIMO (MU-MIMO) systems an access point uses numerous antennas to serve several single-antenna terminals using the same time/frequency resources. The performance of these systems may be affected directly by the diffuse propagation environment at THz frequencies. Hence, the motive here is to observe how the aforementioned unique propagation characteristics with diffuse scattering phenomena that depend on material properties (e.g. surface roughness, permittivity) map onto communication system characteristics such as capacity. Further, as the rough surface gives rise to an influx of multiple scattered paths (diffusely scattered field components) in addition to the specular reflected path, the anticipated multiplexing gain can apparently enhance the channel capacity.

Therefore, an indoor THz communication system is investigated, where a single array with multiple antennas is used to compensate for the high path loss. Specifically, we analyze the ergodic capacity for the THz system. Besides, this study is the first to consider the impact of diffuse scattering on massive MIMO over NLoS channels at THz frequencies. In the capacity analysis, we express the channel capacity into two parts, one is the capacity introduced by specular reflection, the second is the one introduced by scattered rays. Thus, our goal is to analyze the relationship between the capacity and the roughness factor, as well as the capacities introduced by different rays.

The foremost contributions of this study are summarized as follows:

- The implementation of ray-tracing algorithms developed for this study applying the extended Kirchhoff scattering model as proposed by Beckmann to the rough surfaces at THz frequencies.
- An analysis of how much leverage a massive MIMO system can possibly obtain out of high degrees of surface roughness factor creating an influx of scattered paths.
- Results for the achievable channel capacity of the scattered propagation environment in indoor LoS and NLoS THz massive MIMO channels.
- A tradeoff between rich multipath and high RX power in THz massive MIMO capacity.

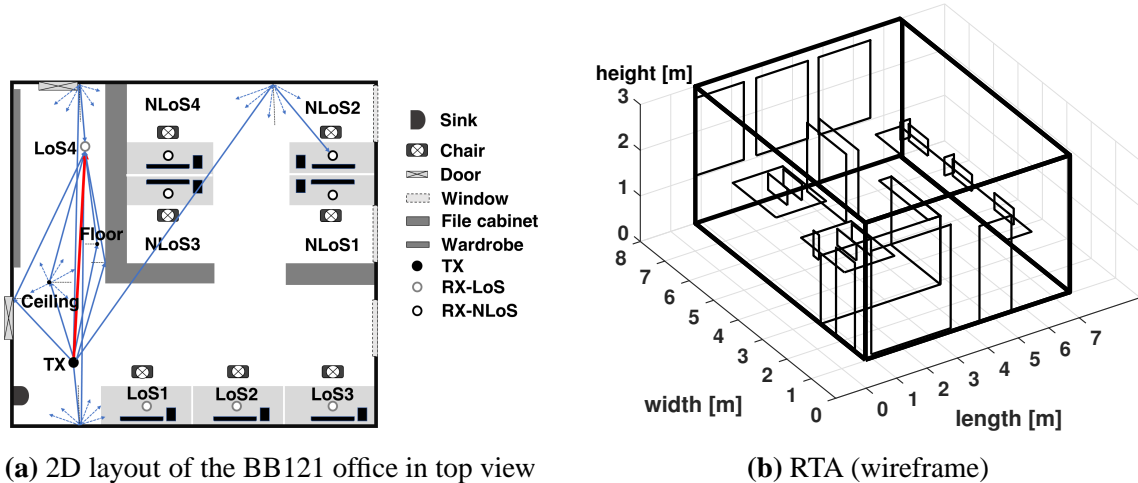


Figure 4.11: Real environment of the office room BB121.

4.3.1 Single User-MIMO Channel Capacity

Due to the fact that the simulations for this present study are carried out indoor in a small office room, and only in the atmospheric spectral window, we have neglected the atmospheric attenuation since its impact amounts to no more than 2.8 dB/km [3]. The modeled environment is shown in Fig. 4.11. Please note that in Fig. 4.11 (b) only those surfaces (faces) from our RTA are shown where first- and second-order reflections have occurred. Besides, simulations are conducted to evaluate the channel capacity for three rough plasters with different degrees of surface roughness. The key idea here is to use realistic statistical surface parameters measured by the authors in [18], and varying these for rough plasters as given in Table 3.1 with the target to investigate and demonstrate the influence of degree of roughness on the 300 GHz propagation characteristics.

We illustrate the channel capacity results on the formerly presented ray-tracing based statistical THz channel model with multiple-antenna configurations. Fig. 4.11 depicts the layout of the simulated environment, comprising of one TX, 4 LoS receivers (RX-LoS) and 4 NLoS receivers (RX-NLoS), distributed at 8 different locations in total. The transmitting antenna is an 8 x 8 planar array, kept away from any obstructions in order to provide maximum coverage. So, $N = 64$ antennas are assumed at both TX and RX ends. It is also assumed that both TX and RX have perfect channel state information, since beamforming at both TX and RX is necessary to compensate the severe path loss in THz. Besides, we consider both single-user MIMO (i.e., transmitting to each user independently) and MU-MIMO (i.e., transmitting to each user simultaneously) for computing the channel capacity. At the TX side, waterfilling-based power

allocation is used to achieve maximum capacity, resulting in the MIMO channel capacity [94]

$$C = \sum_{n=1}^N \log_2 \left(1 + \frac{p_n}{\sigma^2} \lambda_n^2 \right) \quad (4.2)$$

where λ_n is the n th singular value of the channel matrix \mathbf{H} ; p_n is the allocated power on the n th data stream obtained from the waterfilling algorithm, satisfying $\sum_{n=1}^N p_n = P_T$; SNR is defined as the ratio of the total transmitted power P_T over the noise variance σ^2 . It is noteworthy to mention that an increase in capacity is expected when the SNR is kept constant owing to the increase in the channel richness. To obtain *ergodic* capacity, we simulate a wideband channel with 10 GHz bandwidth at the carrier frequency of 300 GHz. It is worth mentioning that the roughness is assumed (or approximated) to be constant over 10 GHz bandwidth (*cf.* Fig. 2.18 at 300 GHz). The channel is divided into 10^3 subchannels whose capacity is calculated by Eq. (4.2) and then averaged to obtain the ergodic capacity.

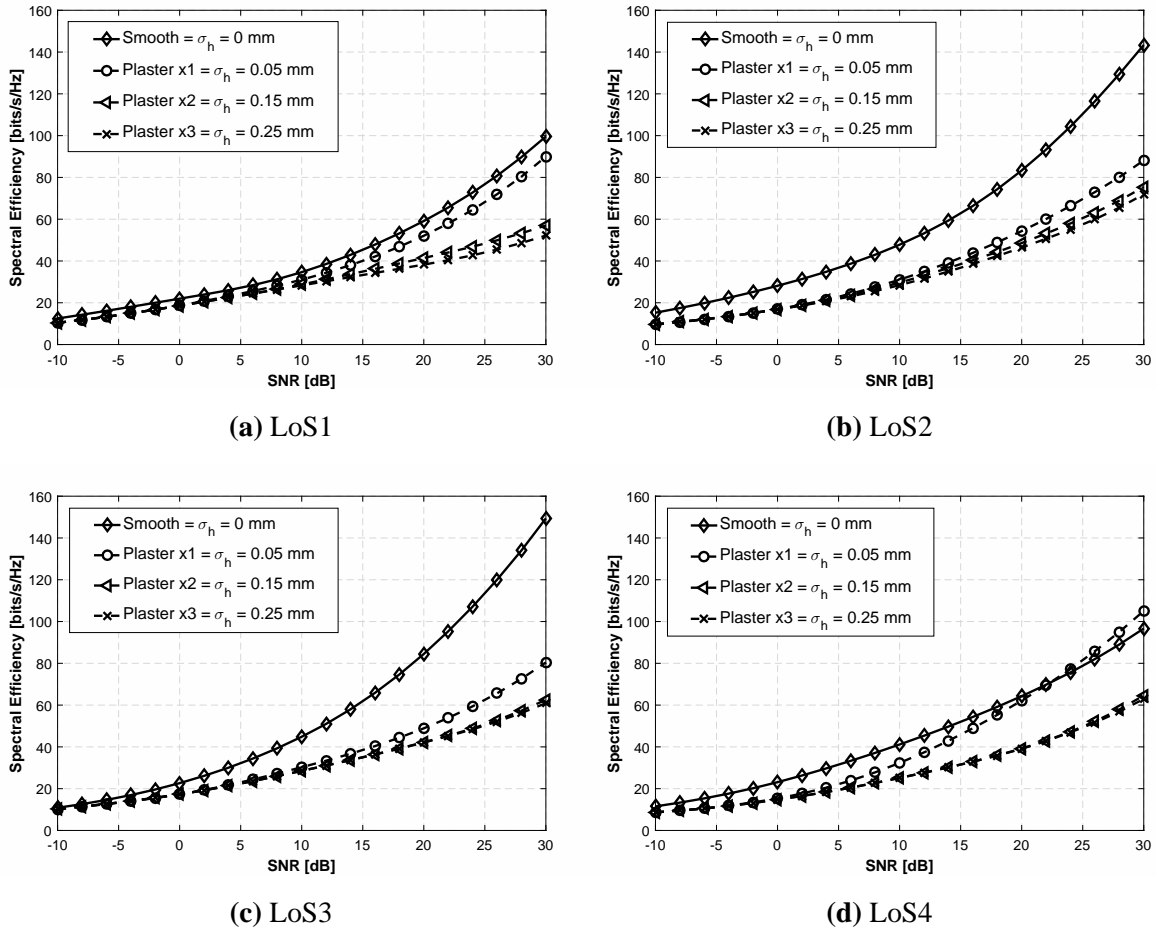


Figure 4.12: Channel capacity of LoS1–LoS4.

Fig. 4.12 plots the MIMO ergodic channel capacity for four LoS receiver locations. It is

observed that the diffuse scattering reduces the channel capacity. In LoS2 and LoS3 locations, even a minor roughness, i.e., 0.05 mm can drastically degrade the channel capacity. In contrast, for $\sigma_h = 0.15$ mm a significant degradation of the channel capacity can be observed in LoS1 and LoS4 locations. However, when the $\sigma_h > 0.15$ mm the channel capacity further decreases only slightly with increasing roughness in all LoS locations. Fig. 4.12 implies that the diffuse scattering is unfavorable in the LoS scenarios. Intuitively, as the surface roughness σ_h increases, the power of the scattered channel paths tends to be negligible compared to that of the strong direct path. As a result, the degree-of-freedom of the MIMO channel tends to one (no spatial multiplex gain), which is obviously unfavourable to MIMO channel capacity. In case of smooth environments, the prominent difference in capacity at 30 dB SNR between the four LoS receiver locations is due to the total number of reflections received for that particular location, i.e., LoS1 exhibits 9 reflections in contrast to the 14 reflections for LoS3. Here, the minimum path amplitude -150 dB is applied. However, in case of rough environments the observed prominent difference due to the multipaths alters depending on the origin of the paths as to whether it is reflected from smooth or rough objects in that environment.

Next, the NLoS scenarios are presented in Fig. 4.13. Unlike the negative impact of the diffuse scattering on the channel capacity in LoS case, the diffuse scattering can potentially boost the channel capacity in NLoS locations. For example, in NLoS2 and NLoS3, capacity of all the channels with rough surfaces is much higher than that of the smooth ones. This is due to the rich scattering introduced by surface roughness. It is noteworthy to mention that the reason behind the capacity reduction for NLoS4 location is due to the least number of specular and scattered paths. However, it should be noted that surface roughness is not always advantageous to the channel capacity as observed in NLoS1 and NLoS4. For NLoS1, even a higher roughness of 0.25 mm can degrade the channel capacity. This degradation is probably due to the power loss of the diffuse scattering. The diffuse scattering actually increases the scattering richness and simultaneously decreases the channel strength. Basically, the scattering phenomena leading to spatial whitening can increase the capacity, unless it is associated with a loss of SNR. This is the reason why diffuse scattering has different effects on channel capacity in NLoS scenarios. It should be noted that in LoS scenarios as shown in Fig. 4.12, the direct path component rather than the multipath richness impose the main impact on the channel capacity. This is the reason why we cannot observe these different effects in LoS scenarios. From the observations in Figs. 4.12 and 4.13, we witness that the diffuse scattering affects the capacity of massive MIMO negatively in the presence of a direct path and positively when there is no direct path.

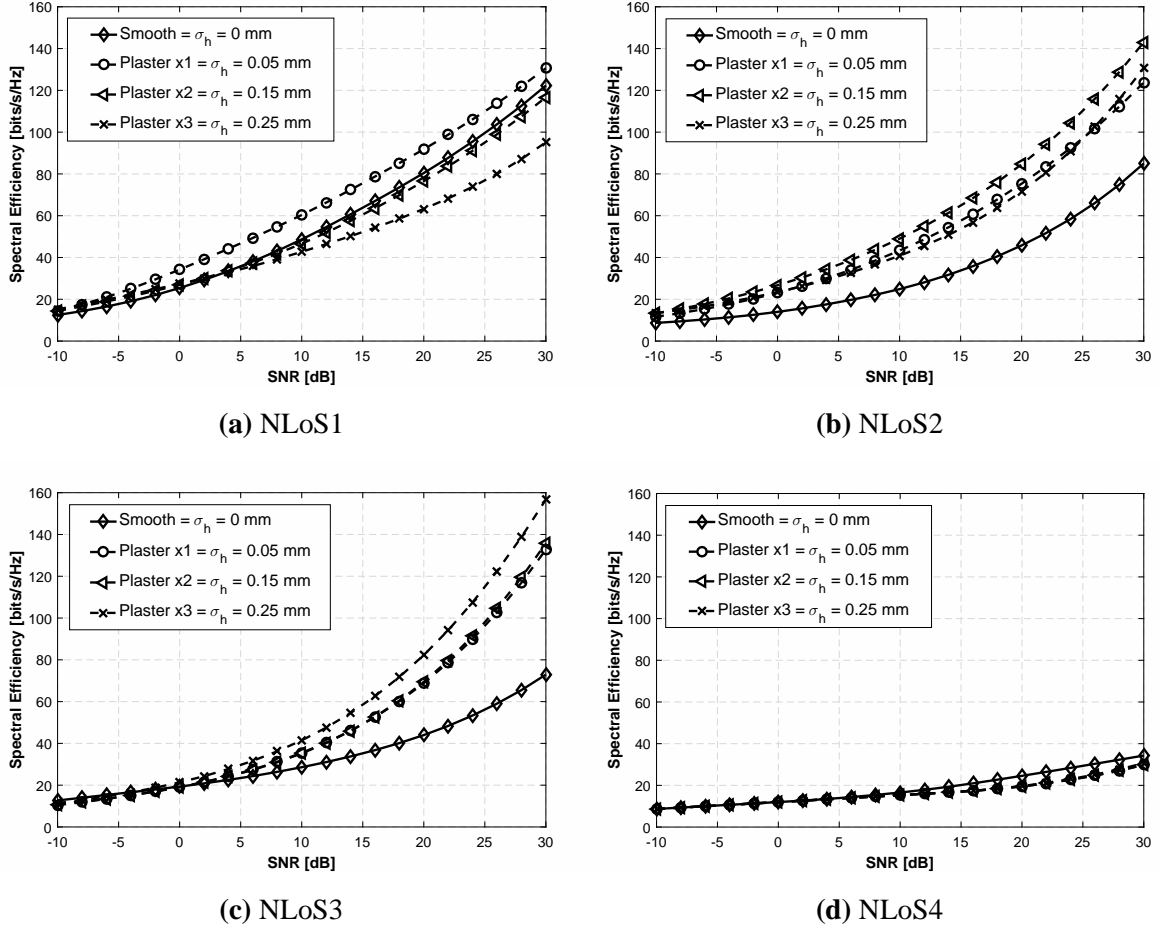


Figure 4.13: Channel capacity of NLoS1–NLoS4.

4.3.2 Multi User-MIMO Channel Capacity

The channel capacity of single-user MIMO (SU-MIMO) is plotted graphically in Fig. 4.12 and Fig. 4.13. Observing the MU-MIMO, let us suppose that the TX still has $N = 64$ antennas, but for RX we only have one antenna in each RX location. Consequently, we have one 64-antenna TX and 8 single-antenna users as RX. The results for channel capacity are shown in Fig. 4.14(a) and (b) for LoS and NLoS, respectively. For LoS case similar to the SU-MIMO, the diffuse scattering degrades the channel capacity. Note that the diffuse scattering makes the power of scattered paths too low, and the capacity mainly depends on the angular difference of the direct path of each user. Since AoDs of LoS1–LoS3 are very similar as shown in Fig. 4.11 (a), the capacity of the rough channel exhibits large degradation compared to that of smooth channel. For the NLoS case, as shown in Fig. 4.14(b), we can see that the diffuse scattering can boost the channel capacity at high SNR, thanks to the rich scattering introduced by the diffuse scattering.

4.4. Concluding Remarks

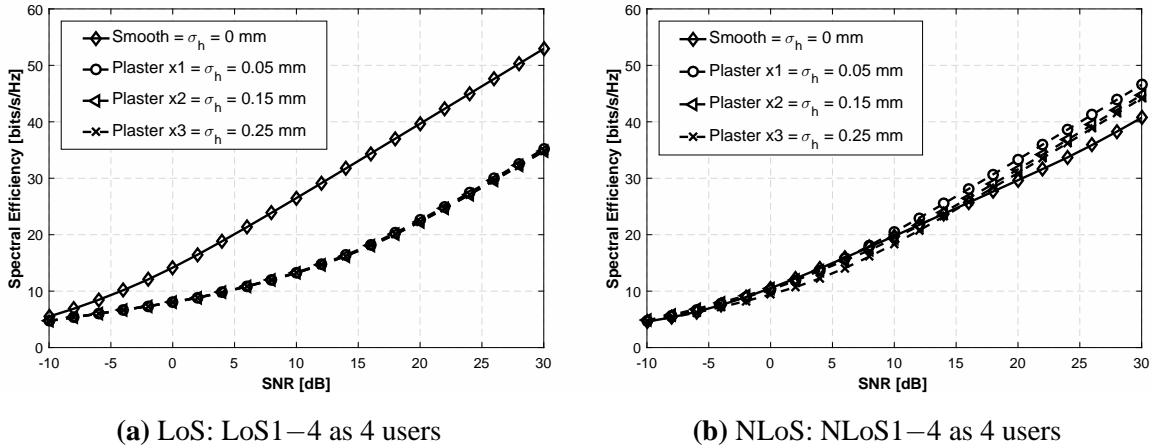


Figure 4.14: Channel capacity of MU-MIMO with $N = 64$ TX antennas and 4 single-antenna users as RX.

4.4 Concluding Remarks

This chapter unveils the need for developing a THz RTA to overcome the conventional GHz RT limitations:

⇒ We developed a novel THz 3D RTA tool based on GUI with distinct THz wave characteristics to support the proposed THz scattering models. We integrated the most famous THz scattering models of rough surfaces, mentioned in the previous chapter, to develop this self-programmed RTA tool using MATLAB. The THz RTA has been validated by comparing the path loss against measurements from the literature of an earlier publication by modeling similar LoS and NLoS scenarios for correctness and comparison.

⇒ The GUI system for our RTA tool is a user friendly interface, thus can be operated without any prior MATLAB experience to simulate THz scenarios. Apart from the major outputs of propagation predictions in terms of quantities such as received and scattered power, AoA, AoD, ToA, CxIR, CTF, and PDP, our RTA delivers results in a number of ways. For instance, it provides visual presentations such as coverage maps, power distributions, angular distributions, PDPs, and CIRs within the modeled environment. All output files produced by the RTA are in a readable ASCII format. This THz RTA is also capable of importing user defined antenna patterns from full-wave electromagnetic simulators such as CST Microwave Studio. The user can also input the roughness parameters such as σ_h , ℓ_{cr} , along with the ϵ_r to simulate and study the influence of rough materials on the ultra-broadband THz propagation characteristics.

⇒ Upon comparison of the scattering models, our simulation results affirm that the ER model though proposed for channel modeling at 60 GHz can be employed for modeling THz channels

as well.

⇒ Finally, the channel capacity results on the ray-tracing based statistical THz channel model with multiple antenna configurations illustrate that the diffuse scattering enhances the channel capacity due to the contribution from strong multipaths in case of NLoS scenario. This capacity increase further owes to the spatial multiplexing gain. The simulation results conclude that the influence of diffuse scattering is not desirable in LoS scenario. However, the high multipath observed in the NLoS scenario is a desirable characteristic for a THz communication channel.

Novel THz Material Characterization Techniques

During the last decade, THz frequency region, 0.3–1 THz, has been massively studied and expected to be one of the possible resources exploited for future wireless communication networks beyond 5G. Wireless transmission over this band will offer several advantages such as Tb/s channel capacities, and small size transceivers [95]. However, this technology needs to address a couple of challenges in order to yield outstanding performances. In fact, THz application extends to security, medical, biology, aerospace technology, and nondestructive evaluation of materials used in airplanes, such as foams, plastic, and fiberglass composites [96]. Therefore, characterization of material dielectric properties at these frequencies is of paramount importance. It has to be accomplished with high precision through appropriate measurement and extraction techniques. While material characterization is extensively investigated at lower frequencies, published information is still scarce for applications within the THz frequency spectrum region of interest. In fact, the main techniques for characterizing dielectrics at THz frequencies are namely, time-domain spectroscopy (frequency down-conversion) and measurements using a VNA (frequency up-conversion) [97]. Nevertheless, the selection of the most suitable measurement method (i.e., free space or guided wave transmission line methods etc.) depends on some parameters such as the material phase, specimen size/shape, temperature, anisotropy, inhomogeneity, and frequency range [98]. Specifically, this work reports the first ever transmission measurements for a wide choice of indoor materials such as *wood, plastic, paper, brick, glass* and *leather* at frequencies from 750 GHz to 1.1 THz using up-conversion (frequency-domain) method employing *Swissto12* system. The common as well as novel inversion methods used

to convert the calibrated scatter data into intrinsic material parameters (e.g. permeability and permittivity) are also outlined. To push our sleeve farther up, some of the sources of errors in frequency up-conversion based measurement systems are also discussed.

So far, there are not many investigations for characterizing intrinsic properties of materials at THz frequencies. In [99] the measured complex dielectric and magnetic properties of liquid and solid biological tissues removed from human arteries at frequency range of 110 to 170 GHz are presented. The evaluation of the dielectric properties is performed using the Nicolson-Ross-Weir (NRW) conversion process. In [100], an extensive calculation analysis of substrate permittivity, characteristic impedance, total loss, and dielectric loss tangent is presented for up to 500 GHz frequency range. Furthermore, THz Metamaterial samples are characterized in [101]. In [31], the characterization of the dielectric properties of a variety of common building and plastic materials between 100 and 1000 GHz using THz-TDS transmission system is presented. In fact, the existing reports regarding dielectric properties of indoor materials are limited, i.e., leather and mirror glass are not characterized yet. Therefore, providing a new database of dielectric properties based on a very sophisticated material characterization kit (MCK) already validated in [102] is worth having. The presented results are a part of the larger measurement campaign seeking material parameters of a variety of indoor materials between 0.75 and 1.1 THz. Next, this research work is presumed to be quite useful and helpful for accurate modeling of future indoor wireless communication channels at THz frequencies. In addition, the measured material parameters may also prove beneficial for investigation and development of high-speed wireless networks. This chapter entails research published in [103, 104].

5.1 State-of-the-art Spectroscopic Technique in THz

THz Spectroscopy is one of the rapidly evolving field of THz technology with major applications in medical imaging, security screening, scientific spectroscopy, communications, and many more. It is based on the strengths of emission or absorption specifications for rotational and vibrational excitations of the molecules from material specimen in THz region. More precisely, many molecules especially chemical and biological ones, provide fingerprint spectroscopic lines in the THz spectral region from 300 GHz to 10 THz. Thereupon, intrinsic material parameters can be identified by their characteristic resonant peaks. Honestly speaking, the THz waves can be thought of as a new addition to the electromagnetic spectrum occupying the region between microwaves and infrared, as shown in Fig. 5.1.

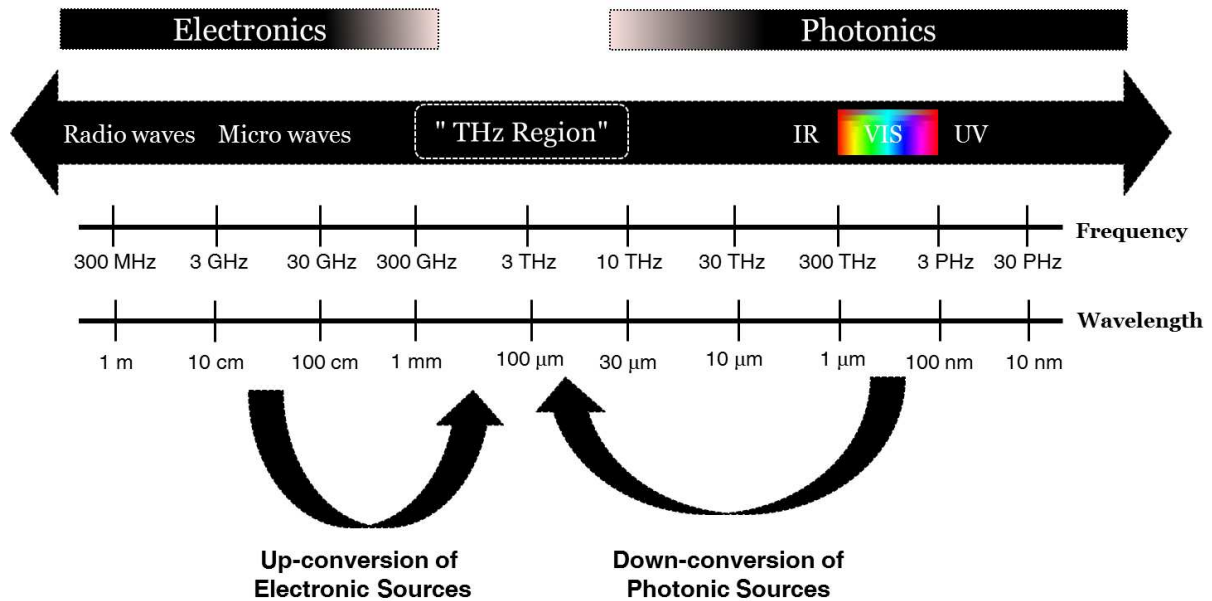


Figure 5.1: The EM spectrum from radio waves to optical region, highlighting the location of the THz Region.

From a spectroscopic point of view, the THz spectral region from 300 GHz to 10 THz has not yet seen the technological development of optical or microwave frequencies with the result that commercial spectrometers covering the entire spectral range are so far not widely available. This is primarily due to the difficulty of generating and detecting THz frequencies. Broadly speaking, to measure intrinsic material spectroscopic responses, the state-of-the-art THz systems based on time-domain and frequency-domain methods are classified as follows: (i) THz-TDS systems [31]; (ii) THz quasi time-domain spectroscopy (THz-QTDS) systems [105]; (iii) continuous wave THz (cw-THz) systems [106]; and (iv) frequency modulated continuous wave (FM-CW) radar transceiver systems [107]. However, each method is confined to specific frequencies, materials and applications in its own constraint. In addition, MCK developed by *Swissto12* is now commercially available (*cf.* Fig. 5.3a) which in conjunction with VNAs enables the measurement of both the reflection coefficients (S_{11} , S_{22}) and the transmission coefficients (S_{12} , S_{21}) in the WM-250 (or equivalent WR-01) waveguide band that supports frequencies from 750 GHz to 1.1 THz, explained briefly in following section.

5.2 Measurement Techniques

A number of techniques exist for characterizing of materials' dielectric and magnetic properties at THz frequencies. In practise, different techniques work better for different spectroscopic information or types of measurements. However, two eye catching techniques namely free space [108, 109] and waveguide measurement (or transmission/reflection (T/R) line) techniques [102, 110], are proven commonplace among VNA-based THz material characterization research community due to their ease of use along with reasonable accuracy explained below in brief.

5.2.1 Free Space Technique

Free space methods are based on placing a sample (i.e., unknown material specimen) in the space between the transmitting and receiving antennas and then let a plane EM wave pass through it [111]. The measurement principle depends on the fact that phase and attenuation of the passing or reflecting wave varies according to the material's properties which are defined by the relative complex permittivity ϵ_r expressed by the [111] as

$$\epsilon_r = \frac{\epsilon}{\epsilon_0} = \tilde{\epsilon}_r - j\tilde{\epsilon}_r = \tilde{\epsilon}_r - j\frac{\sigma}{\omega\epsilon_0} \quad (5.1)$$

where $\tilde{\epsilon}_r$ is the real part of permittivity, and is often called permittivity for short. $\tilde{\epsilon}_r$ is the imaginary part of permittivity and referred to as the dielectric loss factor. The loss factor is related to the energy absorption from the material. In the above definition, $\tilde{\epsilon}_r$ is always expected to be a positive number since energy conservation dictates that a passive material cannot exhibit gain [112]. Thereupon, the loss factor should not be negative. Next, σ is the conductivity of the sample, $\epsilon_0 = 8.854 \times 10^{-12}$ F/m being the permittivity of vacuum which is a fundamental constant of nature, and $\omega = 2\pi f$ refers to the angular frequency of the THz waves.

Another quantity, a loss tangent $\tan \delta$ is often introduced which is also associated with the energy absorption of a material specimen, defined as the ratio of the imaginary part to the real part of complex permittivity as

$$\tan \delta = \frac{\text{Im}(\epsilon_r)}{\text{Re}(\epsilon_r)} \quad (5.2)$$

As such, Eq. (5.1) can be expressed from [111] as

$$\varepsilon_r = \tilde{\varepsilon}_r(1 - j \tan \delta) \quad (5.3)$$

Similarly, the complex relative permeability of the material relative to free space is defined as [113]

$$\mu_r = \tilde{\mu}_r(1 - j \tan \delta) \quad (5.4)$$

To derive the complex relative permittivity $\varepsilon_r(\omega)$, the reflection $\Gamma(\omega)$ and transmission $T(\omega)$ coefficients need to be obtained first. Then, by assuming the material sample thickness as d , the transmission coefficient excited with a free space transversal EM wave propagating through the material specimen with permittivity $\varepsilon = \varepsilon_0 \varepsilon_r$, and permeability $\mu = \mu_0 \mu_r$ can be expressed as

$$T(\omega) = e^{-j\omega\sqrt{\mu\varepsilon}d} = e^{-j\frac{\omega}{c}\sqrt{\mu_r\varepsilon_r}d} \quad (5.5)$$

And the reflection coefficient is

$$\Gamma(\omega) = \frac{\sqrt{\frac{\mu_r}{\varepsilon_r}} - 1}{\sqrt{\frac{\mu_r}{\varepsilon_r}} + 1} \quad (5.6)$$

From [114], without considering multiple reflections inside the material the scattering parameters of the sample at the surfaces are given by

$$S_{11} = \frac{\Gamma(1 - T^2)}{1 - \Gamma^2 T^2} \quad (5.7)$$

$$S_{21} = \frac{T(1 - \Gamma^2)}{1 - \Gamma^2 T^2} \quad (5.8)$$

Once calibrated and processed, S_{11} and S_{21} are determined, then an inversion algorithm is applied to Eq. (5.7) and Eq. (5.8) for extracting material parameters. These inversion methods are derived by solving the boundary value problem of a plane wave interacting with a planar slab of material specimen [112]. For instance, in case of nonmagnetic materials (i.e., $\mu_r = 1$) the complex relative permittivity ε_r can be determined by employing Eq. (5.8) as a root-finding problem and applying the Newton Raphson method as described in [114]. On the other hand, one can obtain the relative permittivity as well as the relative permeability from the Eq. (5.7) and Eq. (5.8) according to Nicolson-Ross approach [115], one of the numerical approaches used

in this study.

Advantages of free space technique

Free space methods (i.e., focused beams) for measurements of dielectric and magnetic properties of materials are preferred over waveguide measurement techniques for the following main reasons:

- For materials such as plasters, ceramics, and composites this technique is favorable owing to their inhomogeneity due to the variations in manufacturing processes. Because of inhomogeneity the unwanted higher order modes (*cf.* Sec. 5.4 for details) can be excited at an air-dielectric interface in case of waveguides.
- The techniques for free space characterization of materials are nondestructive and non-contact. Thus, allowing reflection and transmission measurements without any physical contact with the sample. Because of this feature, these methods have a distinct advantage over waveguide techniques concerning the dielectric measurements at high temperatures.
- The use of free space techniques is most favorable because there is no interface between the material specimen and guide wall. For instance, in the waveguide methods it is necessary that the waveguide cross section completely spans the space within the material with negligible air-gaps. The unusually large systematic errors sometimes experienced are an aftermath of the air-gaps, when present between the waveguide walls and the sample preferably guide the THz energy through these rather than the specimen. However, in case of free space systems, the energy is confined to an area within a large specimen so that no air-gaps exist.

Disadvantages of free space technique

- Requires flat and relatively large sized specimen, which can be troublesome owing to the expenses and manufacturing impracticality. Furthermore, due to the large sizes of the samples the transmitted signal level becomes too low for the accurate measurement of changes in frequency [116].
- Most commonly used for measurement of samples with medium loss.
- Multiple reflections between antenna and surface of sample.

- Diffraction effects at the edge of the sample.

As portrayed in the Figs. 5.14–5.10, the high losses of common indoor building materials at THz frequencies make this method seemingly unfavourable.

5.2.2 Waveguide Measurement Technique

Waveguide measurement techniques or transmission/reflection line methods involve placing a sample in a section of waveguide and measuring the two port complex scattering parameters with a VNA. From these measured parameters after post processing, e.g., applying NRW method [115, 116], the intrinsic properties such as dielectric permittivity and magnetic permeability of the specimen can be calculated. The scattering parameters represent the signals that are transmitted (S_{12} , S_{21}) and reflected (S_{11} , S_{22}) by a material specimen when an incident wave is directed at the sample. It is noteworthy to mention that the intrinsic properties of a material are typically independent of the size and shape of a material. However, the scattering parameters depend on geometrical factors such as thickness, roughness, and angle of incidence. Calibrations for the waveguide are accomplished using short circuit for each end of waveguide and transmission with and without the sample holder.

Advantages of waveguide technique

- Waveguide techniques are commonly used for measurement of samples with medium to high loss.
- It can be used to determine both the permittivity and permeability of material specimen.
- Relatively smaller sample size at THz frequencies.

Disadvantages of waveguide technique

- Measurement accuracy is limited by the air-gap effects.
- Low accuracy when the sample length is the multiple of one-half wavelength in the material.

At THz frequencies, the common indoor building materials have high reflection and penetration losses [117]. In addition, the incident angle to the material increases the penetration

loss through increased path length inside the material. Consequently, VNA-based waveguide measurement techniques in *transmission mode* are the most favorable with an incentive to get on board [118].

5.3 Measurement Characterization Kit *Swissto12*

The potential of modern THz systems in material characterization offers a unique solution in imaging, sensing, spectroscopy and communication. Meanwhile, the academia as well as industry are reviewing how this emerging THz field might be implemented in a variety of “real world” applications by sharing their experimental database to the world, ranging from the materials’ dielectric properties [120], to material surface textures [121] and the molecular spectroscopic database [122].

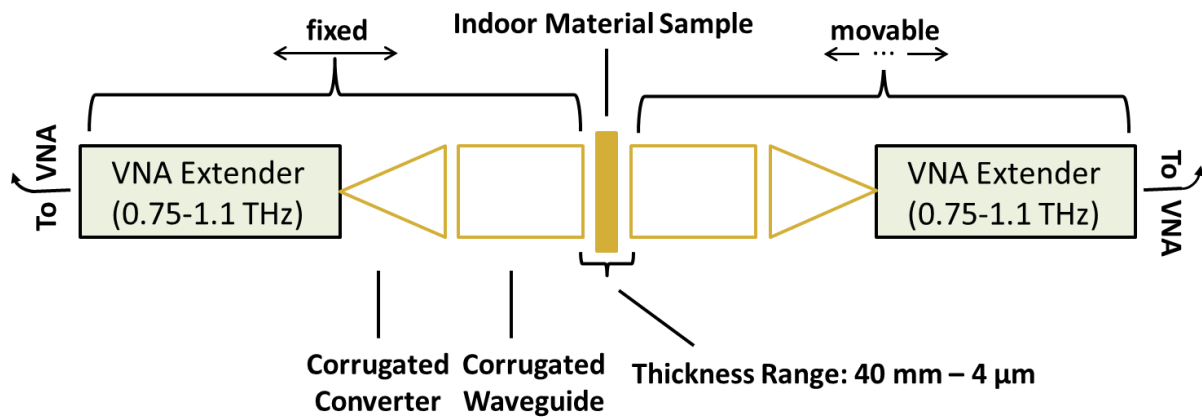
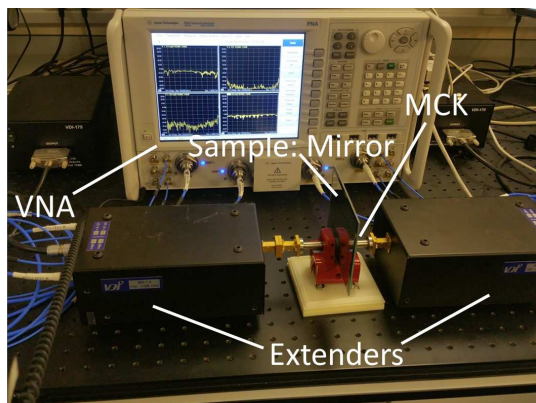
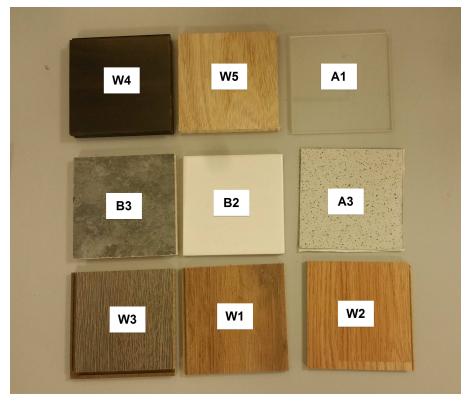


Figure 5.2: Schematic diagram of *Swissto12* MCK.

The experimental system for the THz transmission measurements in this study comprises of three parts, vector network analyzer (VNA), the *Swissto12* MCK waveguide system, and two frequency extension modules for measuring different indoor materials in the frequency range 750 GHz to 1.1 THz as shown in Fig. 5.2. The chosen THz frequencies are produced by the VNA using the extension modules and the output signal then traverses through a rectangular waveguide. The interconnecting gap between the rectangular frequency extension module waveguide and MCK’s corrugated waveguide is bridged by a corrugated conical horn antenna at the narrow aperture transiting from a circular to rectangular waveguide. The purpose for this transitional waveguide design is to accomplish the THz transmission in an enclosed environment with minimal losses as shown in Fig. 5.3a. The transitional horn or corrugated converter is connected



(a) MCK and VNA



(b) Material Samples

Figure 5.3: The 0.75 to 1.1 THz VNA system at University of Glasgow.

to the rectangular waveguide with adjustable flanges which are of standard size for the VNA extenders accommodating a compatible design for the waveguide converter components. Furthermore, the left hand segment of the setup is fixed as opposed to the movable right one for the ease of characterizing material samples with different thicknesses. Two-port short, open, load, and through (SOLT) WR-01 waveguide standards are acquired to calibrate the measurement equipment. This calibration streamlines the systematic errors between VNA transceivers and waveguide flanges. As the indoor materials are not chemically pure, we have selected two locations and recorded three readings for each at laboratory temperature $18^{\circ}\text{C} \pm 0.2^{\circ}\text{C}$ with humidity $30\% \pm 2\%$.

5.4 Description of Material Samples

We have characterized six common indoor building material groups encountered in the indoor wireless propagation channel. In addition to channel modeling, the study of propagation through different indoor materials can expedite the development of a basic theory for pulse shaping and receiver design. The knowledge of material samples' thicknesses is mandatory in extracting the material parameters and hence, the average of the thicknesses of 20 indoor materials categorized in six material groups measured at five different locations is tabulated in Table 5.1. However, in view of the limitations *only 9 materials* namely $W1$, $W2$, $W3$, $W4$, $W5$, $A1$, $A3$, $B2$ and $B3$ are chosen from Table 5.1. The electrical parameters of these three smooth ($A1$, $A3$, $B2$) and remaining six slightly rough ($W1$, $W2$, $W3$, $W4$, $W5$, $B3$) are then obtained using FMCW radar system in [123] but with a THz source of 250 GHz, further tabulated in Table 5.2. These

measured electrical parameters at 250 GHz are considered constant at the carrier frequency of interest as well affirmed by [31].

Table 5.1: List of measured materials with their thickness.

Material group	ID	Sample	Thickness
Wood	W1	High-Density Fiberboard (Thick)	7.5 mm
	W2	High-Density Fiberboard (Thin)	5.5 mm
	W3	High-Density Fiberboard (Underlay wood fibre)	12 mm
	W4	Bamboo (hard wood)	14 mm
	W5	Natural wood	10.5 mm
	W6	Pine wood	8.9 mm
Plastic	A1	Glass-look cast acrylic	4.75 mm
	A2	Vinyl flooring	4.5 mm
	A3	Vinyl tile sheet	1.2 mm
Paper	P1	Ingrain wallpaper	0.6 mm
	P2	Carton (white corrugated)	2.5 mm
	P3	Hardboard paper	3.9 mm
	P4	Hardboard with paper	3.92 mm
Brick	B1	Clay brick	12 mm
	B2	White ceramic wall tile (plain)	6.5 mm
	B3	Brown ceramic wall tile	9.7 mm
Glass	G1	Window glass	3.85 mm
	G2	Mirror glass	2.9 mm
Leather	L1	Synthetic leather (Faux)	4.5 mm
	L2	Genuine leather (brown)	1.4 mm

Measured Scattering Parameters

We employed the (VNA-based) *Swissto12* MCK THz transmission waveguide measurements system corresponding to waveguide band WM-250 for measuring scattering parameters (S_{21} and S_{11}). These measured S_{21} and S_{11} of all the six material groups namely, *wood*, *plastic*, *paper*, *brick*, *glass* and *leather* at frequencies from 750 GHz to 1.1 THz are illustrated in Figs. 5.4–5.15.

5.4. Description of Material Samples

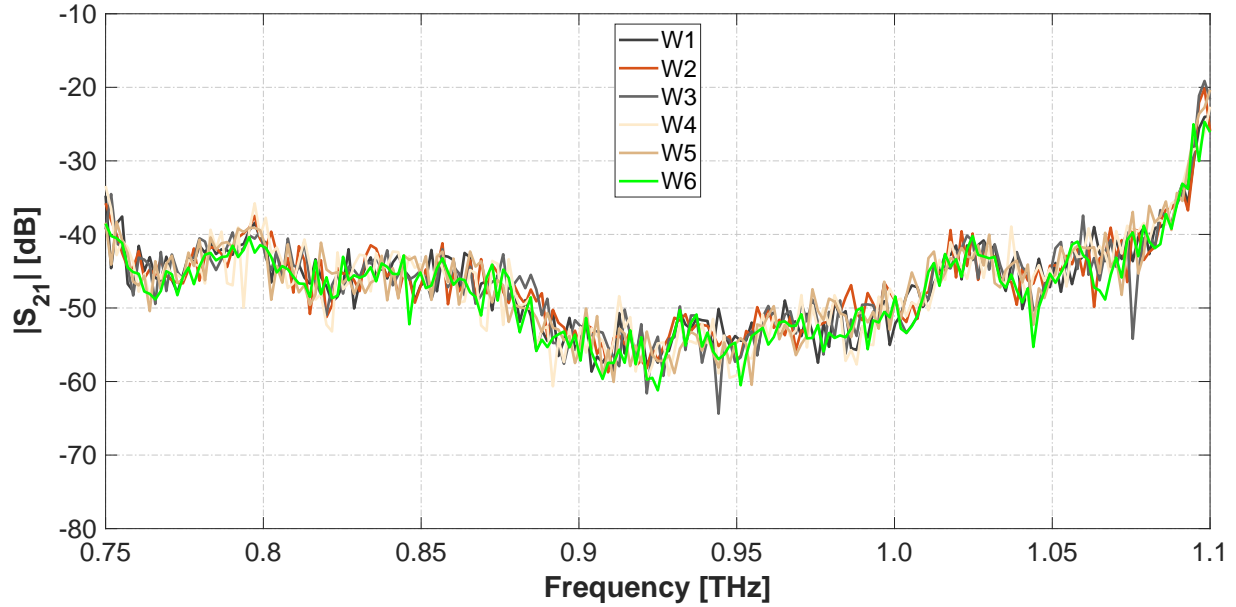


Figure 5.4: Measured S-parameter S_{21} [dB] versus frequency of indoor materials using MCK system (*Material Group: Wood*).

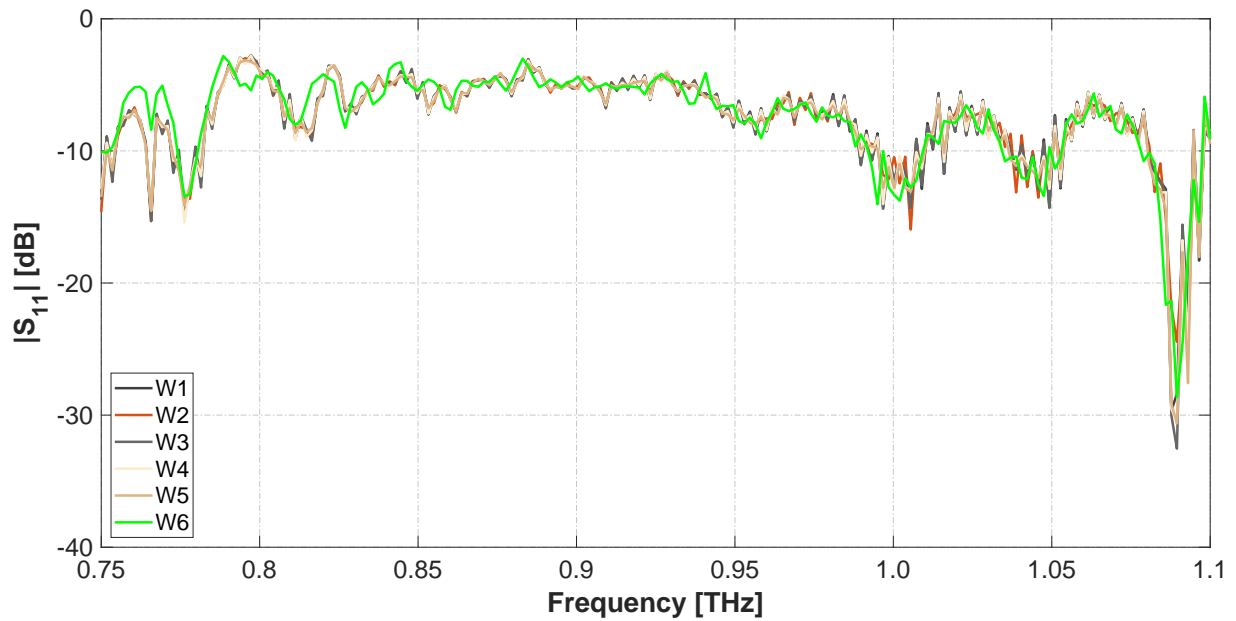


Figure 5.5: Measured S-parameter S_{11} [dB] versus frequency of indoor materials using MCK system (*Material Group: Wood*).

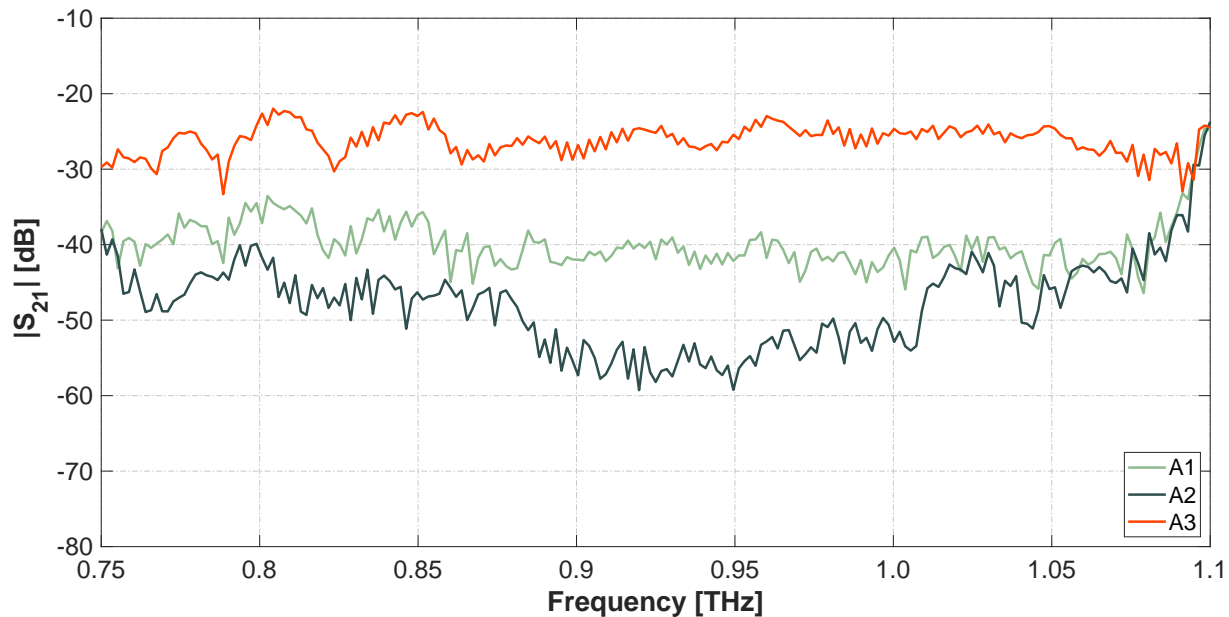


Figure 5.6: Measured S-parameter S_{21} [dB] versus frequency of indoor materials using MCK system (*Material Group: Plastic*).

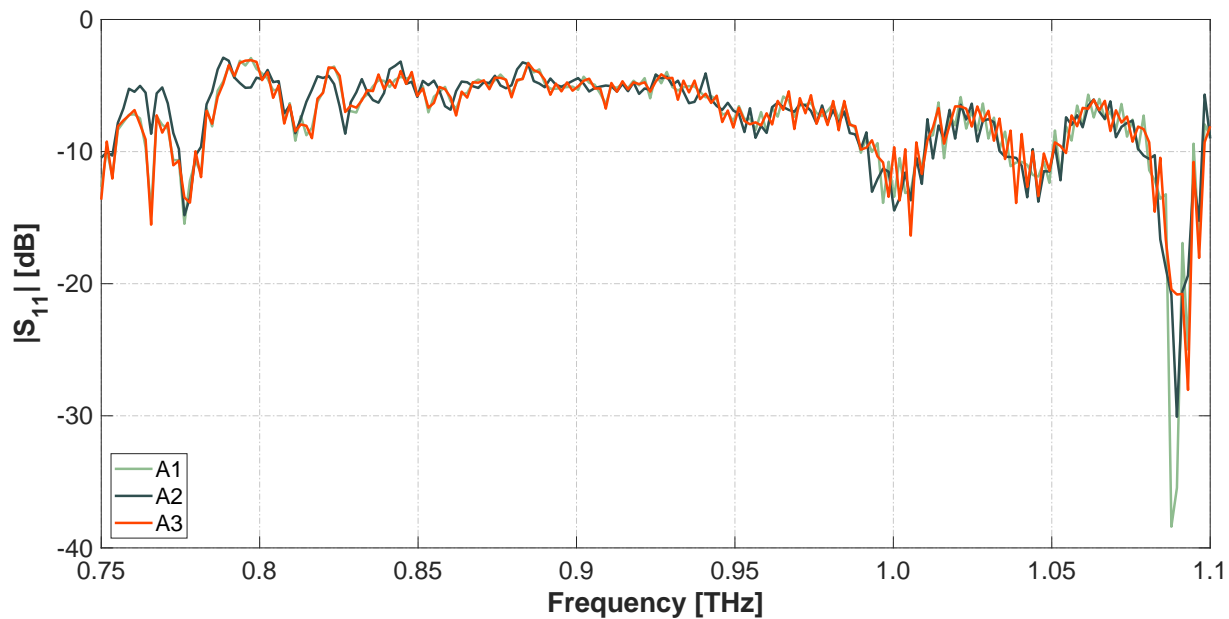


Figure 5.7: Measured S-parameter S_{11} [dB] versus frequency of indoor materials using MCK system (*Material Group: Plastic*).

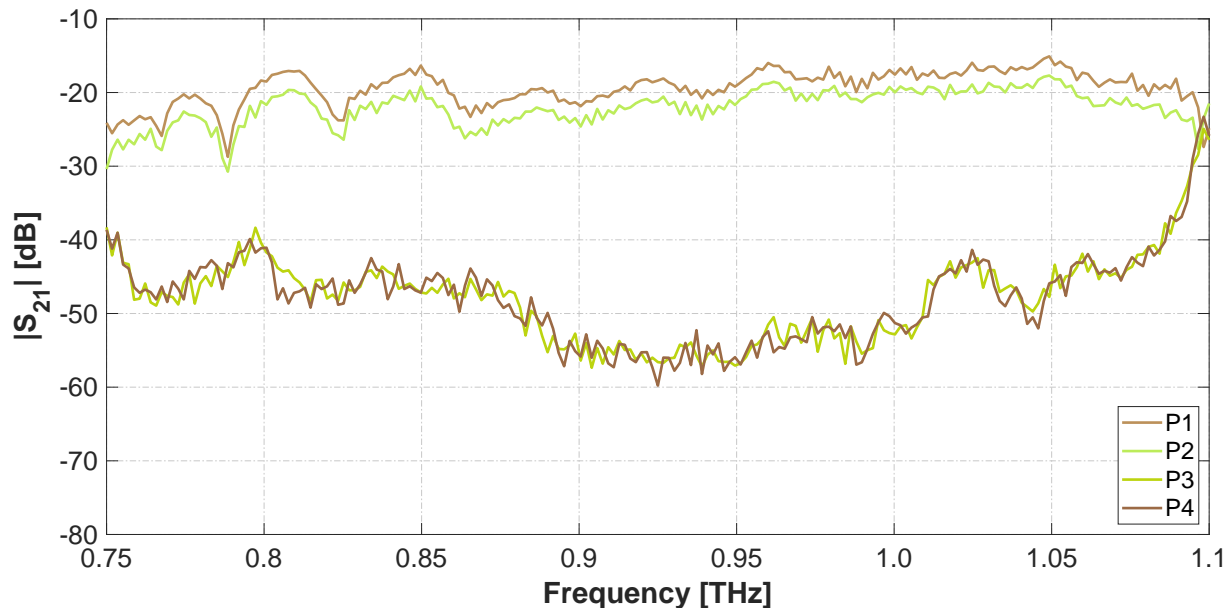


Figure 5.8: Measured S-parameter S_{21} [dB] versus frequency of indoor materials using MCK system (*Material Group: Paper*).

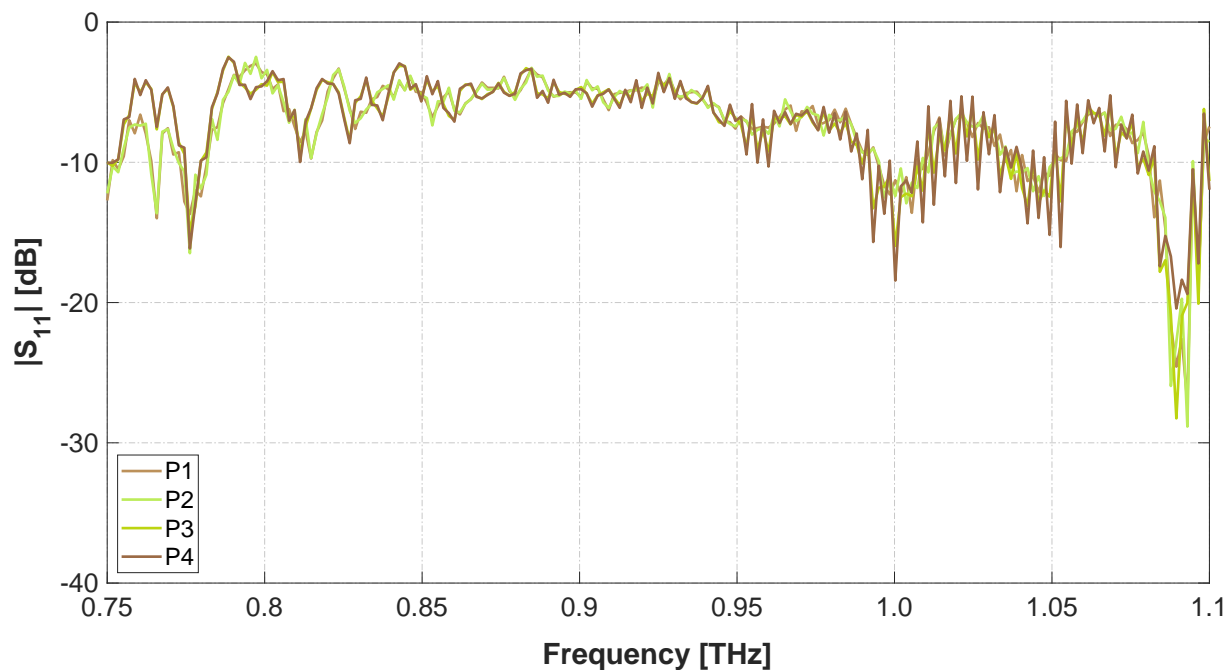


Figure 5.9: Measured S-parameter S_{11} [dB] versus frequency of indoor materials using MCK system (*Material Group: Paper*).

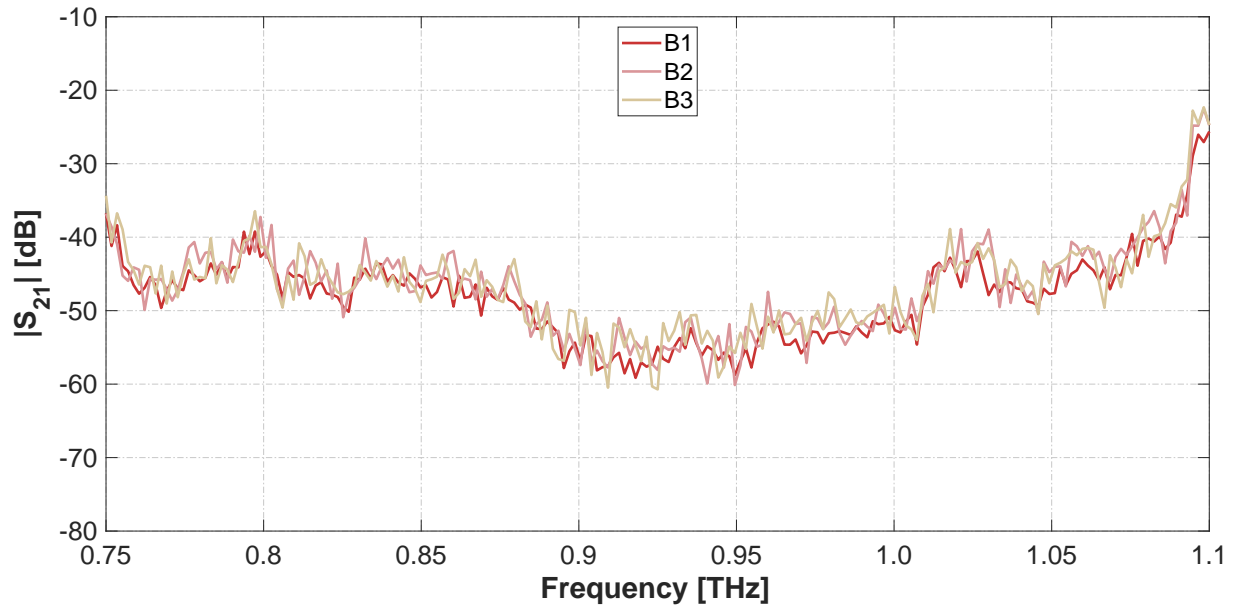


Figure 5.10: Measured S-parameter S_{21} [dB] versus frequency of indoor materials using MCK system (*Material Group: Brick*).

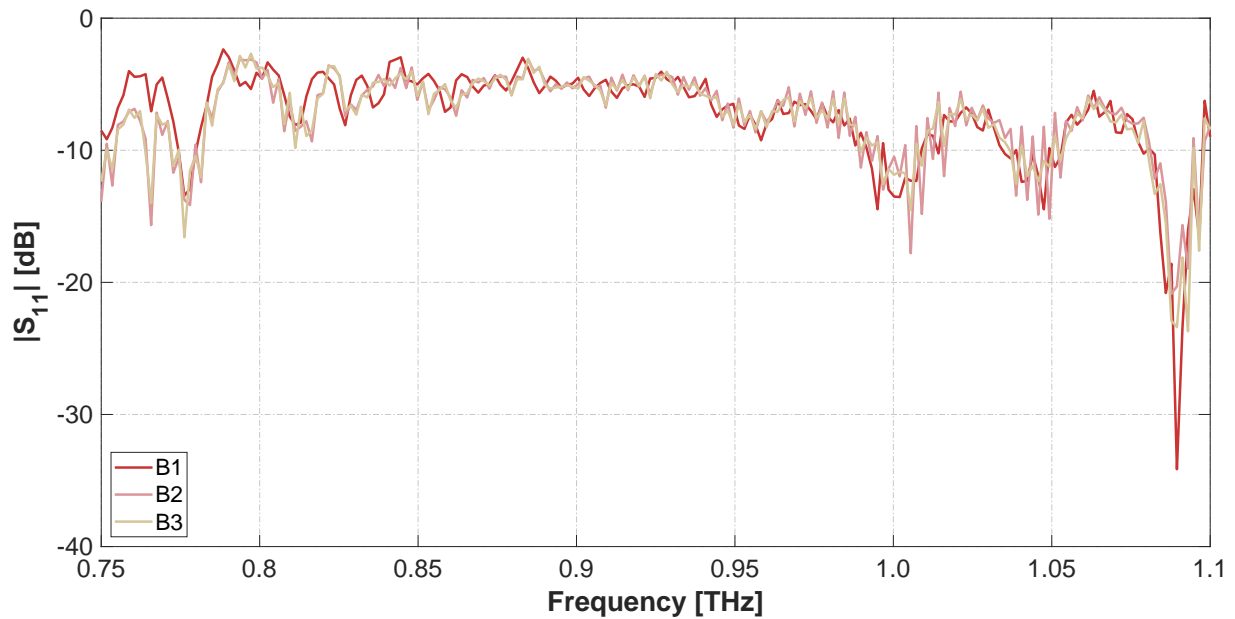


Figure 5.11: Measured S-parameter S_{11} [dB] versus frequency of indoor materials using MCK system (*Material Group: Brick*).

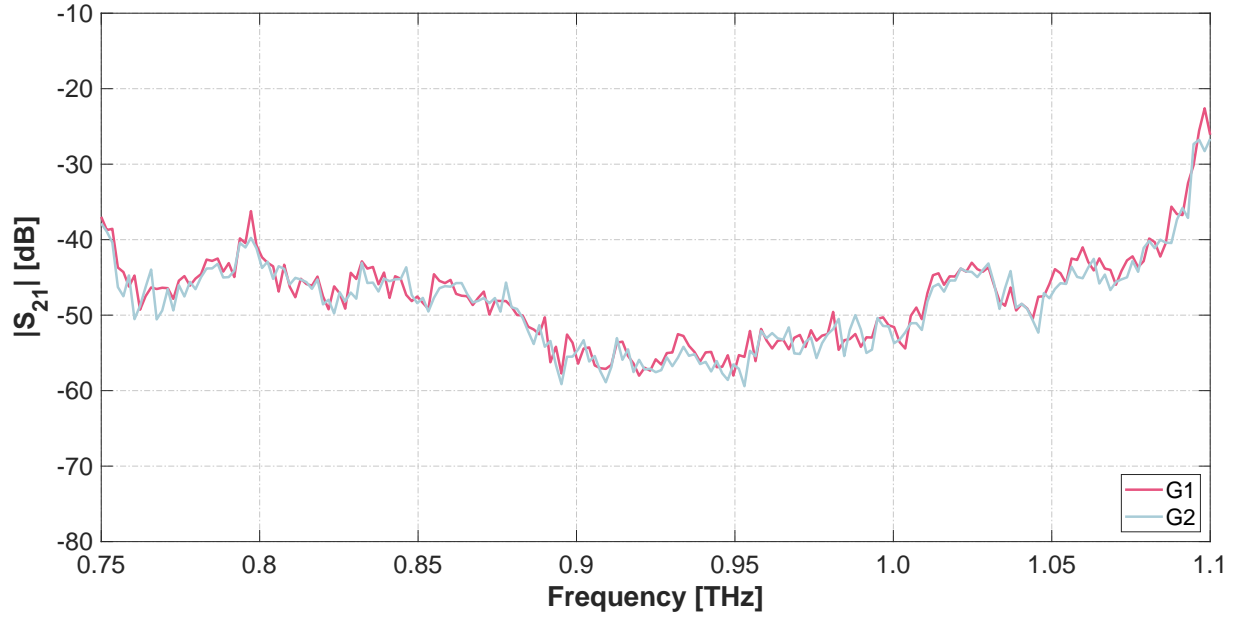


Figure 5.12: Measured S-parameter S_{21} [dB] versus frequency of indoor materials using MCK system (*Material Group: Glass*).

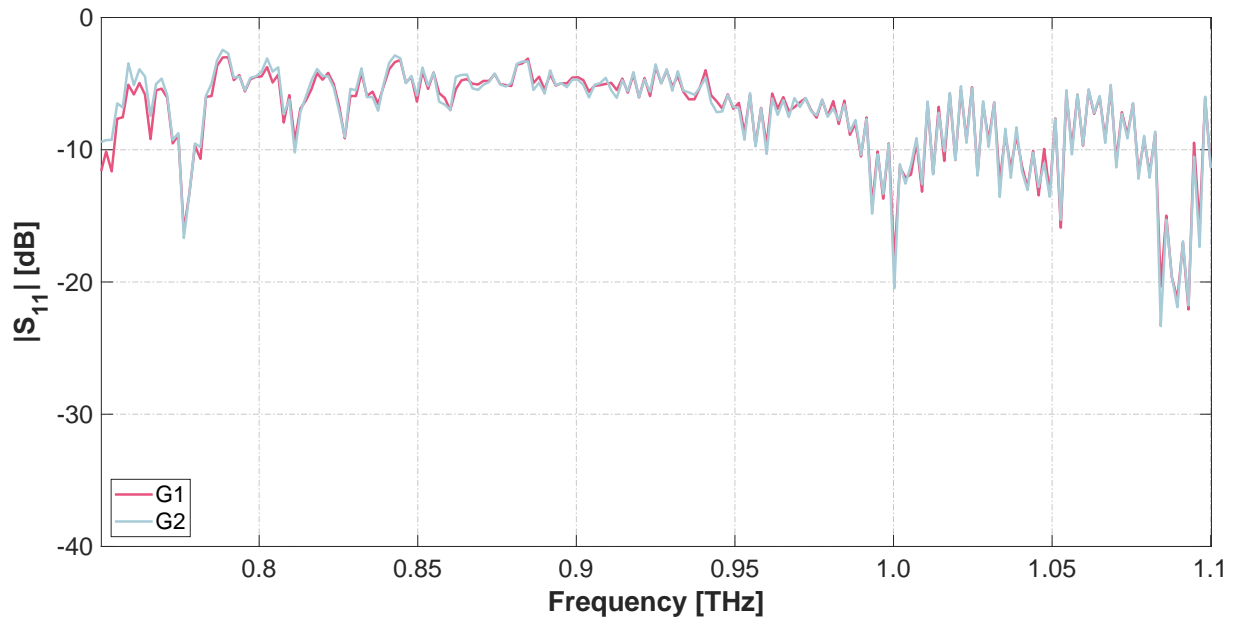


Figure 5.13: Measured S-parameter S_{11} [dB] versus frequency of indoor materials using MCK system (*Material Group: Glass*).

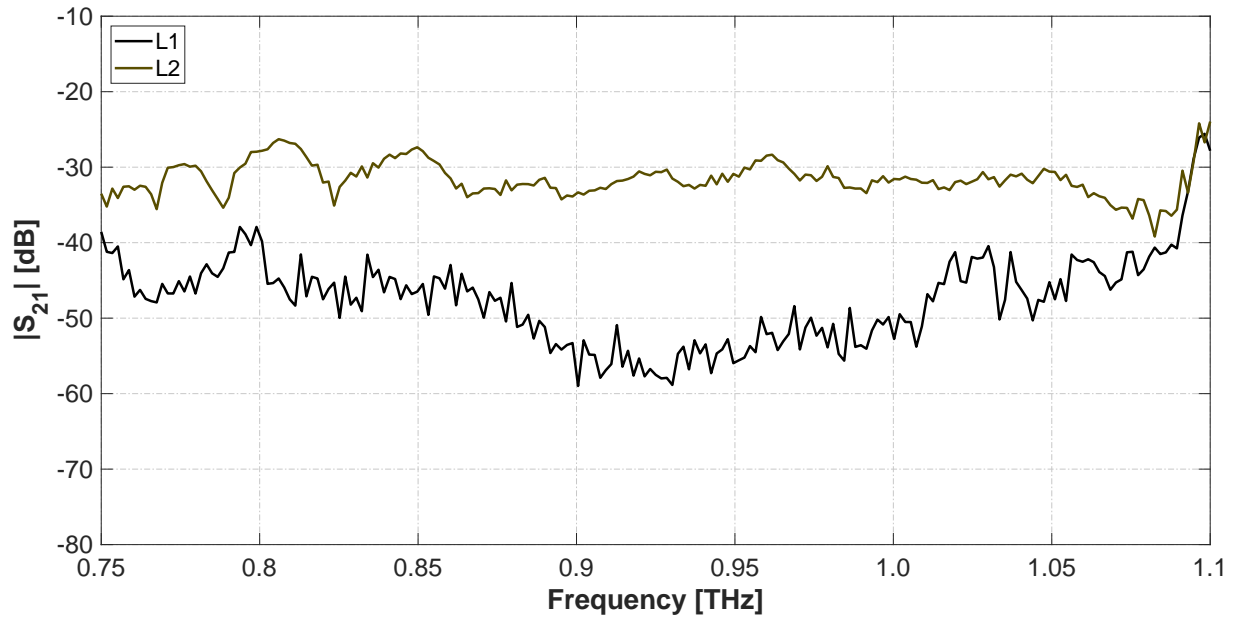


Figure 5.14: Measured S-parameter S_{21} [dB] versus frequency of indoor materials using MCK system (*Material Group: Leather*).

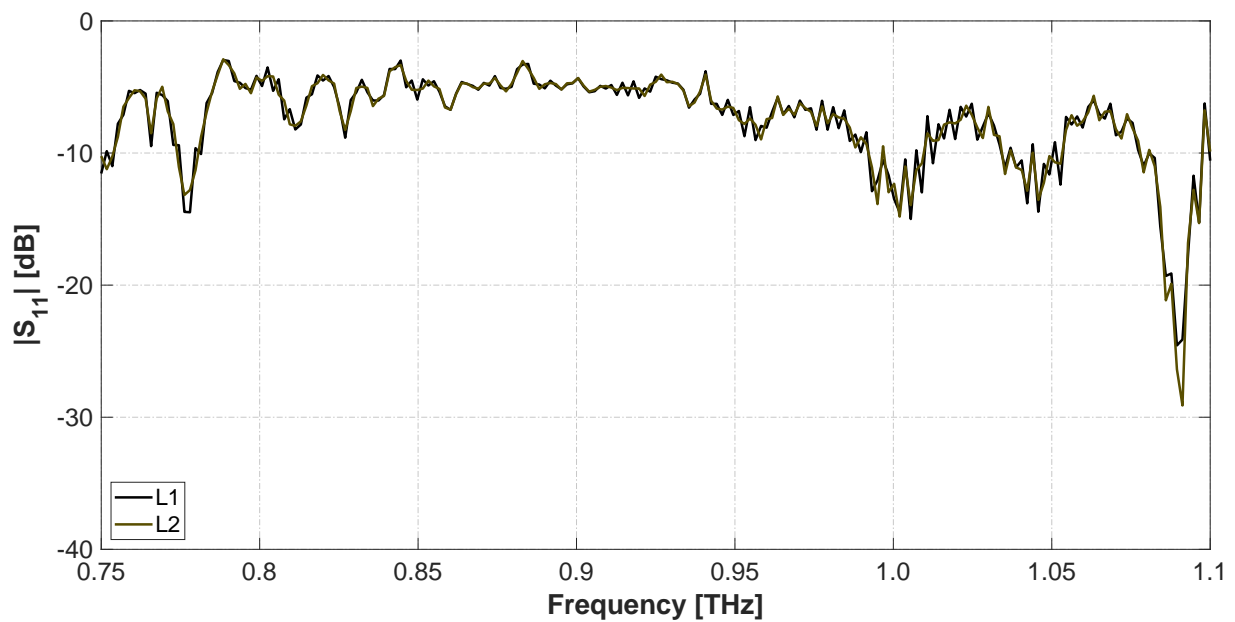


Figure 5.15: Measured S-parameter S_{11} [dB] versus frequency of indoor materials using MCK system (*Material Group: Leather*).

The fact that the values of S_{21} for all six groups are quite low indicates the high losses during transmission. These materials can thus be regarded as high-loss materials. Perhaps, the transmission attenuation, thickness of the sample and its permittivity, surface scattering, and

5.4. Description of Material Samples

absorption in the material samples result in these losses. The S_{21} values for all material groups indicate considerable variation as apparent from the illustrations. For instance, the S_{21} values for W1, W2, W3, W4, W5 and W6 at 1 THz are -52.09, -49.08, -48.51, -48.95, -48.62 and -48.43 dB, respectively. Similarly, for A1 and A3 these S_{21} values at 1 THz are -40.4 dB and -24.65 dB, respectively. Meanwhile, an 8.65 dB difference between S_{21} values for materials A1 and A3 is conspicuous in Fig. 5.6 at 750 GHz. Lastly, for B1, B2 and B3 the corresponding S_{21} values at 1 THz are -52.66, -49.6 and -46.77 dB. The recorded data reveals that the S_{21} values are not only influenced by the thickness but the texture or inner structure of any material may also impact these values. It is also noteworthy to mention here that the thickness may influence the scattering parameters but indeed causes no impact on the intrinsic properties of any material.

The variation in S_{11} also exhibits an eminent frequency dependence being a function of the thickness of the sample as well as its permittivity. However, the recurrent big dip at 1.08 THz in S_{11} for all material samples is likely attributed to absorption lines rather than errors and discrepancies in the measurement process or due to the physical behavior of the material samples [119].

Rayleigh Roughness Factor

In Fig. 5.16, the Rayleigh roughness factor ρ_{spec} illustrates the impact of scattering and surface roughness on the 6 rough material samples versus frequency as the remaining 3 material samples from Table 5.2 are smooth.

Table 5.2: Measured parameters of materials.

Mat. group	ID	$\tilde{\epsilon}_r$	$\tilde{\tilde{\epsilon}}_r$	σ_h	Thickn.
Wood	W1**	3.88	0.192	0.0468 mm ^a	7.5 mm
	W2**	3.23	0.10	0.0503 mm ^a	5.5 mm
	W3**	4.06	0.152	0.0115 mm ^b	12 mm
	W4**	2.86	0.474	0.0111 mm ^b	14 mm
	W5**	3.08	0.123	0.0122 mm ^a	10.5 mm
Plastic	A1*	2.64	0.0190	0.0000 mm	4.75 mm
	A3*	2.4	0.0340	0.0000 mm	1.2 mm
Brick	B2*	4.0	0.0820	0.0000 mm	6.5 mm
	B3**	4.20	0.10	0.0950 mm ^a	9.7 mm

*smooth surface **rough surface

^a μsurf Confocal Microscope ^bProfilometer XP-Plus 200 Stylus

The measured modified reflection coefficient is divided by the conventional reflection coefficient to obtain the Rayleigh roughness factor (cf. Eq. (2.18)). One is most likely able to extract a general rule from Eq. (2.14) that the Rayleigh roughness factor decreases with the relative increase in surface roughness, as is well evident from Fig. 5.16. Perhaps, the decrease in ρ_{spec} is only due to the impact of surface roughness as the angle of incidence is fixed, i.e., $\cos(0^\circ) = 1$, and thus causes no influence. It is evident that the material sample *W4* is amongst the least rough whereas *B3* is the most rough material. The Rayleigh roughness factor thus assorts the materials samples from most to least rough in this order, i.e., *B3*, *W1*, *W3*, *W2*, *W5* and *W4*.

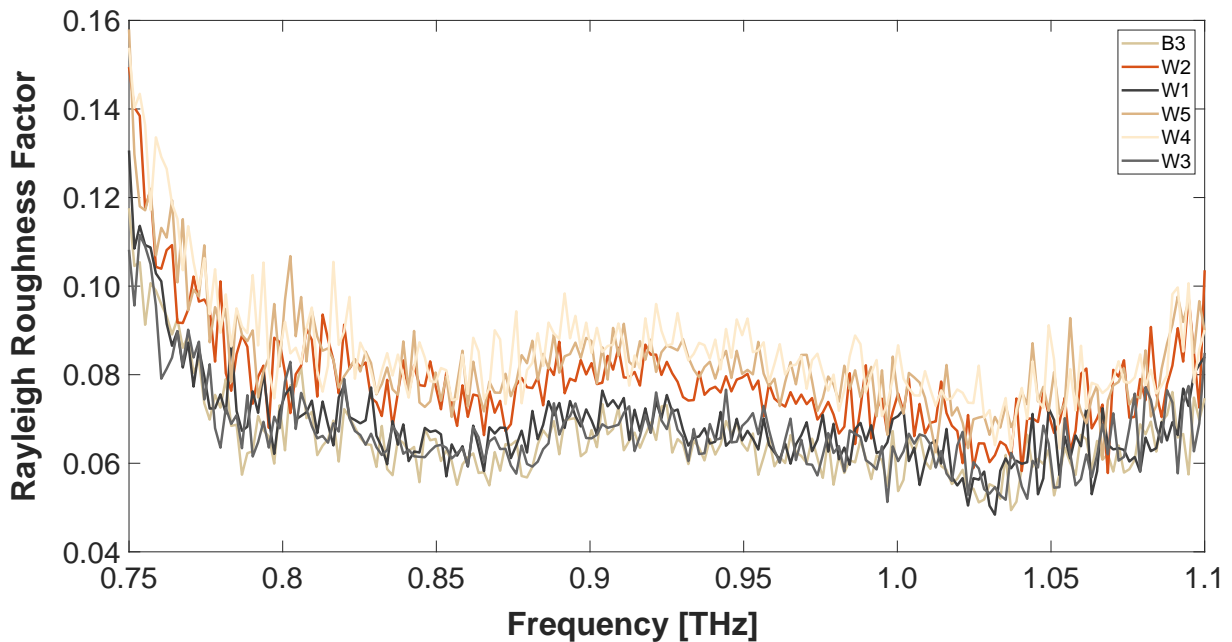


Figure 5.16: Calculated Rayleigh roughness parameter ρ_{spec} versus frequency for six rough materials at angle of incidence 0° (i.e., transmission geometry).

5.5 Propagation of EM Waves in Dielectric Materials

There are multiple reflections between material and air in the measuring system, so we cannot simply regard S_{11} as the reflection coefficient and S_{21} as the transmission coefficient of the given material. A unit amplitude wave incident on the air-sample surface in the measuring system is shown in Fig. 5.17, the relationship between the T/R coefficient of the material and the scattering parameter can be deduced from [124].

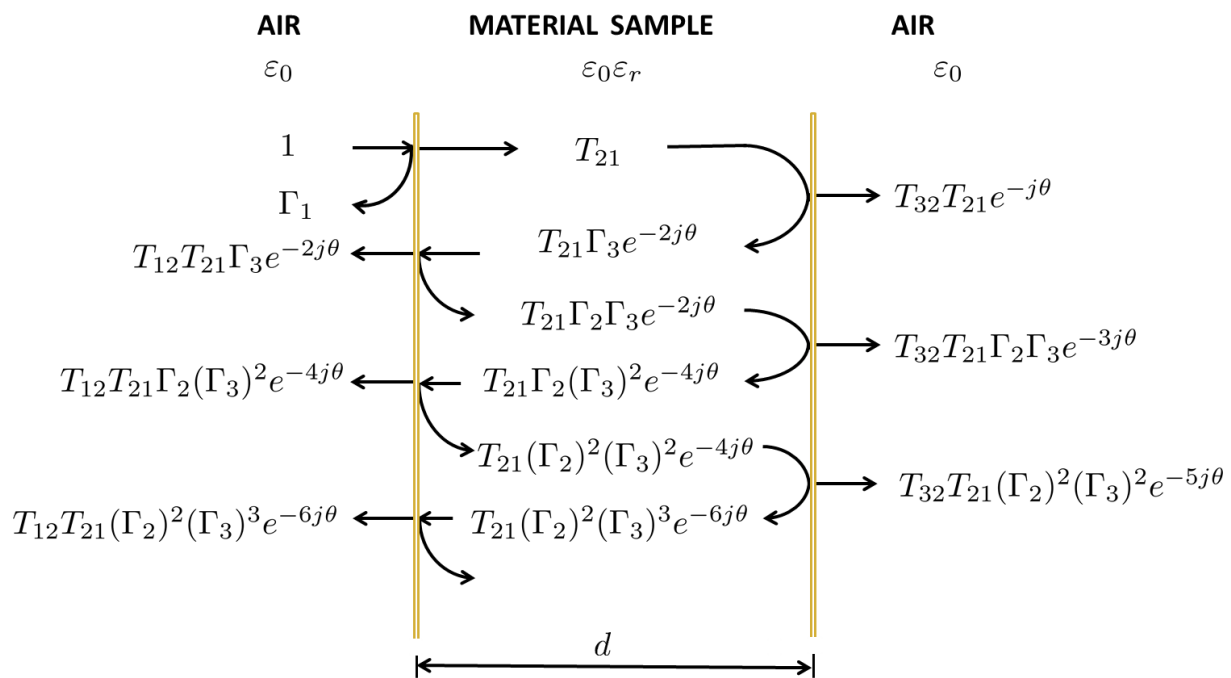


Figure 5.17: Multiple reflections at the air-sample interfaces in the system.

The total reflection coefficient Γ_{in} of this section is equal to the sum of all reflections at the first surface of the material. It can be expressed as

$$\Gamma_{in} = \Gamma_1 + T_{12}T_{21}\Gamma_3e^{-2j\theta} + T_{12}T_{21}\Gamma_2(\Gamma_3)^2e^{-4j\theta} + \dots \quad (5.9)$$

This equation can be simplified as

$$\Gamma_{in} = \Gamma_1 + T_{12}T_{21}\Gamma_3e^{-2j\theta} \sum_{n=0}^{\infty} \Gamma_2^n \Gamma_3^n e^{-2jn\theta} \quad (5.10)$$

Here, we approximate S_{11} to Γ_{in} , so the equation can be further simplified as

$$S_{11} = \Gamma_1 + \frac{T_{12}T_{21}\Gamma_3e^{-2j\theta}}{1 - \Gamma_2\Gamma_3e^{-2j\theta}} \quad (5.11)$$

Assuming that a wave is incident from first to second material, the reflection coefficient Γ_{12} at the surface between these two materials can be given as

$$\Gamma_{12} = \frac{z_2 - z_1}{z_2 + z_1} \quad (5.12)$$

where z_1 is the wave impedance in first material and z_2 is the wave impedance in second material.

From Eq. (5.12), we can get the reflection coefficients of the material as depicted in Fig. 5.17

$$\Gamma_1 = -\Gamma_2 = -\Gamma_3 \quad (5.13)$$

This means $\Gamma = \Gamma_1$. By defining

$$\begin{aligned} T_{12} &= 1 + \Gamma_2 \\ T_{21} &= 1 - \Gamma_1 \end{aligned} \quad (5.14)$$

and the transmission coefficient of the material T can then be written as

$$T = e^{-j\theta} \quad (5.15)$$

Substituting the obtained calculations from Eq. (5.13), Eq. (5.14) and Eq. (5.15) into Eq. (5.11) gives the relationship between S_{11} and T/R coefficient of the material as

$$S_{11} = \frac{\Gamma(1 - T^2)}{1 - \Gamma^2 T^2} \quad (5.16)$$

Similarly, S_{21} is calculated by summing up all the transmissions at the second surface of the material and then the relationship between S_{21} and T/R coefficient of the material is expressed as

$$S_{21} = \frac{T(1 - \Gamma^2)}{1 - \Gamma^2 T^2} \quad (5.17)$$

The Eq. (5.16) and Eq. (5.17) exhibit the relationship between the T/R coefficient of the material and the measured scattering parameters. This gives an insight into almost all of the methods utilized for extracting material properties from their corresponding scattering parameters including the NRW method and the one based on K-K relations mentioned later in this chapter.

5.6 Novel Analysis Techniques

5.6.1 Nicolson-Ross-Weir (NRW) based Methods

Basic NRW Method

The NRW method is an extraction method to retrieve the complex relative permittivity ($\epsilon_r = \tilde{\epsilon}_r - j\tilde{\epsilon}_r$) and complex relative permeability ($\mu_r = \tilde{\mu}_r - j\tilde{\mu}_r$) of the measured material by measuring

transmission and reflection [115]. In this system the transmission coefficient is expressed as

$$T = \exp(-\gamma d) \quad (5.18)$$

where d is the thickness of the material, γ is the propagation constant, defined as

$$\gamma = j\omega\sqrt{\mu_0\epsilon_0}\sqrt{\mu_r\epsilon_r - \left(\frac{\omega_c}{\omega}\right)^2} \quad (5.19)$$

ω is the angular frequency and ω_c is the angular cutoff frequency. The measuring system used in this work can be regarded as a free space measurement, the angular cutoff frequency is then $\omega_c = 0$. μ_0 is the permeability of vacuum and ϵ_0 is the permittivity of vacuum. The speed of light is $c = \frac{1}{\sqrt{\mu_0\epsilon_0}}$. These values are substituted in Eq. (5.19) to get

$$\gamma = j(\omega/c)\sqrt{\mu_r\epsilon_r} \quad (5.20)$$

The transmission coefficient can then be calculated with ϵ_r and μ_r

$$T = \exp\left[-j\left(\frac{\omega}{c}\right)\sqrt{\mu_r\epsilon_r}d\right] \quad (5.21)$$

The reflection coefficient in our measuring system can be expressed as

$$\Gamma = \frac{z - z_0}{z + z_0} \quad (5.22)$$

with

$$z = \frac{j\omega\mu_0\mu_r}{\gamma} \quad z_0 = \frac{j\omega\mu_0}{\gamma_0} \quad (5.23)$$

where z_0 is the wave impedance in the air and z is the wave impedance in the material. So Eq. (5.22) can be elaborated as

$$\Gamma = \frac{\frac{\gamma_0}{\gamma}\mu_r - 1}{\frac{\gamma_0}{\gamma}\mu_r + 1} \quad (5.24)$$

From Eq. (5.20), we get $\frac{\gamma_0}{\gamma} = \frac{1}{\sqrt{\mu_r\epsilon_r}}$. So the reflection coefficient is given as

$$\Gamma = \frac{\sqrt{\frac{\mu_r}{\epsilon_r}} - 1}{\sqrt{\frac{\mu_r}{\epsilon_r}} + 1} \quad (5.25)$$

In the NRW algorithm, based on Eq. (5.16) and Eq. (5.17) mentioned in the last section, let us assume

$$\begin{aligned} V_1 &= S_{21} + S_{11} \\ V_2 &= S_{21} - S_{11} \end{aligned} \quad (5.26)$$

and

$$K = \frac{1 - V_1 V_2}{V_1 V_2} = \frac{S_{11}^2 - S_{21}^2 + 1}{2S_{11}} \quad (5.27)$$

The reflection coefficient can then be expressed in terms of scattering parameters as

$$\Gamma = K \pm \sqrt{K^2 - 1} \quad (5.28)$$

Depending on the $|\Gamma| \leq 1$, the value of Γ is either positive or negative. The transmission coefficient is given by

$$T = \frac{V_1 - \Gamma}{1 - V_1 \Gamma} = \frac{S_{11} + S_{21} - \Gamma}{1 - (S_{11} + S_{21})\Gamma} \quad (5.29)$$

The Eq. (5.28) and Eq. (5.29) enable one to extract the reflection coefficient Γ and transmission coefficient T from the scattering parameters.

The values of Γ and T are thus obtained and their relationship with ϵ_r and μ_r is also been retrieved. The above information is employed to calculate μ_r and ϵ_r . Hence, from the Eq. (5.25) we can get

$$\frac{\mu_r}{\epsilon_r} = \left(\frac{1 + \Gamma}{1 - \Gamma}\right)^2 = c_1 \quad (5.30)$$

and from the Eq. (5.21) we obtain

$$\mu_r \epsilon_r = -\left[\frac{c}{\omega d} \ln\left(\frac{1}{T}\right)\right]^2 = c_2 \quad (5.31)$$

Thus,

$$\mu_r = \sqrt{c_1 c_2} \quad (5.32)$$

$$\epsilon_r = \sqrt{\frac{c_2}{c_1}} \quad (5.33)$$

The refractive index is then given by

$$n = \sqrt{\epsilon_r \mu_r} \quad (5.34)$$

Theoretically, the relative complex permittivity ϵ_r and relative complex permeability μ_r can be calculated eventually from S_{11} and S_{21} . The flowchart of the basic NRW method is shown in Fig. 5.18.

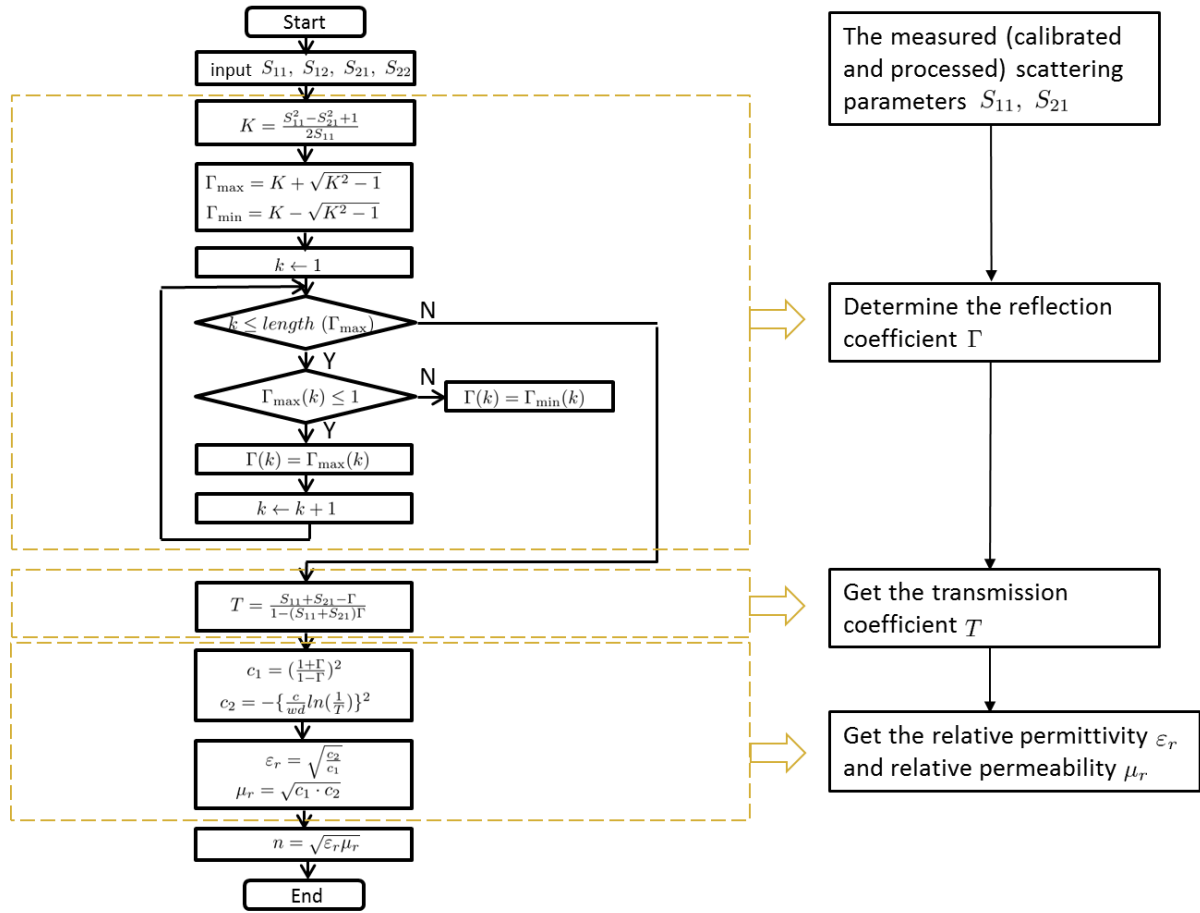


Figure 5.18: Nicolson-Ross-Weir method for calculating dielectric permittivity.

The NRW method is non-iterative, simple in calculation and high in precision. However, there are some problems in the basic NRW method. The *first one* is the existence of “thickness resonance”. It means, in the no-loss or low-loss materials, when some frequencies satisfy $d = m \frac{\lambda_g}{2}$, $m = 1, 2, 3, \dots$, where λ_g is the wavelength within the sample, there will be then $T = \exp[-j(\frac{\omega}{c})\sqrt{\mu_r \epsilon_r}d] \rightarrow \pm 1$. So the S_{11} determined by Eq. (5.16) is close to 0, $|S_{11}| \rightarrow 0$, and similarly $|S_{21}| \rightarrow 1$ [125]. The abnormal phenomenon at these frequency points also influences the results of ϵ_r and μ_r . But the thickness resonances do not occur for higher loss materials as is the case in our work, depicted in Fig. 5.19

In order to reduce this error for the low-loss materials, one may generally control the thickness of the sample to be less than $\frac{\lambda_g}{2}$. The best thickness of a sample is $\frac{\lambda_g}{4}$ with minimum error. However, at higher frequencies, for example, 0.75 ~ 1.1 THz as in this work, the half wavelength in the sample is less than 1 mm. So it is almost impossible to get $d < \frac{\lambda_g}{2}$, thus at high frequencies the “thickness resonance” is hard to avoid for low-loss materials. Moreover,

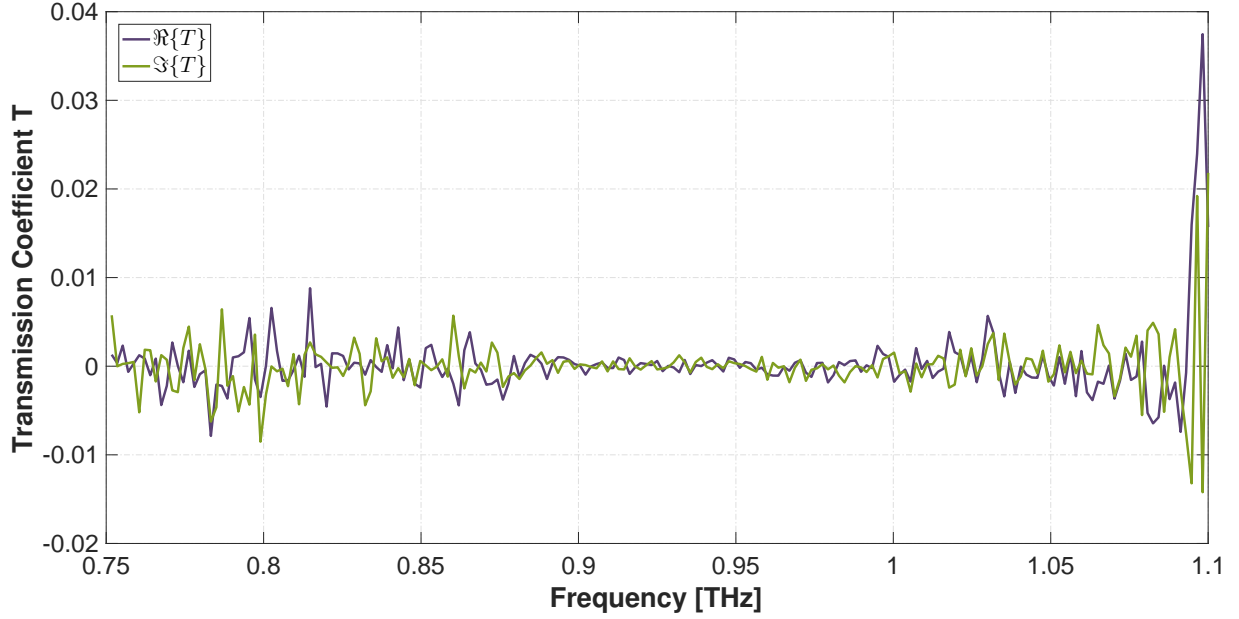


Figure 5.19: Transmission coefficient T

even if the thickness of the material can be limited for lower frequencies, a very thin thickness will affect the accuracy of the measurement. This problem seriously restricts the use of NRW method.

The *second problem* is the multi-value of $\ln(\frac{1}{T})$. $\frac{1}{T}$ is constant which has a unique solution. But $\ln(\frac{1}{T})$ has many values from the complex number $\frac{1}{T}$

$$\ln\left(\frac{1}{T}\right) = \ln\left|\frac{1}{T}\right| + j[\arg\left(\frac{1}{T}\right) + 2m\pi], m = 0, 1, 2, \dots \quad (5.35)$$

Here, $\arg(\frac{1}{T})$ represents calculating the argument of $\frac{1}{T}$ in the range $[-\pi, \pi]$. We can see that the imaginary part of $\ln(\frac{1}{T})$ is multi-valued and each value differs by $2m\pi$. In the mathematical algorithm, one generally takes the solution of the whole imaginary part of $\ln(\frac{1}{T})$ in the range of $[-\pi, \pi]$, which may lead to an error in the result.

Defining the value of m as

$$m = \text{int}\left(\frac{d}{\lambda_g}\right) \quad (5.36)$$

Here, *int* means integer. In the common NRW method, the need is for $d < \frac{\lambda_g}{2}$, at least at the start frequency point $d < \frac{\lambda_g}{2}$ (a stepwise method mentioned below is applied to this situation), by default $m = 0$ and the imaginary part of $\ln(\frac{1}{T})$ in the range $[-\pi, \pi]$ is proper.

However, for high frequencies such as THz the situation becomes more complex. In this

case, d is required to be quite greater than λ_g , such that $m \neq 0$ is definite. When using the basic NRW method, it may result in a huge error, and the result is even nonphysical as presented in Fig. 5.20. Due to the unknown material properties, λ_g is hard to define, hence this makes the evaluation of m challenging as well. Later in this section, an NRW method based on group delay unfolds the proper way to obtain m .

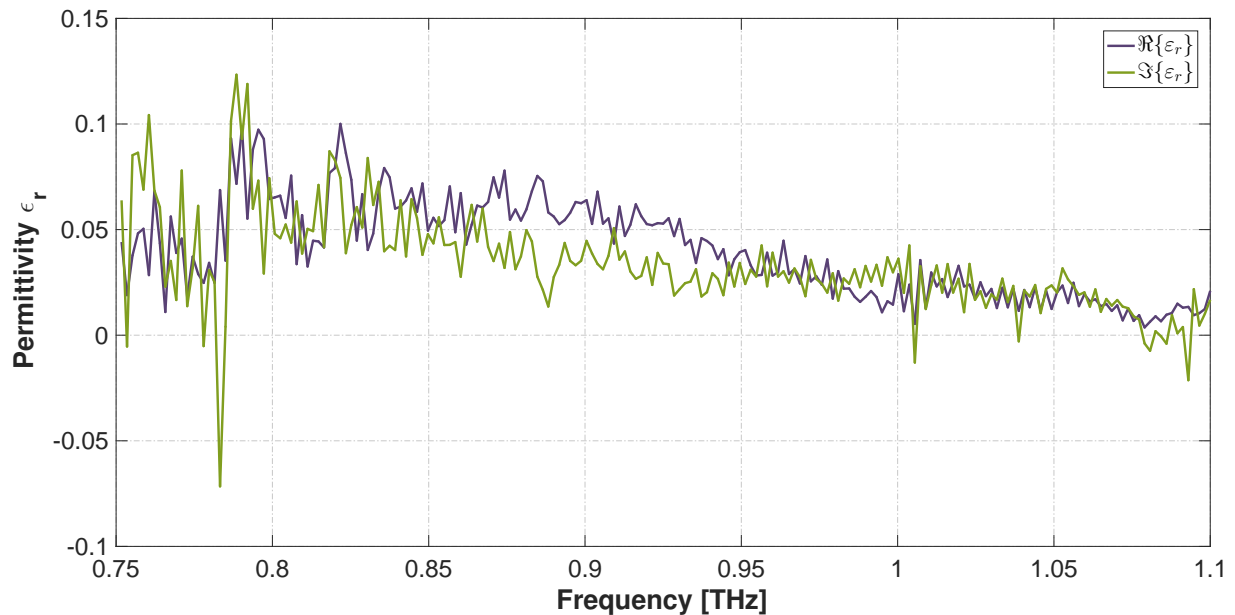


Figure 5.20: Relative permittivity base on basic NRW method

Stepwise NRW Method

In Eq. (5.35), we consider the imaginary part of $\ln(\frac{1}{T})$ ranging from $-\pi$ to $+\pi$ for the basic NRW method, if it exceeds this range, the results still jump back to the range $[-\pi, +\pi]$, i.e., randomized results due to the phase ambiguity. Hypothetically, we consider N frequency points, $f_1, f_2, f_3, \dots, f_N$, with the corresponding transmission coefficients $T_1, T_2, T_3, \dots, T_N$. By using the constraint of the changes between the imaginary part of $\ln(\frac{1}{T_{i-1}})$ and $\ln(\frac{1}{T_i})$ ($2 \leq i \leq N$), the problem of multi-values can be tackled [126].

$$\phi_i = \phi_{i-1} + \arg\left(\frac{\frac{1}{T_i}}{\frac{1}{T_{i-1}}}\right) = \phi_{i-1} + \arg\left(\frac{T_{i-1}}{T_i}\right) \quad (5.37)$$

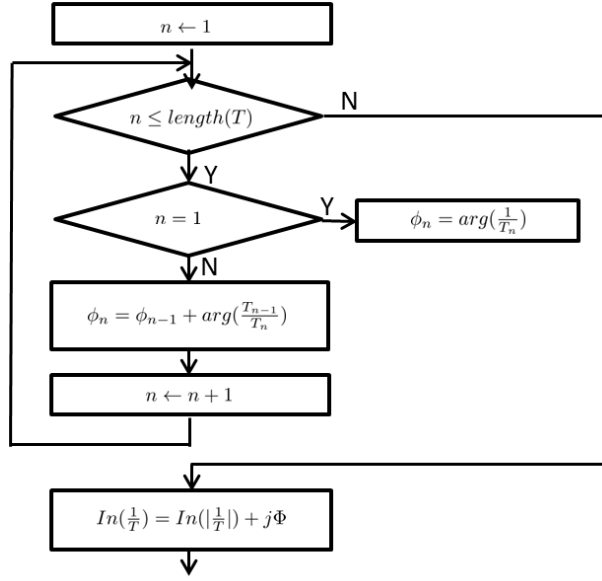


Figure 5.21: The flowchart of operation process for $\ln\frac{1}{T}$

where ϕ_i is the imaginary part of $\ln(\frac{1}{T_i})$. Finally, ϕ_N can be written as

$$\begin{aligned}
 \phi_N &= \phi_1 + \sum_{i=1}^N \arg\left(\frac{\frac{1}{T_i}}{\frac{1}{T_{i-1}}}\right) \\
 &= \phi_1 + \sum_{i=1}^N \arg\left(\frac{T_{i-1}}{T_i}\right)
 \end{aligned} \tag{5.38}$$

In the frequency band, Eq. (5.37) ascertains $\Delta\phi = \phi_i - \phi_{i-1} \leq \pi$, which determines the unique solution of ϕ_i , so that there is no ambiguity of $\ln(\frac{1}{T})$. The only problem is to determine the value of ϕ_1 , all other values of ϕ at the frequency points afterwards can be obtained by the previous values. In the common stepwise NRW method, ϕ_1 is in the range from $-\pi$ to $+\pi$ by default. After getting the result of ϕ , $\ln(\frac{1}{T})$ without ambiguity can be calculated from the following equation

$$\ln\left(\frac{1}{T}\right) = \ln\left|\frac{1}{T}\right| + j\phi \tag{5.39}$$

The flowchart for the evaluation steps of operation process for $\ln\frac{1}{T}$ based on the stepwise NRW method is shown in Fig. 5.21. The other part of the stepwise NRW method is complete in harmony with the basic NRW method.

The prerequisite of the stepwise NRW method is that the start frequency is low, and it

satisfies $d < \frac{\lambda_g}{2}$, in order to guarantee $m_1 = 0$. With $\lambda_g = \frac{v_g}{f}$ and $v_g = \frac{c}{\sqrt{\epsilon_r \mu_r}}$ (v_g is the velocity in the material), the deterministic formula of start frequency is given as

$$f_1 < \frac{c}{2d\sqrt{\epsilon_r \mu_r}} \quad (5.40)$$

If the starting frequency f_1 satisfies this formula, then $m_1 = 0$ and ϕ_1 is directly defined in the range of $[-\pi, +\pi]$, therefore, we can just use the stepwise NRW method to get the result.

The stepwise NRW method is an improvisation of the basic NRW method, because in most cases, it is unrealistic that all the frequencies on the frequency band satisfy $d < \frac{\lambda_g}{2}$, which leads to the fact that the results of the basic NRW method are often inaccurate. In comparison, the stepwise NRW method only limits the start frequency, but does not limit the other frequencies, even if the following frequencies become higher and higher, resulting in $m \neq 0$, if ϕ is out of the range $[-\pi, \pi]$, the stepwise NRW method can still work, which offsets the error caused by multi-value.

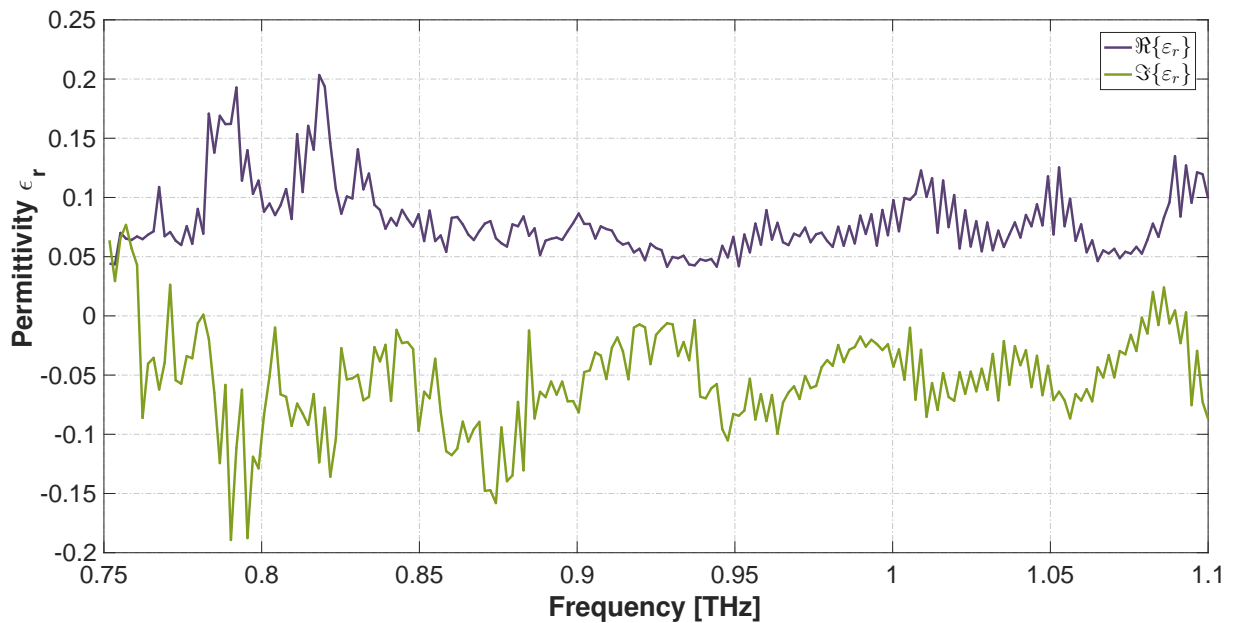


Figure 5.22: Relative permittivity based on a stepwise NRW method

From Fig. 5.22, it is evident that the relative permittivity obtained based on the stepwise NRW method is more smooth and steady than the one obtained from the basic NRW method. But at higher frequencies such as THz as depicted in the figure, the result is still nonphysical. The main reason being is the start frequency in this work is 0.75 THz, thus making it impossible to achieve $m_1 = 0$, hence we still need to evaluate m_1 to get the ϕ_1 . In contrast the advantage is

that we need the m merely at the start frequency (m_1), instead of calculating the values of m for each of the frequency points.

Basic NRW Method based on Group Delay

For NRW method at THz frequencies, the key problem is to determine the value of m in order to overcome the issue of multi-values. If the cutoff frequency of the waveguide (f_c) is known for the transmission/reflection line method, we can get λ_g through the formula $\lambda_g = \frac{\lambda_0}{\sqrt{1 - (\frac{\lambda_0}{\lambda_c})^2}}$, and then m is obtained from $m = \text{int}(\frac{d}{\lambda_g})$. For the free method the value of m can be evaluated by comparing the calculated group delay with the measured group delay.

The group delay directly obtained by the measurement is defined as

$$\tau_{meas} = -\frac{1}{2\pi} \frac{d\varphi}{df} \quad (5.41)$$

where φ is the phase of the transmission coefficient T .

The calculated group delay is

$$\tau_{calc} = d \frac{d}{df} \sqrt{\frac{\epsilon_r \mu_r}{\lambda_0^2} - \frac{1}{\lambda_c^2}} \quad (5.42)$$

In this work it can be rewritten as

$$\tau_{calc} = d \frac{d}{df} \sqrt{\frac{\epsilon_r \mu_r}{\lambda_0^2}} \quad (5.43)$$

Firstly, we should calculate ϵ_r and μ_r when m takes a series of values based on the basic NRW method. Secondly, we can get the τ_{calc} at each frequency point from Eq. (5.43), where τ_{calc} is a series of values for each frequency point corresponding to the value of m . Finally, the τ_{calc} and the τ_{meas} are compared for each frequency point to determine the proper m . When $\tau_{calc}(m = k) - \tau_{meas} \simeq 0$, at this frequency the most suitable m value is $m = k$.

A prerequisite for this method is that the spacing between adjacent frequency points is small enough so that the phase of T changes less than 360° from this frequency point to the adjacent one. Also because of the small frequency spacing, the change of ϵ_r and μ_r between adjacent frequencies is so small that it can be neglected [127].

In Fig. 5.23, our results reveal an undesirable phenomenon where m takes a different range and the optimal solution of m changes, thus changing the ϵ_r . This maybe due to the excessive

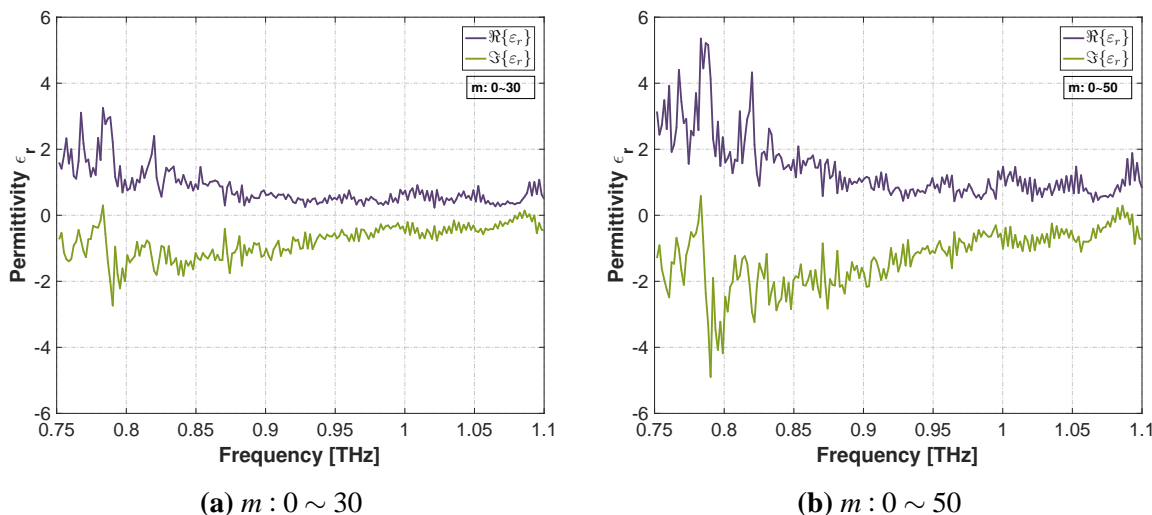


Figure 5.23: Relative permittivity for the different range of $m : 0 \sim 30$ and $m : 0 \sim 50$.

spacing of adjacent frequencies, $\Delta f = 1.75$ GHz in our work, giving errors in the results. This problem may be avoided by selecting more frequency points in this frequency band, but for the measured data another method is introduced to overcome this limitation, which is an extraction elaborated in K-K relations later in Sec. 5.6.2.

Stepwise NRW Method based on Group Delay

In the NRW method based only on group delay, the loop calculation in the range of m is to be done at each frequency point, then this calculation cycle from the first frequency to the last one is repeated, which requires a lot of operational steps. But if we combine the group delay and stepwise NRW method, this greatly reduces the amount of computation. One can only use the group delay to estimate the proper value of m at the first frequency so that the value of $\ln(\frac{1}{T})$ at the first frequency can be obtained, then the rest of the calculation is performed by the stepwise NRW method.

Table 5.3: Elapsed times of the programming.

The range of m	Group delay (seconds)	Combination (seconds)
0 ~ 30	4.04	0.20
0 ~ 50	6.62	0.56

The NRW method based on group delay only and the other one that based on a combination of group delay and stepwise yield similar results as shown in Fig. 5.24, but the elapsed time of the combination is comparatively more faster and less, Table 5.3 shows the different elapsed times.

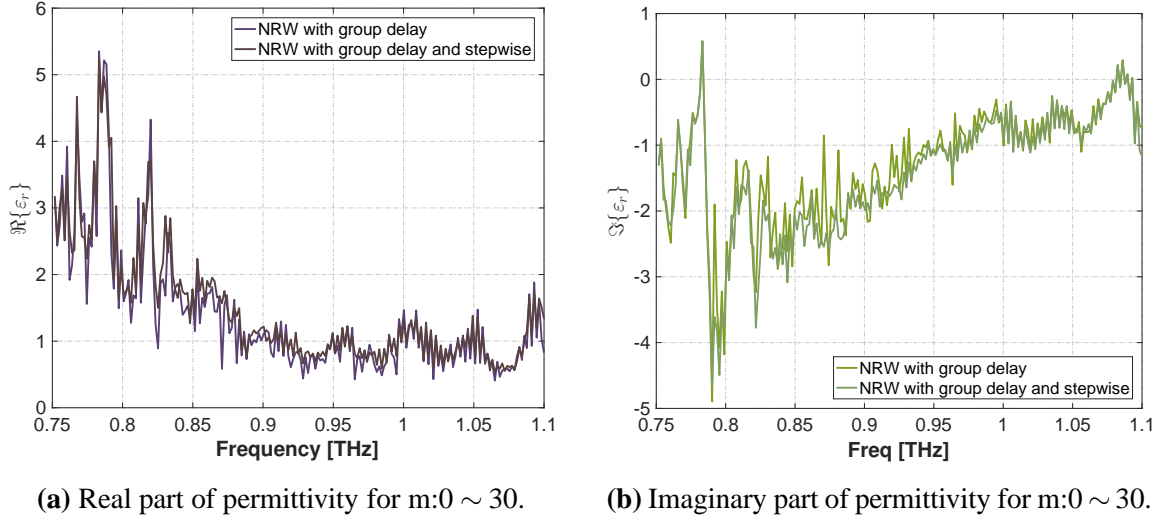


Figure 5.24: Comparison of relative permittivity.

5.6.2 Kramers-Kronig (K-K) Relations based Method

Kramers-Kronig Relations

K-K relation is essentially a special case of the Hilbert transform, it describes the relationship between the real and imaginary parts of the response function. Hilbert transform can be regarded as a convolution of the input signal $u(t)$ with the signal $\frac{1}{\pi t}$, which means extending the real-valued signal to the complex plane as

$$H[u(t)] = u(t) \otimes \left(\frac{1}{\pi t}\right) = \frac{1}{\pi} P \int_{-\infty}^{\infty} \frac{u(\tau)}{t - \tau} d\tau \quad (5.44)$$

where P denotes the cauchy principal value integral. If the system has causality, that is, when $t < 0$, $u(t) = 0$, the real part and imaginary parts of the response function $u(w)$ are not independent, which are further from a pair of Hilbert transform pairs. The Hilbert transform can evolve into K-K relations [128], it can then be written as

$$\begin{aligned} Re\{u(w)\} &= \frac{1}{\pi} P \int_{-\infty}^{\infty} \frac{Im\{u(\omega')\}}{\omega' - \omega} d\omega' \\ Im\{u(w)\} &= \frac{1}{\pi} P \int_{-\infty}^{\infty} \frac{Re\{u(\omega')\}}{\omega' - \omega} d\omega' \end{aligned} \quad (5.45)$$

Considering $u(t)$ is the real-valued function, we get

$$u(-\omega) = u^*(\omega) \quad (5.46)$$

where * means the complex conjugate. So $Re\{u(\omega)\}$ is an even function, $Im\{u(\omega)\}$ is an odd function and both are rewritten as

$$\begin{aligned} Re\{u(\omega)\} &= Re\{u(-\omega)\} \\ Im\{u(\omega)\} &= -Im\{u(-\omega)\} \end{aligned} \quad (5.47)$$

Substituting the above formula into Eq. (5.45) gives

$$Re\{u(\omega)\} = \frac{2}{\pi} P \int_0^{\infty} \frac{\omega' Im\{u(\omega')\}}{\omega' - \omega} d\omega' \quad (5.48)$$

$$Im\{u(\omega)\} = -\frac{2\omega}{\pi} P \int_0^{\infty} \frac{Re\{u(\omega')\}}{\omega' - \omega} d\omega' \quad (5.49)$$

In the optical response function determined by the causal relationship, its real and imaginary parts are not independent of each other. For example, the complex refractive index ($n = \eta + j\kappa$) describes the interaction between waves and materials from a macroscopic viewpoint. The real part η is related to the phase velocity of the wave in the medium ($\eta = \frac{c}{v_g}$), and the imaginary part κ is generally positive, representing the attenuation of the wave in that medium. When $\omega \rightarrow \infty$, $n(\omega) \rightarrow 1$, then the K-K relations connecting the real and imaginary parts of the refractive index can be written as:

$$\eta(\omega) - 1 = \frac{2}{\pi} P \int_0^{\infty} \frac{\omega' \kappa(\omega')}{\omega' - \omega} d\omega' \quad (5.50)$$

$$\kappa(\omega) = -\frac{2\omega}{\pi} P \int_0^{\infty} \frac{\eta(\omega')}{\omega' - \omega} d\omega' \quad (5.51)$$

It can be seen from the Eq. (5.50) and Eq. (5.51) that if either one of the real or the imaginary part is determined, then the other one is also calculated. We can use this to solve the multi-value problem in the extraction of the material properties from scattering parameters.

The Method based on Kramers-Kronig Relations

In Fig. 5.25, the flowchart of the K-K relation based method is depicted. The S-parameters are previously derived in Eq. (5.16) and Eq. (5.17). Now, after substituting the value of $T = e^{+jk_0nd}$ derived from Eq. (5.21) by [115, 130], the equation can be rewritten for the above S-parameters as

$$S_{11} = \frac{\Gamma(1 - T^2)}{1 - \Gamma^2 T^2} = \frac{\Gamma(1 - e^{+2jk_0nd})}{1 - \Gamma^2 e^{+2jk_0nd}} \quad (5.52)$$

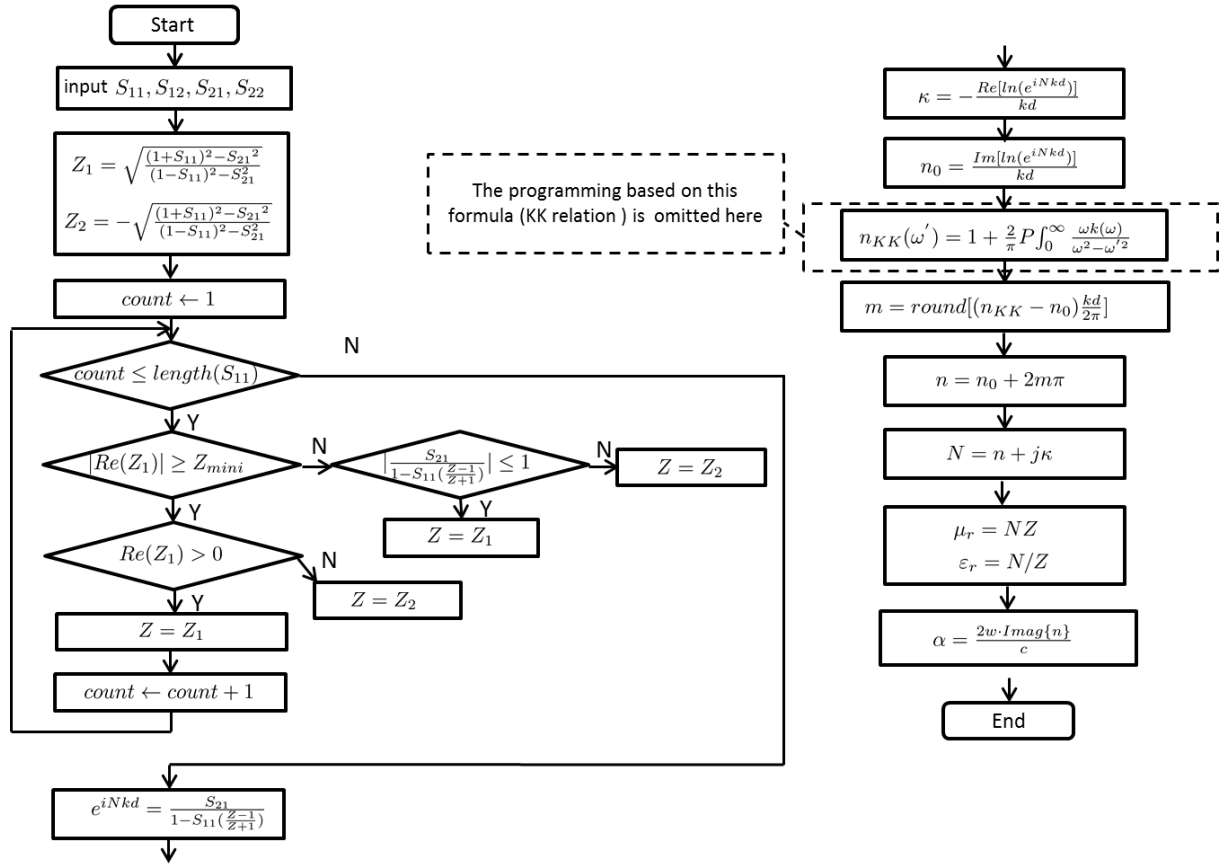


Figure 5.25: Flowchart of method based on K-K relations.

$$S_{21} = \frac{T(1 - \Gamma^2)}{1 - \Gamma^2 T^2} = \frac{e^{+jk_0nd}(1 - \Gamma^2)}{1 - \Gamma^2 e^{+2jk_0nd}} \quad (5.53)$$

The reflection coefficient of the material specimen is

$$\Gamma = \frac{z - z_0}{z + z_0} = \frac{Z - 1}{Z + 1} \quad (5.54)$$

Here, Z is the normalized impedance. From the above equations, we obtain

$$Z = \sqrt{\frac{(1 + S_{11})^2 - S_{21}^2}{(1 - S_{11})^2 - S_{21}^2}} \quad (5.55)$$

$$T = \frac{S_{21}}{1 - S_{11}\Gamma} \quad (5.56)$$

Let us assume working with passive materials, there is no gain in the material, so $Re(Z) \geq 0$, $Im(n) \geq 0$, also the $|T| \leq 1$, then the value of Z can be derived. After determining this, we get

the value of Γ from Eq. (5.54), and the value of T from Eq. (5.56). The refractive index n can then be expressed with T as

$$\begin{aligned} n &= \frac{1}{k_0 d} \{Im[\ln(T)] + 2m\pi - jRe[\ln(T)]\} \\ &= \frac{1}{k_0 d} \{Im[\ln(e^{jk_0 nd})] + 2m\pi - jRe[\ln(e^{jk_0 nd})]\} \end{aligned} \quad (5.57)$$

where m is some integer. T is expressed as

$$T = e^{jk_0 nd} \quad (5.58)$$

Now, the real and imaginary parts of the refractive index are expressed separately

$$\eta = Re(n) = \frac{Im[\ln(e^{jk_0 nd})]}{k_0 d} + \frac{2m\pi}{k_0 d} = n_0 + \frac{2m\pi}{k_0 d} \quad (5.59)$$

$$\kappa = Im(n) = -\frac{Re[\ln(e^{jk_0 nd})]}{k_0 d} \quad (5.60)$$

The above expression reveals that the imaginary part of the refractive index κ is well-determined, but the real part of the refractive index η is multi-valued. Therefore, by utilizing the K-K relationships to evaluate the value of η by using κ from the Eq. (5.50) is given as

$$\eta_{kk}(w') = 1 + \frac{2}{\pi} P \int_0^\infty \frac{w\kappa(w)}{w^2 - w'^2} dw \quad (5.61)$$

Now we get an estimated value η_{kk} of η by using the K-K relations, we then compare η_{kk} and η_0 to find the value of m .

$$m = Round\left[(\eta_{kk} - \eta_0) \frac{k_0 d}{2\pi}\right] \quad (5.62)$$

where $Round()$ means taking the nearest integer. From Eq. (5.57) the refractive index n is finally determined as

$$\begin{aligned} n &= \sqrt{\epsilon_r \mu_r} \\ Z &= \sqrt{\frac{\mu_r}{\epsilon_r}} \end{aligned} \quad (5.63)$$

Accordingly, the relative permittivity and relative permeability are derived as

$$\epsilon_r = \frac{n}{Z} \quad (5.64)$$

$$\mu_r = nZ \quad (5.65)$$

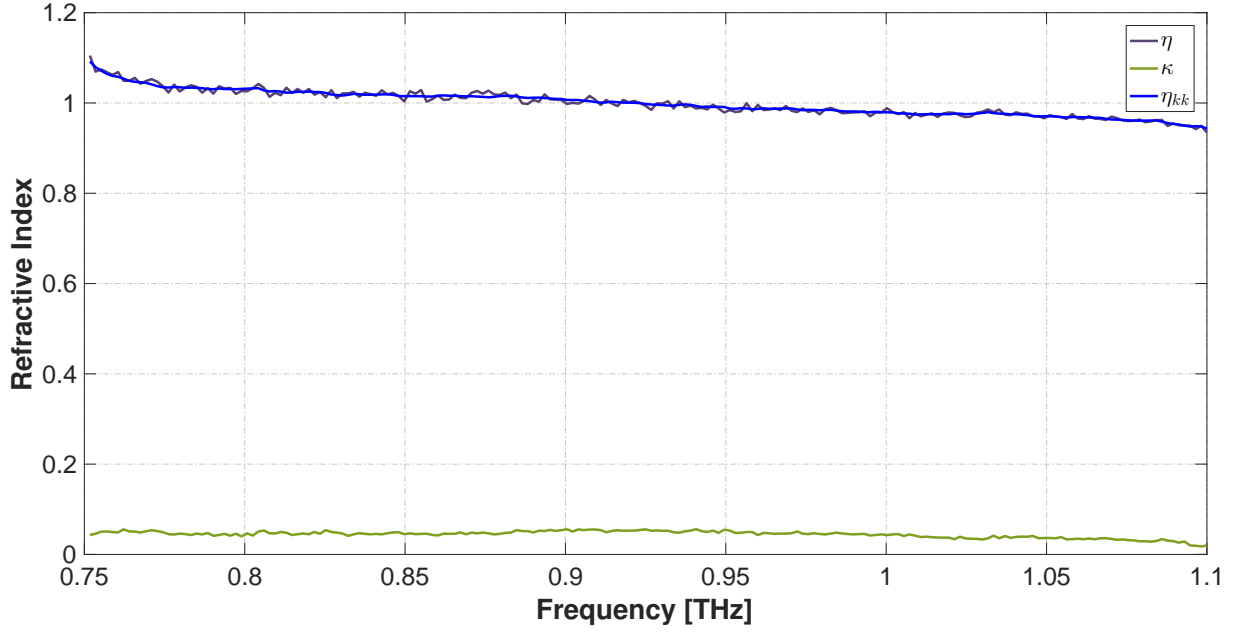


Figure 5.26: Refractive index of method based on K-K relation for material B2.

Fig. 5.26 depicts the measured refractive index of material B2 as a function of frequency using the above equations. As can be inferred, after comparing with the NRW method based on group delay, the method based on K-K relationships is not solemnly affected by the thickness of the sample d , nor does it require the interval between adjacent frequency points to be sufficiently small. But it also has limitations as can be seen from the Eq. (5.61) that the integral is $0 \rightarrow \infty$, so the scattering parameters measured should be in the entire frequency range, but beyond possibility. The frequency range obtained in the experiment must be limited, which will truncate the integral, resulting in inaccurate results, just approximations. For example, it can be observed in the Fig. 5.26 that η_{kk} has a rapid change at the beginning and end of the frequency range, which is most likely due to the truncation integral. In order to reduce the errors caused by the finite frequency range, we can adopt the largest possible frequency range offered by the measurement equipment, or use the subtractive K-K relations, which are generally divided into singly subtractive K-K relations (SSKK) and multiply subtractive K-K relations (MSKK). Besides, as can be seen from Eq. (5.62) the value of m is determined depending on its relation with η and η_{kk} . Hence, m takes a series of values depending on the closeness of the η and η_{kk} .

curves at that frequency point. The equation can be obtained as follows

$$\begin{aligned}\eta(\omega') - \eta(\omega'') &= \frac{2}{\pi}P \int_0^\infty \frac{w\kappa(w)}{w^2 - w'^2}dw - \frac{2}{\pi}P \int_0^\infty \frac{w\kappa(w)}{w^2 - w''^2}dw \\ &= \frac{2(\omega'^2 - \omega''^2)}{\pi}P \int_0^\infty \frac{w\kappa(w)}{(w^2 - w'^2)(w^2 - w''^2)}dw\end{aligned}\quad (5.66)$$

where $\eta(\omega'')$ is a priori known refractive index at a reference point ω'' . MSKK is similar to SSKK, but requires more reference points.

In the SSKK, the real refractive index at a single frequency point inside the frequency range is to be known, hence measured beforehand serving as a reference point to improve accuracy of K-K relations.

5.7 Concluding Remarks

This chapter unravels the issue of material characterization in the THz spectrum:

- ⇒ The frequency dependent material parameters such as permittivity, refractive index and absorption coefficient are mandatory to analyze and model the wave propagation mechanism. Hence, this work reports the first ever transmission measurements for six (6) material groups comprising of 20 common indoor building materials at frequencies from 750 GHz to 1.1 THz.
- ⇒ The commercially available VNA-based *Swissto12* system is employed for characterizing the chosen materials on the basis of their dielectric properties, extracted from the scattering measurements using novel analysis techniques.
- ⇒ The low values of S_{21} for all six groups signify the high losses during transmission thus regarding these as high-loss materials. These losses perhaps attribute to the transmission attenuation, thickness of the sample and its permittivity, surface scattering, and absorption in the material samples.
- ⇒ A number of novel analysis techniques such as K-K relations are reviewed to carry out the conversion of S parameters to complex dielectric properties replacing the conventional THz-TDS system based on down conversion method employed previously for similar measurements.

Conclusions and Future Challenges

This dissertation is another one pacing forward with the aim to achieve 100 Gb/s wireless links anywhere and anytime. The line of action towards fulfilling this target first and foremost calls for a thorough study of the basic propagation mechanisms followed by the detailed typology of the surfaces along with the solutions posed by the diffuse scattering from rough surfaces. Finally, the development of a novel RTA to overcome the conventional GHz ray tracer's limitations and material characterization on the basis of dielectric properties is successfully carried out/accomplished to analyze and model the wave propagation mechanism.

Each chapter of this dissertation is a link in the chain of actions. The notable conclusions rather contributions from this work are:

6.1 Conclusions

Impact Of Candle Flame On THz Communication Links → Three different antenna configurations (Horn-Horn, Horn-Open and Open-Open) are employed to contemplate the impact of candle flame on the ultra-broadband THz communication across the spectrum of interest from 300 GHz to 310 GHz. The channel measurements are performed for two different distances i.e., 0.5 m and 1 m. The findings from this work demonstrate that the THz electromagnetic wave is exposed to slight attenuation mostly caused by the water vapour attenuation. The wave propagation is delayed (phase-shifted) and comparatively more prominent in the Open-Open antenna configuration. However, this slight attenuation does not cause any hindrance in the characterization and localization of materials at THz frequencies.

Impact Of Surface Roughness On The THz Propagation Channels → The coverage map results obtained from the ray-tracing simulations in an LoS environment pinpoint to the peculiar pattern of scattering. The scattering phenomenon significantly persists in the points near to the walls and distant from the TX. The almost identical average attenuations for varied degrees of roughness recorded from our simulations in LoS scenario highlight the effect of a dominant direct path as opposed to the scattered channel paths with almost negligible effect.

Comparison Of The Surface Scattering Models → Diffuse scattering is among the major challenges at THz frequencies when modeling the THz propagation channels. A thorough study on the four (4) widely accepted scattering models (R-R, ER, cB-K and mB-K) along with their comparison is presented in this work as a step towards resolving the scattering problem. A noteworthy finding from this comparison and further affirmed by the simulation results as well is that the ER model can be considered a good choice modeling THz channels, though proposed for channel modeling at 60 GHz.

Novel Ray-Tracing Algorithm → The limitations of the conventional GHz RT and the smooth materials turning rough now at THz frequencies are the two main reasons that compelled us to develop our own THz RTA for channel modeling at THz frequencies. This self-programmed 3D RTA is developed by integrating the above mentioned scattering models for rough surfaces and can work completely on standalone basis. The GUI for our RTA can be operated without any prior MATLAB experience to simulate THz scenarios thus catering users of all levels.

Novel THz Material Characterization Techniques → This dissertation proclaims the first ever transmission measurements for six (6) material groups (*wood, plaster, paper, brick, glass and leather*) at frequencies from 750 GHz – 1.1 THz employing the *Swissto12* system using up-conversion (frequency domain) method. The characterization of the material dielectric properties assists in analyzing and modeling the wave propagation at these frequencies.

6.2 Future Challenges

The most difficult aspect of this dissertation has been declaring it finished. Some further interesting and promising research topics are summarized as follows:

Diffraction From Rough Surfaces At THz Frequencies → The diffraction encountered at THz frequencies is still a topic that warrants further study and research. Particularly, for desktop scenarios where a variety of common desktop item can serve as an obstructive purpose for diffraction. Prior research affirms that UTD is a well suited approach for the diffraction modeling at 300 GHz from smooth surfaces. However, this approach has not been studied yet for rough surfaces at THz frequencies. This topic hence awaits to be explored and further investigated for resolving the problem of diffraction at THz frequencies.

Full Coverage With NLoS Communication Channels → The measurements carried out for the chosen six material groups report that all of these undergo reflection losses except for comparatively less loss witnessed in the case of wood. Hence, in order to attain a full coverage free of or with minimal reflection loss, the idea of introducing reflection mirrors can be a good bait for further research.

Horn Antenna Misalignments → The horn antennas interestingly have a divergent beam in their spatial structure where the beam spot size gets larger at farther distances, unless collimating lenses are used. In future, a study on the horn antenna misalignments (horizontal-, vertical-, angular-displacements) can be an interesting topic particularly with a concomitant in-depth study on the beam spot diameter.

Non-Gaussian Distributed Rough Surfaces → This dissertation probed and studied the Gaussian rough surfaces and their impact at THz frequencies. However, the non-Gaussian surfaces are left unexplored in this work. The study of the non-Gaussian height distribution effects on the total received and scattered power can open up new horizons for channel modeling at THz frequencies. This can be elaborated by adopting suitable scattering models for resolving the scattering problems similar to those experienced in case of Gaussian rough surfaces. Meanwhile, embedding directly the 3D surface topography measurement data obtained from the surface measurements instruments into the RTA can be an interesting advancement in future.

THz Scattering Models → A comparison of the widely accepted THz models (R-R, ER, cB-K and mB-K) is already presented in this study work in terms of the frequency-domain CTFs for $f = 300...310$ GHz in LoS and NLoS scenarios. However, in order to evaluate the suitability of these aforementioned models as to which one proves more suited for which scenario, one needs

to refer back to the measurements.

Photo-realistic GPU-enabled 3D THz Ray-tracer → The novel 3D THz ray tracer employed in this study for flat surfaces only can be futuristically enhanced into a photo-realistic GPU-enabled 3D THz ray tracer. This visionary enhancement can be then employed for non-flat surfaces as well with comparatively expedited results.

Reflected Multipaths → The elaborate *in-room* study on the chosen material groups can be augmented further to assay the reflected paths achievable with maximum path lengths for each of these materials. This may take the deployment of THz wireless communications a step further.

Look Through Distant Objects → A huge leap in the THz spectrum is already witnessed but the envisioned future awaits prospective applications overpowering the frames of mind once the look through experiments already accomplished for nearby indoor materials employing the *Swissto12* system are taken a step further to look through distant objects. This will bring out the THz (or T-wave) from the confined in-room scenarios to achieve multi-room radio coverage thus facilitating several new applications in human-to-human, human-to-thing, and thing-to-thing communications, beyond thought in the past.

This brings the dissertation to an end. However, the challenges summarized above open up new avenues for future research.

List of Publications

Journal Papers

- [1] **F. Sheikh**, Y. Gao, and T. Kaiser, “A Study of Diffuse Scattering in Massive MIMO Channels at Terahertz Frequencies”, IEEE Transactions on Antennas and Propagation, accepted, August 2019
- [2] M. Hermelo, R. Chuenchom, V. Rymanov, T. Kaiser, **F. Sheikh**, A. Czylik, and A. Stöhr, “Photonic-Assisted mm-Wave and THz Wireless Transmission towards 100 Gbit/s Data Rate”, Frequenz Journal of RF-Engineering and Telecommunications, Band 71, Heft 9-10, pp. 1-13, August 2017
- [3] **F. Sheikh**, N. Zarifeh, and T. Kaiser, “Terahertz Band: Channel Modelling for Short-range Wireless Communications in the Spectral Windows”, IET Microwaves, Antennas & Propagation, vol. 10, no. 13, pp. 1435-1444, October 2016

Conference Papers

- [1] **F. Sheikh**, I. Mabrouk, A. Alomainy, Q. Abbasi, and T. Kaiser, “Indoor Material Properties Extraction from Scattering Parameters at Frequencies from 750 GHz to 1.1 THz”, IEEE MTT-S International Microwave Workshop Series on Advanced Materials and Processes (IMWS-AMP), pp. 1-3, Bochum, Germany, July 2019
- [2] **F. Sheikh** and T. Kaiser, “A Modified Beckmann-Kirchhoff Scattering Model for Slightly Rough Surfaces at Terahertz Frequencies”, IEEE AP-S Symposium on Antennas and Propagation and USNC-URSI, pp. 1-2, Atlanta, USA, July 2019

- [3] **F. Sheikh**, M. Alissa, A. Zahid, Q. Abbasi, and T. Kaiser, "Atmospheric Attenuation Analysis in Indoor THz Communication Channels", IEEE AP-S Symposium on Antennas and Propagation and USNC-URSI, pp. 1-2, Atlanta, USA, July 2019
- [4] Y. Zantah, **F. Sheikh**, A. Abbas, M. Alissa, and T. Kaiser, "Channel Measurements in Lecture Room Environment at 300 GHz", IEEE 2nd Int. Workshop on Mobile THz Systems (IWMTS 2019), pp. 1-5, Bad Neuenahr, Germany, July 2019
- [5] A. Ghwaji, **F. Sheikh**, T. Schulze, I. Willms, and T. Kaiser, "Preliminary Analysis of Candle Flame Impact on THz Electromagnetic Wave Propagation", IEEE 2nd Int. Workshop on Mobile THz Systems (IWMTS 2019), pp. 1-5, Bad Neuenahr, Germany, July 2019
- [6] **F. Sheikh**, Q. Abbasi, and T. Kaiser, "On Channels with Composite Rough Surfaces at Terahertz Frequencies", in Proc. 13th European Conference on Antennas and Propagation (EuCAP), pp. 1-5, Krakow, Poland, April 2019
- [7] **F. Sheikh** and T. Kaiser, "Rough Surface Analysis for Short-Range Ultra-Broadband THz Communications", IEEE AP-S Symposium on Antennas and Propagation and USNC-URSI, pp. 1-2, Boston, USA, July 2018
- [8] **F. Sheikh**, D. Lessy, and T. Kaiser, "A Novel Ray-Tracing Algorithm for Non-specular Diffuse Scattered Rays at Terahertz Frequencies", IEEE 1st Int. Workshop on Mobile THz Systems (IWMTS 2018), pp. 1-6, Velen, Germany, July 2018
- [9] **F. Sheikh**, D. Lessy, M. Alissa, and T. Kaiser, "A Comparison Study of Non-specular Diffuse Scattering Models at Terahertz Frequencies", IEEE 1st Int. Workshop on Mobile THz Systems (IWMTS 2018), pp. 1-6, Velen, Germany, July 2018
- [10] **F. Sheikh**, M. El-Absi, Y. Gao, and T. Kaiser, "Terahertz Band: Analysis of Sounding Bandwidth and Center Frequency on Power Delay Profile Model", Antennas and Propagation Conference (LAPC), pp. 1-5, Loughborough, UK, November 2015
- [11] **F. Sheikh**, M. El-Hadidy, and T. Kaiser, "Terahertz Band: Indoor Ray Tracing Channel Model Considering Atmospheric Attenuation", IEEE AP-S Symposium on Antennas and Propagation and USNC-URSI, pp. 1782-1783, Vancouver, Canada, July 2015

Related work by the author

- [1] A. Zahid, H. Abbas, **F. Sheikh**, T. Kaiser, A. Zoha, M. Imran, and Q. Abbasi, “Monitoring Health Status and Quality Assessment of Leaves Using Terahertz Frequency”, IEEE AP-S Symposium on Antennas and Propagation and USNC-URSI, pp. 1-2, Atlanta, USA, July 2019
- [2] M. Alissa, **F. Sheikh**, A. Abbas, and T. Kaiser, “Wave Scattering from Non-Gaussian Rough Surfaces at Terahertz Frequencies”, IEEE 2nd Int. Workshop on Mobile THz Systems (IWMTS 2019), pp. 1-5, Bad Neuenahr, Germany, July 2019
- [3] J. Barowski, J. Jebramcik, I. Alwaneh, **F. Sheikh**, T. Kaiser, and I. Rolfes, “A Compact Measurement Setup for In-Situ Material Characterization in the Lower THz Range”, IEEE 2nd Int. Workshop on Mobile THz Systems (IWMTS 2019), pp. 1-5, Bad Neuenahr, Germany, July 2019

Bibliography

- [1] S. Cherry, “Edholmes law of bandwidth”, *IEEE Spectr.*, vol. 41, no. 7, pp. 58-60, Jul. 2004
- [2] G. Fettweis and E. Zimmermann, “ICT Energy Consumption — Trends and Challenges”, *The 11th International Symposium on Wireless Personal Multimedia Communications (WPMC 2008)*, Jan. 2008
- [3] H. J. Song and T. Nagatsuma, “Handbook of Terahertz Technologies: Devices and Applications”, *Pan Stanford Pub.*, Singapore, 2015
- [4] J. D. Cressler and G. Niu, “Silicon–Germanium Heterojunction Bipolar Transistors”, *Artech House Publishers*, Jan. 2003
- [5] K. Shinohara, D. C. Regan, Y. Tang, A. L. Corrion, D. F. Brown, J. C. Wong, J. F. Robinson, H. H. Fung, A. Schmitz, T. C. Oh, S. J. Kim, P. S. Chen, R. G. Nagele, A. D. Margomenos, and M. Micovic, “Scaling of GaN HEMTs and Schottky Diodes for Submillimeter-Wave MMIC Applications”, *IEEE Transactions on Electron Devices*, vol. 60, no. 10, pp. 2982-2996, Oct. 2013
- [6] G. J. Foschini and M. J. Gans, “On limits of wireless communications in a fading environment when using multiple antennas”, *Wireless Personal Communications*, vol. 6, no. 3, pp. 311-335, Mar. 1998
- [7] A. Goldsmith, S. A. Jafar, N. Jindal, and S. Vishwanath, “Capacity limits of MIMO channels”, *IEEE Journal on Selected Areas in Communications*, vol. 21, no. 5, pp. 684-702, Jun. 2003

- [8] T. L. Marzetta and B. M. Hochwald, "Capacity of a mobile multiple-antenna communication link in Rayleigh flat fading", *IEEE Transactions on Information Theory*, vol. 45, no. 1, pp. 139-157, Jan. 1999
- [9] T. L. Marzetta, "Noncooperative Cellular Wireless with Unlimited Numbers of Base Station Antennas", *IEEE Transactions on Wireless Communications*, vol. 9, no. 11, pp. 3590-3600, Oct. 2010
- [10] S. Berman, D. S. Greenhouse, I. Bailey, R. D. Clear, and T. Raasch, "Human electroretinogram responses to video displays, fluorescent lighting, and other high frequency sources", *Optometry and vision science*, vol. 68, no. 11, pp. 645-662, Sep. 1991
- [11] A. Maltsev, A. Sadri, R. Maslennikov, A. Davydov, and A. Khoryaev, "Channel Models for 60 GHz WLAN Systems", *IEEE 802.11-08/0811r1*, Jul. 2008
- [12] M. Shafi, A. F. Molisch, P. J. Smith, T. Haustein, P. Zhu, P. D. Silva, F. Tufvesson, A. Benjebbour, and T. Raasch, "5G: A Tutorial Overview of Standards, Trials, Challenges, Deployment and Practice", *IEEE Journal on Selected Areas in Communications*, vol. 35, no. 6, pp. 1201-1221, Jun. 2017
- [13] F. Sheikh, N. Zarifeh, and T. Kaiser, "Terahertz band: Channel modelling for short-range wireless communications in the spectral windows", *IET Microwaves, Antennas & Propagation*, vol. 10, no. 13, pp. 1435-1444, Oct. 2016
- [14] R. Piesiewicz, T. K. Ostmann, N. Krumbholz, D. Mittleman, M. Koch, J. Schoebei, and T. Kürner, "Short-range ultra-broadband terahertz communications: Concepts and perspectives", *IEEE Antennas Propog. Mag.*, vol. 49, no. 6, pp. 24-39, Dec. 2007
- [15] T. Schneider, A. Wiatrek, S. Preussler, M. Grigat, and R. P. Braun, "Link Budget Analysis for Terahertz Fixed Wireless Links", *IEEE Trans. on Terahertz Science and Technology*, vol. 2, no. 2, pp. 250-256, Feb. 2012
- [16] F. Sheikh, D. Lessy, M. Alissa, and T. Kaiser, "A Comparison Study of Non-specular Diffuse Scattering Models at Terahertz Frequencies", in *IEEE 1st. International Workshop on Mobile Terahertz Systems (IWMTS)*, pp. 1-6, Jul. 2018
- [17] S. Priebe, M. Jacob, C. Jastrow, T. K. Ostmann, T. Schrader, and T. Kürner, "A Comparison of Indoor Channel Measurements and Ray Tracing Simulations at 300 GHz", *35th*

- International Conference on Infrared Millimeter and Terahertz Waves (IRMMW-THz)*, pp. 1-2, Sep. 2010
- [18] R. Piesiewicz, C. Jansen, D. Mittleman, T. K. Ostmann, M. Koch, and T. Kürner, “Scattering Analysis for the Modeling of THz Communication Systems”, *IEEE Transactions on Antennas and Propagation*, vol. 55, no. 11, pp. 3002-3009, Dec. 2007
- [19] C. Jansen, S. Priebe, C. Möller, M. Jacob, H. Dierke, M. Koch, and T. Kürner, “Diffuse Scattering From Rough Surfaces in THz Communication Channels”, *IEEE Transactions on Terahertz Science and Technology*, vol. 1, no. 2, pp. 462-472, Nov. 2011
- [20] M. F. Hermelo, R. Chuenchom, V. Rymanov, T. Kaiser, F. Sheikh, A. Czylik, and A. Stöhr, “Photonic-Assisted mm-Wave and THz Wireless Transmission towards 100 G-bit/s Data Rate”, *Frequenz: Journal of RF-Engineering and Telecommunications*, vol. 71, no. 9-10, pp. 485-498, Aug. 2017
- [21] F. Sheikh, M. Alissa, A. Zahid, Q. Abbasi, and T. Kaiser, “Atmospheric Attenuation Analysis in Indoor THz Communication Channels”, *IEEE AP-S Symposium on Antennas and Propagation and USNC-URSI*, pp. 1-2, Jul. 2019
- [22] F. Sheikh, M. El-Absi, Y. Gao, and T. Kaiser, “Terahertz Band: Analysis of Sounding Bandwidth and Center Frequency on Power Delay Profile Model”, *Antennas and Propagation Conference (LAPC)*, pp. 1-5, Nov. 2015
- [23] F. Sheikh, M. El-Hadidy, and T. Kaiser, “Terahertz Band: Indoor Ray Tracing Channel Model Considering Atmospheric Attenuation”, *IEEE AP-S Symposium on Antennas and Propagation and USNC-URSI*, pp. 1782-1783, Jul. 2015
- [24] C. Oestges, B. Clerckx, L. Raynaud, and D. V. Janvier, “Deterministic Channel Modelling and Performance Simulation of Microcellular Wide-Band Communication Systems”, *IEEE Transactions on Vehicular Technology*, vol. 51, no. 6, pp. 1422-1430, Nov. 2002
- [25] H. T. Friis, “A Note on a Simple Transmission Formula”, *Proceedings of the IRE*, vol. 34, no. 5, pp. 254-256, May 1946
- [26] International Telecommunication Union, “Attenuation by atmospheric gases”, *P Series Radiowave propagation*, Recommendation ITU-R P.676-10, Sep. 2013

- [27] Y. Zantah, F. Sheikh, A. Abbas, M. Alissa, and T. Kaiser, "Channel Measurements in Lecture Room Environment at 300 GHz", *IEEE 2nd Int. Workshop on Mobile THz Systems (IWMTS 2019)*, pp. 1-5, Jul. 2019
- [28] A. Ghwaji, F. Sheikh, T. Schulze, I. Willms, and T. Kaiser, "Preliminary Analysis of Candle Flame Impact on THz Electromagnetic Wave Propagation", *IEEE 2nd Int. Workshop on Mobile THz Systems (IWMTS 2019)*, pp. 1-5, Jul. 2019
- [29] A. Maltsev, R. Maslennikov, A. Lomayev, A. Sevastyanov, and A. Khoryaev, *IEEE 802.11-09/0431r0*", Apr. 2009
- [30] P. Beckmann and A. Spizzichino, "The Scattering of Electromagnetic Waves from Rough Surfaces", *Artech House Radar Library*, Boston, USA, 1963
- [31] R. Piesiewicz, C. Jansen, S. Wietzke, D. Mittleman, M. Koch, and T. Kürner, "Properties of Building and Plastic Materials in the THz Range", *International Journal of Infrared and Millimeter Waves*, vol. 28, no. 5, pp. 363-371, May 2007
- [32] J. Ma, R. Shrestha, L. Moeller, and D. Mittleman, "Channel performance for indoor and outdoor terahertz wireless links", *APL Photonics*, vol. 3, no. 5, pp. 1-12, Jan. 2018
- [33] F. G. Bass and I. M. Fuks, "Wave Scattering from Statistically Rough Surfaces", *International Series in Natural Philosophy (Volume 93)*, Pergamon Press, New York, USA, Jan. 1979
- [34] E. L. Feinberg, "The propagation of Radio Waves along the surface of the earth", *AF Systems Command*, 1967
- [35] I. M. Fuks, "Radio wave scattering theory on the distributed surface of the sea", *Institute of Radio Physics and Electronics of the Ukrainian Academy of Sciences*, vol. 9, no. 5, pp. 876-887, 1966
- [36] R. N. Gurzhi and S. M. Shevchenko, "Thermal conductivity theory of thin dielectric models", *Soviet Physics - Journal of Experimental and Theoretical Physics (JETP)*, vol. 25, no. 3, pp. 534-536, 1967
- [37] G. T. Ruck, "Radar Cross Section Handbook", *Plenum Press*, New York, 1970

- [38] R. Vaughan and J. Andersen, “Channels, Propagation and Antennas for Mobile Communications”, *IET*, 2003
- [39] Y. Zhao, G. Wang, and T. Lu, “Characterization of Amorphous and Crystalline Rough Surface: Principles and Applications”, *1st Edition (Volume 37)*, Academic Press, San Diego, USA, Oct. 2000
- [40] A. Goulianos, A. Freire, T. Barratt, E. Mellios, P. Cain, M. Rumney, A. Nix, and M. Beach, “Measurements and Characterisation of Surface Scattering at 60 GHz”, *2017 IEEE 86th Vehicular Technology Conference (VTC-Fall)*, pp. 1-5, Sep. 2017
- [41] A. K. Fung, “Scattering and depolarization of EM waves from a rough surface”, *Proc. IEEE (Communications)*, vol. 54, pp. 395-396, Mar. 1966
- [42] P. Beckmann, “The depolarization of electromagnetic waves scattered from rough surfaces”, *Proc. Symp. Electromagnetic Theory and Antennas*, E. C. Jordan, Ed. New York: Pergamon, pp. 717-726, 1963
- [43] M. Jacob, S. Priebe, R. Dickhoff, T. Ostmann, T. Schrader, and T. Kürner, “Diffraction in mm and Sub-mm Wave Indoor Propagation Channels”, *IEEE Transactions on Microwave Theory and Technique*, vol. 60, no. 3, pp. 833-844, Mar. 2012
- [44] R. Kouyoumjian and P. Pathak, “Uniform Geometrical Theory of Diffraction for an Edge in a Perfectly Conducting Surface”, *Proc. IEEE*, vol. 62, no. 11, pp. 1448-1461, 1974
- [45] C. Han, A. O. Bicen, and I. F. Akyildiz, “Multi-Ray Channel Modeling and Wideband Characterization for Wireless Communications in the Terahertz Band”, *IEEE Transactions on Wireless Communications*, vol. 14, no. 5, pp. 2402-2412, May 2015
- [46] J. Kokkonen, P. Rintanen, J. Lehtomäki, and M. Juntti, “Diffraction Effects in Terahertz Band - Measurements and Analysis”, *2016 IEEE Global Communications Conference (GLOBECOM)*, , pp. 1-6, Dec. 2016
- [47] C. Cheng, S. Kim, and A. Zajic “Study of Diffraction at 30 GHz, 140 GHz, and 300GHz”, *IEEE AP-S Symposium on Antennas and Propagation and USNC-URSI*, pp. 1-2, Jul. 2018
- [48] T. Ostmann, M. Jacob, S. Priebe, R. Dickhoff, T. Schrader, and T. Kürner, “Diffraction Measurements at 60 GHz and 300 GHz for Modeling of Future THz Communication Sys-

- tems”, *Proc. 37th Int. Conf. Infr. Millim. Terahertz Waves (IRMMW-THz)*, pp. 1-2, Sep. 2012
- [49] H. Hamada, T. Fujimura, I. Abdo, K. Okada, H. Song, H. Sugiyama, H. Matsuzaki, and H. Nosaka, “300-GHz. 100-Gb/s InP-HEMT Wireless Transceiver Using a 300-GHz Fundamental Mixer”, *2018 IEEE/MTT-S International Microwave Symposium (IMS 2018)*, pp. 1480-1483, Jun. 2018
- [50] S. Lee, R. Dong, T. Yoshida, S. Amakawa, S. Hara, A. Kasamatsu, J. Sato, and M. Fujishima, “An 80Gb/s 300GHz-Band Single-Chip CMOS Transceiver”, *2018 IEEE International Solid-State Circuits Conference (ISSCC)*, pp. 1480-1483, Jun. 2018
- [51] W. Deal, A. Zamora, K. Leong, P. Liu, W. Yoshida, J. Zhou, M. Lange, B. Gorospe, K. Nguyen, and X. Mei, “A 670 GHz low noise amplifier with \downarrow 10 dB packaged noise figure”, *IEEE Microw. Wirel. Compon. Lett.*, vol. 26, no. 10, pp. 837-839, Sep. 2016
- [52] I. Kallfass, F. Boes, T. Messinger, J. Antes, A. Inam, U. Lewark, A. Tessmann, and R. Henneberger, “64 Gbit/s transmission over 850m fixed wireless link at 240 GHz carrier frequency”, *Journal of Infrared, Millimeter, and Terahertz Waves*, vol. 36, no. 2, pp. 221-233, Feb. 2015
- [53] A. Fox, B. Heinemann, H. RÜcker, R. Barth, G. Fischer, C. Wipf, S. Marschmeyer, K. Aufinger, J. Böck, S. Boguth, H. Knapp, R. Lachner, W. Liebl, D. Manger, T. Meister, A. Pribil, and J. Wursthorn, “Advanced heterojunction bipolar transistor for half-THz SiGe BiCMOS technology”, *IEEE Electron Device Lett.*, vol. 36, no. 7, pp. 642-644, Jul. 2015
- [54] W. Deal, X. Mei, V. Radisic, K. Leong, S. Sarkozy, B. Gorospe, J. Lee, P. Liu, W. Yoshida, J. Zhou, J. Uyeda, and R. Lai, “Demonstration of a 0.48 THz Amplifier Module Using InP HEMT Transistors”, *IEEE Microw. Wirel. Compon. Lett.*, vol. 20, no. 5, pp. 289-291, May 2010
- [55] V. Radisic, K. Leong, X. Mei, S. Sarkozy, W. Yoshida, and W. Deal, “Power amplification at 0.65 THz using INP HEMTs”, *IEEE Trans. Microw. Theory Techn.*, vol. 60, no. 3, pp. 724-729, Mar. 2012

- [56] O. Momeni and E. Afshari, “High power terahertz and millimeter-wave oscillator design: A systematic approach”, *IEEE J. Solid-State Circuits*, vol. 46, no. 3, pp. 583–597, Mar. 2011
- [57] J. Kim, H. Song, K. Ajito, M. Yaita, and N. Kukutsu, “A 325 GHz quadrature voltage controlled oscillator with superharmonic-coupling”, *IEEE Microw. Wireless Compon. Lett.*, vol. 23, no. 8, pp. 430–432, Aug. 2013
- [58] H. Song, J. Kim, K. Ajito, N. Kukutsu, and M. Yaita, “50-Gb/s direct conversion QPSK modulator and demodulator MMICs for terahertz communications at 30 GHz”, *IEEE Trans. Microw. Theory Techn.*, vol. 62, no. 3, pp. 600–609, Mar. 2014
- [59] H. Hamada, T. Kosugi, H. Song, M. Yaita, A. Moutaouakil, H. Matsuzaki, and A. Hirata, “300-GHz band 20-Gbps ASK transmitter module based on InP-HEMT MMICs”, in *Proc. IEEE Compound Semicond. Integr. Circuit Symp.*, pp. 1-4, Oct. 2015
- [60] M. Seo, M. Urteaga, M. Rodwell, and M. Choe, “A 300 GHz PLL in an InP HBT technology”, in *IEEE MTT-S Int. Microw. Symp. Dig.*, pp. 1-4, Jun. 2011
- [61] M. Seo, M. Urteaga, A. Young, J. Hacker, A. Skalare, R. Lin, and M. Rodwell, “A single-chip 630 GHz transmitter with 210 GHz sub-harmonic PLL local oscillator in 130 nm InP HBT”, in *IEEE MTT-S Int. Microw. Symp. Dig.*, pp. 1-3, Jun. 2012
- [62] IEEE Standard for High Data Rate Wireless Multi-Media Networks, “100 Gb/s Wireless Switched Point-to-Point Physical Layer”, in *IEEE Std 802.15.3d-2017*, pp. 1-55, Oct. 2017
- [63] V. Degli Esposti, “A Diffuse Scattering Model for Urban Propagation Prediction”, *IEEE Transactions on Antennas and Propagation*, vol. 49, no. 7, pp. 1717–1728, Jul. 2001
- [64] F. Sheikh and T. Kaiser, “A Modified Beckmann-Kirchhoff Scattering Model for Slightly Rough Surfaces at Terahertz Frequencies”, *IEEE AP-S Symposium on Antennas and Propagation and USNC-URSI*, pp. 1-2, Jul. 2019
- [65] F. Sheikh, Q. Abbasi, and T. Kaiser, “On Channels with Composite Rough Surfaces at Terahertz Frequencies”, in *Proc. 13th European Conference on Antennas and Propagation (EuCAP)*, pp. 1-5, Apr. 2019

- [66] F. Sheikh and T. Kaiser, “Rough Surface Analysis for Short-Range Ultra-Broadband THz Communications”, *IEEE AP-S Symposium on Antennas and Propagation and USNC-URSI*, pp. 1-2, Jul. 2018
- [67] S. Nayar, K. Ikeuchi, and T. Kanade, “Surface reflection: physical and geometrical perspectives”, *IEEE Transactions on Pattern Analysis and Machine Intelligence*, vol. 13, no. 7, pp. 611–634, Jul. 1991
- [68] Remcom Inc., Wireless InSite Users Manual version 2.7, “Electromagnetic Simulation Software by Remcom ”, PA, USA
- [69] S. Priebe, M. Jacob, and T. Kürner, “The Impact of Antenna Directivities on THz Indoor Channel Characteristics”, *Proceedings of the 6th European Conference on Antennas and Propagation (EUCAP)*, pp. 478–482, May. 2012
- [70] S. Priebe, M. Jacob, and T. Kürner, “Affection of THz indoor communication links by antenna misalignment”, *Proceedings of the 6th European Conference on Antennas and Propagation (EUCAP)*, pp. 483–487, May. 2012
- [71] Y. Cocheril, R. Vauzelle, L. Aveneau, and M. Khoudeir, “Rough Surfaces Influence on an Indoor Propagation Simulation at 60 GHz”, *ECPS*, Mar. 2005
- [72] S. Tariq, C. Despins, S. Affes, and C. Nerguizian, “Rough Surface Scattering Analysis at 60 GHz in an Underground Mine Gallery”, *2014 IEEE International Conference on Communications Workshops (ICC)*, pp. 724–729, Jun. 2014
- [73] Alicona Imaging InfiniteFocus, “Alicona Imaging GmbH”, *Online*, Available: www.alicon.com, accessed in August 2019
- [74] R. Piesiewicz, T. Kleine-Ostmann, N. Krumbholz, D. Mittleman, M. Koch, and T. Kürner, “Terahertz characterisation of building materials”, *Electronics Letters*, vol. 41, no. 18, pp. 1002–1004, Sep. 2005
- [75] V. Degli Esposti, D. Guiducci, A. de’Marsi, P. Azzi, and F. Fuschini, “An Advanced Field Prediction Model Including Diffuse Scattering”, *IEEE Transactions on Antennas and Propagation*, vol. 52, no. 7, pp. 1717–1728, Jul. 2004
- [76] J. Stover, “Optical Scattering, Measurement and Analysis”, *2nd Edition*, SPIE Press, Washington, 1995

- [77] T. Vorburger, E. Marx, and T. Lettieri, “Regimes of surface roughness measurable with light scattering”, *Appl. Opt.*, vol. 32, no. 19, pp. 3401–3408, 1993
- [78] W. Ament, “Toward a theory of reflection by a rough surface”, *Proceedings of the IRE*, vol. 41, no. 1, pp. 142–146, Jan. 1953
- [79] V. Degli Esposti, F. Fuschini, E. Vitucci, and G. Falciasecca, “Measurement and Modelling of Scattering From Buildings”, *IEEE Transactions on Antennas and Propagation*, vol. 55, no. 1, pp. 143–153, Jan. 2007
- [80] S. Priebe, M. Jacob, C. Jansen, and T. Kürner, “Non-specular scattering modeling for THz propagation simulations”, *Proceedings of the 5th EUCAP*, pp. 1–5, Apr. 2011
- [81] J. Harvey, C. Vernold, A. Krywonos, and P. Thompson, “Diffracted radiance: a fundamental quantity in nonparaxial scalar diffraction theory”, *Applied Opt.*, vol. 38, no. 31, pp. 6469–6481, Jul. 1999
- [82] J. He and T. Yu, “Method of moments analysis of electromagnetic scattering from a general three-dimensional dielectric target embedded in a multilayered medium”, *Radio Science*, vol. 35, no. 2, pp. 305–313, Mar. 2000
- [83] J. Bourgeois and G. Smith, “A fully three-dimensional simulation of a ground-penetrating radar: FDTD theory compared with experiment”, *IEEE Trans. on Geo. and Rem. Sens.*, vol. 34, no. 1, pp. 36–44, Jan. 1996
- [84] R. Harrington and L. Harrington, “Field Computation by Moment Methods”, *Oxford University Press, Inc.*, 1996
- [85] C. Lim, M. Lee, R. Burkholderet, J. Volakis, and R. Marhefka, “60 GHz indoor propagation studies for wireless communications based on a Ray-Tracing method”, *EURASIP Journal on Wireless Communications and Networking*, vol. 7, no. 1, pp. 1687–1699, Jan. 2007
- [86] F. Sheikh, Y. Gao, and T. Kaiser, “A Study of Diffuse Scattering in Massive MIMO Channels at Terahertz Frequencies”, *IEEE Transactions on Antennas and Propagation*, (*Major Revision round*), August 2019

- [87] F. Sheikh, D. Lessy, and T. Kaiser, “A Novel Ray-Tracing Algorithm for Non-specular Diffuse Scattered Rays at Terahertz Frequencies”, in *IEEE 1st. International Workshop on Mobile Terahertz Systems (IWMTS)*, pp. 1-6, Jul. 2018
- [88] A. Maltsev, A. Sadri, R. Maslennikov, A. Davydov, and A. Khoryaev, “Channel Models for 60 GHz WLAN Systems”, *IEEE 802.11-09/0334r8*, May. 2010
- [89] A. Saleh and R. Valenzuela, “A statistical model for indoor multipath propagation”, *IEEE Journal on Selected Areas in Communications*, vol. 5, no. 2, pp. 128–137, Feb. 1987
- [90] Q. Spencer, M. Rice, B. Jeffs, and M. Jensen, “A statistical model for angle of arrival in indoor multipath propagation”, *IEEE 47th Vehicular Technology Conference. Technology in Motion*, pp. 1415–1419, May 1997
- [91] S. Priebe, M. Jacob, and T. Kürner, “AoA, AoD and ToA Characteristics of Scattered Multipath Clusters for THz Indoor Channel Modeling”, *Sustainable Wireless Technologies (European Wireless)*, pp. 188-196, Apr. 2011
- [92] E. Ali, I. Mahamod, R. Nordin, and N. Abdulah, “Beamforming techniques for massive MIMO systems in 5G: overview, classification, and trends for future research”, *rontiers of Information Technology & Electronic Engineering*, vol. 18, no. 6, pp. 753–772, Jun. 2017
- [93] E. Ali et al., “Beamforming techniques for massive MIMO systems in 5G: overview, classification, and trends for future research,” *Frontiers of Information Technology & Electronic Engineering*, vol. 18, no. 6, pp. 753–772, Jun. 2017.
- [94] E. Telatar, “Capacity of Multi-antenna Gaussian Channels”, *EURASIP Journal on Wireless Communications and Networking*, vol. 10, no. 6, pp. 585–595, Nov. 1999
- [95] V. Petrov, A. Pyattaev, D. Moltchanov, and Y. Koucheryavy, “Terahertz band communications: Applications, research challenges, and standardization activities”, *IEEE 8th International Congress on Ultra Modern Telecommunications and Control Systems and Workshops (ICUMT)*, pp. 183-190, Oct. 2016
- [96] S. Shams, M. Tahseen, and A. Kishk, “Wideband relative permittivity characterization of thin low permittivity textile materials based on ridge gap waveguides”, *IEEE Trans. Microw. Theory Techn.*, vol. 64, no. 11, pp. 3839–3850, Nov. 2016

- [97] J. Hammler, A. Gallant, and C. Balocco, “Free-Space Permittivity Measurement at Terahertz Frequencies With a Vector Network Analyzer”, *IEEE Transactions on Terahertz Science and Technology*, vol. 6, no. 6, pp. 817–823, Nov. 2016
- [98] T. Ozturk and M. Güneser, “Measurement Methods and Extraction Techniques to Obtain the Dielectric Properties of Materials”, *Electrical and Electronic Properties of Materials*, Ch. 3, no. 6, pp. 83–108, Nov. 2018
- [99] G. Shimonov, A. Koren, G. Sivek, and E. Socher, “Electromagnetic Property Characterization of Biological Tissues at D-Band”, *IEEE Transactions on Terahertz Science and Technology*, vol. 8, no. 2, pp. 155–160, Jan. 2018
- [100] P. Seiler and D. Plettemeier, “A Method for Substrate Permittivity and Dielectric Loss Characterization Up to Subterahertz Frequencies”, *IEEE Transactions on Microwave Theory and Techniques*, early access, pp. 1–12, Mar. 2019
- [101] D. Yao, K. Yan, X. Liu, S. Liao et al., “Characterizations of Tunable Terahertz Metamaterial by Using Asymmetrical Double Split-Ring Resonators (ADSRRs)”, *IEEE International Conference on Optical MEMS and Nanophotonics (OMN)*, pp. 310–317, Sep. 2018
- [102] A. Khalid, D. Cumming, R. Clarke, C. Li, and N. Ridler, “Evaluation of a VNA-based Material Characterization Kit at Frequencies from 0.75 THz to 1.1 THz”, *IEEE 9th UK-Europe-China Workshop on Millimetre Waves and Terahertz Technologies (UCMMT)*, pp. 31–34, Sep. 2016
- [103] F. Sheikh, I. Mabrouk, A. Alomainy, Q. Abbasi, and T. Kaiser, “Indoor Material Properties Extraction from Scattering Parameters at Frequencies from 750 GHz to 1.1 THz”, *IEEE MTT-S International Microwave Workshop Series on Advanced Materials and Processes (IMWS-AMP)*, pp. 1-3, Jul. 2019
- [104] J. Barowski, J. Jebramcik, I. Alwaneh, F. Sheikh, T. Kaiser, and I. Rolfes “A Compact Measurement Setup for In-Situ Material Characterization in the Lower THz Range”, in *IEEE 2nd. International Workshop on Mobile Terahertz Systems (IWMTS)*, pp. 1-5, Jul. 2019
- [105] R. Kohlhaas, A. Rehn, S. Nellen, M. Koch, M. Schell, R. Dietz, and J. Balzer, “Terahertz quasi time-domain spectroscopy based on telecom technology for 1550 nm”, *Optics letters*, vol. 25, no. 11, pp. 12851–12859, May 2017

- [106] C. Brenner, M. Hofmann, M. Scheller, M. Shakfa, M. Koch, I. Mayorga, A. Klehr, G. Erbert, and G. Tränkle, “Compact diode-laser-based system for continuous-wave and quasi-time-domain terahertz spectroscopy”, *Optics Express*, vol. 25, no. 11, pp. 3859–3861, Dec. 2010
- [107] J. Barowski, M. Zimmermanns, and I. Rolfes, “Millimeter-Wave Characterization of Dielectric Materials Using Calibrated FMCW Transceivers”, *IEEE Transactions on Microwave Theory and Techniques*, vol. 66, no. 8, pp. 3683–3689, Aug. 2018
- [108] J. Hammler, A. Gallant, and C. Balocco, “Free-Space Permittivity Measurement at Terahertz Frequencies With a Vector Network Analyzer”, *IEEE Transactions on Terahertz Science and Technology*, vol. 6, no. 6, pp. 817–823, Nov. 2016
- [109] P. Skocik and P. Neumann, “Measurement of Complex Permittivity in Free Space”, *Procedia Engineering*, vol. 100, pp. 100–104, 2015
- [110] N. Ridler, R. Clarke, and M. Salter, “‘Mind the Gap’ ... Establishing Measurement Capability in the Terahertz Gap Region – from 0.1 THz to 1.1 THz ”, *ARMMS RF & Microwave Society Conference*, pp. 1-6, Nov. 2019
- [111] J. Musil and F. Zacek, “Microwave Measurements of Complex Permittivity by Free Space Methods and Their Applications”, *Academia*, Band 22, Mar. 1986
- [112] J. Schultz, “Focused Beam Methods Measuring Microwave Materials in Free Space”, Oct. 2012
- [113] M. Aris, E. Kadir, D. Ghodgaonkar, and N. Khadri, “Comparison of Reflection and Transmission Method and Metal Back Method Measurement of Dielectric properties of transformer oil using free space microwave measurement system in 8 - 12 GHz frequency range”, *2009 Asia Pacific Microwave Conference*, pp. 1609-1612, Dec. 2009
- [114] J. Jarvis, E. Vanzura, and W. Kissick, “Improved technique for determining complex permittivity with the transmission/reflection method”, *IEEE Transactions on Microwave Theory and Techniques*, vol. 38, no. 8, pp. 1096–1103, Aug. 1990
- [115] A. Nicolson and G. Ross, “Measurement of the intrinsic properties of materials by time-domain techniques”, *IEEE Trans. Instrum. Meas.*, vol. 19, no. 4, pp. 377–382, Nov. 1970

- [116] P. Banerjee, G. Ghosh, and S. Biswas, “Measurement of dielectric properties of medium loss samples at X-Band frequencies”, *Journal of Optoelectronics and Advanced Materials*, vol. 12, no. 6, pp. 1367–1371, Jun. 2010
- [117] J. Kokkonen, J. Lehtomäki, V. Petrov, D. Moltchanov, and M. Juntti “Frequency domain penetration loss in the terahertz band”, *2016 Global Symposium on Millimeter Waves (GSMM) & ESA Workshop on Millimetre-Wave Technology and Applications*, pp. 1-4, Jun. 2016
- [118] Swissto12 SA, “Swissto12 MCK ”, *Online*, Available: <http://www.swissto12.com>, accessed in August 2019
- [119] H. Zhong et al., “A phase feature extraction technique for terahertz reflection spectroscopy”, *APL*, vol. 92, pp. 221106, Jun. 2008
- [120] (2019) THz BRIDGE Spectral Database, *Online*, Available: <http://www.frascati.enea.it/THz-BRIDGE/database/spectra/searchdb.htm>, accessed in February 2019
- [121] (2019) Columbia-Utrecht Reflectance and Texture Database (CURET), *Online*, Available: <http://www.cs.columbia.edu/CAVE/software/curet>, accessed in February 2019
- [122] (2019) High-resolution Transmission Molecular Absorption Database (HITRAN), *Online*, Available: <https://hitran.org>, accessed in August 2019
- [123] N. Pohl, T. Jaeschke, and K. Aufinger, “An Ultra-Wideband 80 GHz FMCW Radar System Using a SiGe Bipolar Transceiver Chip Stabilized by a Fractional-N PLL Synthesizer”, *IEEE Transactions on Microwave Theory and Techniques*, vol. 60, no. 3, pp. 757–765, Mar. 2012
- [124] A. Vicente, G. Dip, and C. Junqueira, “The step by step development of NRW method”, *2011 SBMO/IEEE MTT-S International Microwave and Optoelectronics Conference (IMOC 2011)*, pp. 738–742, Nov. 2011
- [125] A. Paula, M. Rezende, and J. Barroso, “Modified Nicolson-Ross-Weir (NRW) method to retrieve the constitutive parameters of low-loss materials”, *2011 SBMO/IEEE MTT-S International Microwave and Optoelectronics Conference (IMOC 2011)*, pp. 488–492, Nov. 2011

- [126] O. Luukkonen, S. Maslovski, and S. Tretyakov, “A Stepwise Nicolson-Ross-Weir-Based Material Parameter Extraction Method”, *IEEE Antennas and Wireless Propagation Lett.*, vol. 10, pp. 1295–1298, Nov. 2011
- [127] W. Weir, “Automatic Measurement of Complex Dielectric Constant and Permeability at Microwave Frequencies”, *SProceedings of the IEEE*, vol. 62, no. 1, pp. 33–36, Jan. 1974
- [128] V. Lucarini, J. Saarinen, K. Peiponen, and E. Vartiainen, “Kramers–Kronig Relations in Optical Materials Research”, *SSOS*, volume 110, April 2005
- [129] X. Chen, T. Grzegorzcyk, B. Wu, J. Pacheco, and J. Kong, “Robust method to retrieve the constitutive effective parameters of metamaterials”, *SPhys. Rev. E Stat. Nonlin. Soft Matter Phys.*, vol. 70, pp. 0166081–0166088, Jul. 2004
- [130] X. Chen, T. Grzegorzcyk, B. Wu, J. Pacheco, and J. Kong, “Robust method to retrieve the constitutive effective parameters of metamaterials”, *SPhys. Rev. E Stat. Nonlin. Soft Matter Phys.*, vol. 70, pp. 0166081–0166088, Jul. 2004